



Jones, Kirsty Anne (2021) *Novel parameters for assessing cardiac dyssynchrony*. PhD thesis.

<https://theses@gla.ac.uk/82588/>

Copyright and moral rights for this work are retained by the author

A copy can be downloaded for personal non-commercial research or study, without prior permission or charge

This work cannot be reproduced or quoted extensively from without first obtaining permission in writing from the author

The content must not be changed in any way or sold commercially in any format or medium without the formal permission of the author

When referring to this work, full bibliographic details including the author, title, awarding institution and date of the thesis must be given

Enlighten: Theses

<https://theses.gla.ac.uk/>
research-enlighten@glasgow.ac.uk

Novel Parameters for Assessing Cardiac Dyssynchrony

Kirsty Anne Jones

Submitted in fulfilment of the requirements for the
Degree of Doctor of Philosophy

School of Physics and Astronomy
College of Science and Engineering
University of Glasgow



University
of Glasgow

October 2021

Abstract

Cardiac mechanical dyssynchrony describes the variation in the timing of contraction or relaxation within the ventricle and can be assessed using various imaging techniques. Electrical dyssynchrony has previously been used as a surrogate for mechanical dyssynchrony. However, it is now widely recognised that mechanical dyssynchrony can occur without the presence of electrical dyssynchrony. Therefore, it has become increasingly important to develop quantitative measures of mechanical dyssynchrony. Although echocardiography has led in this area, radionuclide ventriculography (RNVG) imaging can also be used.

This research aims to investigate the use of novel phase parameters from RNVG, including synchrony, entropy, phase standard deviation, approximate entropy, and sample entropy, to provide a quantitative measure of cardiac dyssynchrony. There is limited published data applying these parameters to phase images, and there is currently no established normal range. To achieve these aims, each parameter has been optimised and tested on both simulated and clinical data. In addition, the optimised parameters have been applied to clinical data sets to assess the ability to predict patient outcome.

The results highlight the importance of optimising input parameters for approximate entropy and sample entropy and demonstrate that the selected values are appropriate for application to RNVG phase images. The clinical results using the optimised parameters are promising for assessing patients prior to receiving cardiotoxic cancer therapy. Approximate entropy combined with left ventricular ejection fraction was able to predict those at a higher risk of cardiac dysfunction before treatment commenced. The dyssynchrony parameters were also used to assess a group of patients with heart failure with reduced ejection fraction. The results demonstrated that dyssynchrony, left ventricular ejection fraction, and right ventricular ejection fraction improved after beta-blocker. In addition, patients with non-ischaemic heart failure and dyssynchronous left ventricular contraction were more likely to respond to beta-blocker therapy.

This research has successfully investigated novel dyssynchrony parameters for radionuclide ventriculography imaging. Overall, this research strengthens the idea that dyssynchrony can predict patient outcomes and improve clinical decision making.

Acknowledgements

I would like to thank the following people, without whom none of this would have been possible:

Bill Martin for giving me the opportunity to work in nuclear cardiology, encouraging me to do this PhD, and all of the advice over the years - especially after retiring.

My supervisors Craig Paterson, David Hamilton, and Sandy Small for the invaluable input and advice they have given me throughout the PhD. To Nicholas Goodfield for advising on all of the cardiology aspects of the research. Surajit Ray for answering all of my statistics questions. To my friends and colleagues in the Department of Nuclear Cardiology, especially Kurian Oommen and Jamie Robinson.

Thank you to all of my friends. Especially Fiona for always believing in me, and Vani who has given me the best PhD advice over the last few years.

I would also like to thank my parents, Chris, Femke, my gran, and Aunt Janet for always supporting and encouraging me, and thanks to Frieda for the welcome distraction from PhD work.

And lastly, thank you to Lawrence for his patience, support, and advice.

University of Glasgow
College of Science and Engineering
Identity Statement of Originality to Accompany Thesis Submission

Name: Kirsty Jones

Registration Number:

I certify that the thesis presented here for examination for PhD degree of the University of Glasgow is solely my own work other than where I have clearly indicated that it is the work of others (in which case the extent of any work carried out jointly by me and any other person is clearly identified in it) and that the thesis has not been edited by a third party beyond what is permitted by the University's PGR Code of Practice.

The copyright of this thesis rests with the author. No quotation from it is permitted without full acknowledgement. I declare that the thesis does not include work forming part of a thesis presented successfully for another degree [unless explicitly identified and as noted below].

I declare that this thesis has been produced in accordance with the University of Glasgow's Code of Good Practice in Research.

I acknowledge that if any issues are raised regarding good research practice based on review of the thesis, the examination may be postponed pending the outcome of any investigation of the issues.

Statement of conjoint work

I confirm that the research in chapters 5, 7, and 8 were submitted for publication in collaboration with the Department of Nuclear Cardiology, Glasgow Royal Infirmary, the Department of Nuclear Physics and the Department of Mathematics and Statistics, University of Glasgow. I wrote the submitted manuscripts, designed the studies, wrote the software, analysed the data, and created the plots. My supervisors and collaborators advised on study design and statistics, assisted with data collection, and critically reviewed the manuscripts.

Signature: Date: ...15/10/2021.....

This completed statement must be bound into the submitted copies of the soft-bound thesis.

Published Work

The following papers based on this PhD have been published or submitted to a journal for publication.

Jones, K.A., Small, A.D., Ray, S., Hamilton, D.J., Martin, W., Robinson, J., Goodfield, N.E.R. and Paterson, C.A., 2020. Radionuclide ventriculography phase analysis for risk stratification of patients undergoing cardiotoxic cancer therapy. *Journal of Nuclear Cardiology*, pp.1-9.

Jones, K.A. and Goodfield, N.E.R., 2021. Mechanical dyssynchrony and super-response to CRT. *Journal of Nuclear Cardiology*. <https://doi.org/10.1007/s12350-020-02453-1>

Jones, K.A., Paterson, C.A., Hamilton, D.J., Small, A.D., Martin, W., Robinson, J. and Goodfield, N.E.R., 2021. Optimising approximate entropy for assessing cardiac dyssynchrony with radionuclide ventriculography. *Biomedical Signal Processing and Control*, 68, p.102703.

Jones, K.A., Paterson, C.A., Ray, S., Hamilton, D.J., Small, A.D., Martin, W. and Goodfield, N.E.R. Beta-blockers and mechanical dyssynchrony in heart failure: predictors and treatment response as assessed by radionuclide ventriculography. Submitted to *Journal of Nuclear Cardiology*

Contents

Abstract	i
Acknowledgements	ii
Declaration	iii
Published Work	iv
List of Tables	viii
List of Figures	ix
Glossary	xvi
1 Introduction	1
1.1 Introduction	1
1.2 Aims and Objectives	1
1.3 Outline of Thesis	2
2 Background and Clinical Context	3
2.1 The Heart	3
2.1.1 Cardiovascular System	3
2.1.2 Cardiac Conduction System	3
2.1.3 Ischaemic Heart Disease	4
2.1.4 Myocardial Infarction	6
2.1.5 Left Bundle Branch Block	7
2.2 Cardiac Imaging Modalities	7
2.2.1 Coronary Angiography	7
2.2.2 Echocardiography	8
2.2.3 Cardiac Magnetic Resonance Imaging	9
2.2.4 Computerised Tomography	10
2.3 Nuclear Cardiology	10

2.3.1	Radiopharmaceuticals	10
2.3.2	Gamma Camera	11
2.3.3	Cardiac Gating	12
2.3.4	Myocardial Perfusion Imaging	13
2.3.5	Radionuclide Ventriculography	15
2.4	Summary	16
3	Ventricular Mechanical Dyssynchrony	17
3.1	Introduction	17
3.2	Mechanical Dyssynchrony	17
3.3	RNVG Phase and Amplitude Images	19
3.4	Dyssynchrony Measured From RNVG Phase Analysis	23
3.4.1	Phase Standard Deviation	23
3.4.2	Synchrony and Entropy	25
3.4.3	Approximate Entropy and Sample Entropy	26
3.5	Conclusions	28
4	Statistical Analysis and Machine Learning	29
4.1	Introduction	29
4.2	Logistic Regression	29
4.3	Ridge and LASSO Regression	32
4.4	Cross-Validation	33
4.5	Evaluating Model Performance	35
4.6	Comparing Samples	36
5	Software and Parameter Optimisation	39
5.1	Introduction	39
5.2	Software	39
5.2.1	Software Validation and Testing	40
5.2.2	Generated Data	40
5.3	Selecting Sequence Length (m) and Tolerance (r)	44
5.4	Effect of Data Length	49
5.5	Data Order	51
5.6	Conclusions	55
6	Normal Range and Reproducibility	56
6.1	Introduction	56
6.2	Normal Range	56
6.3	Reproducibility	62
6.4	Correlation Between Dyssynchrony Parameters	65

6.5	Conclusions	68
7	Risk Stratification for Chemotherapy Patients	69
7.1	Introduction	69
7.2	Methods	70
7.2.1	Data Acquisition	70
7.2.2	Data Analysis	71
7.2.3	Statistical Analysis	71
7.3	Results	71
7.4	Discussion	73
7.5	Conclusions	80
8	Effect of Beta-blockade on Dyssynchrony	81
8.1	Introduction	81
8.1.1	Beta-blockade Therapy	82
8.2	Method	83
8.2.1	Study outline	83
8.2.2	Data Acquisition and Processing	84
8.2.3	Statistical Analysis	85
8.3	Results	85
8.3.1	Effect of Beta-Blocker on Dyssynchrony	85
8.3.2	Predicting Response to Beta-Blocker	86
8.3.3	Predictive Models	97
8.4	Discussion	99
8.4.1	Limitations	101
8.5	Conclusions	101
9	Summary and Conclusions	102
	Bibliography	106

List of Tables

2.1	Commonly used radionuclides in nuclear cardiology	11
4.1	Example logistic regression results	31
5.1	Summary of statistics for <i>ApEn</i> with data order	52
5.2	Summary of statistics for <i>SampEn</i> with data order	52
6.1	Comparison of RNVG dyssynchrony normal range from the literature	57
6.2	Normal Range (n=187)	58
6.3	Results comparing normal, MI and LBBB groups.	58
6.4	Correlation values for intra-operator variability	62
7.1	Summary of results for each phase parameter for predicting cardiac dysfunction	73
7.2	Logistic Regression Model to predict response to cardiotoxic chemotherapy . .	79
8.1	NYHA Class Definition	82
8.2	Study inclusion and exclusion criteria	84
8.3	Baseline patient characteristics	88
8.4	Comparing RNVG parameters pre and post beta-blockade	89
8.5	Comparing RNVG parameters pre and post beta-blockage, split by presence of ischaemia	90
8.6	Baseline clinical and dyssynchrony measures for the full heart failure cohort (n=86), for predicting response to beta-blocker	91
8.7	Comparing baseline clinical and dyssynchrony measures, split by etiology (n=86), for predicting response to beta-blocker.	92
8.8	Summary of Logistic Regression Models	97
8.9	Logistic Regression Models for predicting response to beta-blockade	98

List of Figures

2.1	Labelled diagram of the heart [1]	4
2.2	Cardiac conduction system [2] showing the position of the sinoatrial node where the electrical stimulus is generated and the path that the electrical signal travels through the heart.	5
2.3	ECG waveform. The P wave is associated with contraction of the atria, the QRS complex reflects the contraction of the ventricles, and the T wave is associated with the repolarisation of the ventricles.	5
2.4	Ischaemic cascade. Imaging tests, shown by the yellow arrows, can detect ischaemia before ECG changes or chest pain occurs. Prolonged absence of blood supply to the cardiac muscle will lead to necrosis (represented by the dotted line) and the damage will no longer be reversible.	6
2.5	Diagram of coronary stent placement. The stent is expanded within the coronary artery during a coronary angiogram to improve blood flow. The cross sectional view shows the stent around the walls of the of the artery and the compressed plaque.	8
2.6	Example of global longitudinal strain assessment by echo [3]. The myocardium is automatically fitted then tracked during the cardiac cycle using speckle tracking. The plots next to each longitudinal view show the motion for each segment within the ventricle. The bulls eye plot on the right displays the measured GLS value for each segment in the ventricle.	9
2.7	The main components of a conventional gamma camera. Gamma photons travelling parallel to the collimator will pass through the lead septa, be converted to visible light by the scintillation crystal before being amplified and converted to an electrical signal by the photomultiplier tubes.	12
2.8	Example of 8 frame cardiac gating. The signal is triggered on the R wave of the ECG. Each of the frames corresponds to a different part of the ECG signal. . .	13

2.9	(a) Short axis, horizontal long axis, and vertical long axis views used for MPI images. (b) Example of three slices from a normal perfusion scan at stress and rest. (c) Example of a perfusion scan for a patient with severe ischaemia. There is a large anterior and lateral defect on stress imaging which substantially improves on rest imaging.	14
2.10	Example of end-diastolic (left) and end-systolic (right) frames of an RNVG scan, showing the blood pool in left and right ventricles. At end-systole, the atria can also be seen. Regions of interest (ROI) have been outlined for each ventricle and background to allow calculation of ejection fraction.	15
3.1	The time-activity curve shows the number of counts in the left ventricle over the cardiac cycle. This is a normal shape for a time-activity curve showing normal emptying and filling of the left ventricle. As the ventricle contracts during systole, the blood in the chamber is pumped out, and the number of counts reduces. The maximum change in counts is known as the amplitude and the phase refers to the onset of mechanical contraction.	20
3.2	Phase histogram showing the frequency of phase angles for the pixels in the left ventricular region of interest. The corresponding phase image can be seen in the top right. This is an example of a phase histogram for normal phase.	21
3.3	Example images showing phase pattern and associated phase histogram for (a) a normal patient with similar phase values throughout the ventricles, (b) a patient with previous myocardial infarction (MI) with late phase values in the area of a MI, (c) a patient with left bundle branch block, where there is a gradual change in phase values across the left ventricle and (d) a patient with a large aneurysm where two distinctly separate segments within the left ventricle are contracting at different times.	22
3.4	(a) Amplitude image, (b) phase image for patient with normal RNVG. In the amplitude image, red and white represent a higher change in counts than the green pixels. The lateral and apical segments are contributing more than the septum, because the septum is also being pulled by the right ventricle so can not contract as much as the lateral and apical segments.	24
3.5	(a) Amplitude image, (b) phase image for patient with aneurysm. The phase image has two separate sections within the left ventricle, contracting at opposite times. The associated amplitude image shows that the area with the aneurysm has a higher change in counts during the cardiac cycle than the remainder of the left ventricle.	24
3.6	Example of phase vectors showing (a) completely synchronous phase, synchrony = 1, (b) completely random phase, synchrony = 0 and (c) two synchronous sub-regions synchrony = 0.	25

4.1	The sigmoid function that is used in logistic regression to map a prediction to a probability between 0 and 1. The decision boundary is set to 0.5 on the y-axis.	32
4.2	Example data showing an appropriate fit (left) to discriminate between the red and blue points and a model that has been over-fitted to the training data (right). The more flexible the model, the more likely it will overfit the training data. This example is for illustrative purposes and has not been fitted mathematically.	34
4.3	Illustration of the data split for 5-fold cross-validation. Each iteration is performed using a different test-train split, and the average results are reported.	35
4.4	An example of an ROC curve. The red dotted line represents a random classifier, with an AUC of 0.5 and the green line represents a good classifier. The perfect algorithm is represented by the blue line and would have an AUC of 1, representing 100% sensitivity and 100% specificity.	37
5.1	Overview of R code used to extract phase parameters. Phase and amplitude images are read into the code in DICOM format. The images are then masked by the region of interest to zero the pixels outside of the region. The phase parameters are then calculated and the results displayed.	41
5.2	Function within R code used to calculate phase parameters for multiple regions of interest. The phase pixel values are converted from radians to degrees, and the image matrix is converted into a 2D sequence before the calculations. Phase histograms for both the left and right ventricles are created with 1 degree bin width. Synchrony and entropy are calculated, then a loop is used to compare a sequence of m pixels to every other sequence of m pixels for the <i>ApEn</i> and <i>SampEn</i> calculations. The calculated phase parameters are then printed to the screen and saved in a text file.	42
5.3	Example output image from R code showing the phase and amplitude images that were read into the code, the phase within the selected regions of interest for the left and right ventricles, and the phase histograms for left ventricle (bottom right) and right ventricle (bottom left). The phase histogram is a narrow peak for the left ventricle, suggesting it is normal. The right ventricle has two separate peaks on the histogram.	43
5.4	Phase image with radial segments, used to acquire mean and standard deviation of the phase for each of the 16 segments. Simulated data was then created in a 16 segment model using phase values based on the patient data.	44
5.5	Examples of generated images to represent (a) normal phase within the left ventricle ROI and (b) to represent abnormal phase due to the presence of an MI. These images are generated based on mean phase and standard deviation from clinical images.	44

5.6	Simulated data demonstrating how $ApEn$ varies with m and r for (a) normal phase image and (b) a phase image for an MI	46
5.7	Simulated data demonstrating how $SampEn$ varies with m and r for (a) normal phase image and (b) a phase image for an MI. The white areas represent an infinite $SampEn$ value.	46
5.8	Simulated data which represents a phase image for normal left ventricular contraction (in red) and a large MI (in green), demonstrating how $ApEn$ varies with increasing tolerance r , where sequence length $m = 2$. The shaded area represents the difference in $ApEn$ between the normal and MI phase images.	47
5.9	Average $ApEn$ for normal (red), MI (green) and LBBB (yellow) patient groups using varying values of tolerance r , where $m = 2$	48
5.10	Simulated data which represents a phase image for normal left ventricular contraction (in red) and a large MI (in green), demonstrating how $SampEn$ varies with increasing tolerance r , where sequence length $m = 2$. The shaded area represents the difference in $SampEn$	48
5.11	Average $SampEn$ for normal (red), MI (green) and LBBB (yellow) patient groups using varying values of tolerance r , where $m = 2$	49
5.12	Variation of $ApEn$ with left ventricle size for (a) $m = 2, r = 1$ (b) $m = 2, r = 7$, demonstrating a lack of consistency for $r = 1$ with increasing ventricle size for simulated data.	50
5.13	Variation of $SampEn$ with left ventricle size for $m = 2, r = 4$, showing consistent $SampEn$ values with increasing ventricle size for simulated data.	50
5.14	The four directions tested for reading the image matrix, reading image from (a) left to right, (b) top to bottom, (c) left - right, right - left etc (d) top - bottom, bottom to top etc.	51
5.15	ROC analysis of $ApEn$ for each data order, comparing the difference between normal and MI groups.	53
5.16	ROC analysis of $SampEn$ for each data order, comparing the difference between normal and MI groups.	54
6.1	Comparison of synchrony for normal, MI and LBBB groups. Kruskal-Wallis was used to compare all three groups and Wilcoxon rank-sum test was used for pairwise comparison.	59
6.2	Comparison of entropy for normal, MI and LBBB groups. Kruskal-Wallis was used to compare all three groups and Wilcoxon rank-sum test was used for pairwise comparison.	59
6.3	Comparison of phase standard deviation for normal, MI and LBBB groups. Kruskal-Wallis was used to compare all three groups and Wilcoxon rank-sum test was used for pairwise comparison.	60

6.4	Comparing <i>ApEn</i> for normal, MI and LBBB groups. Kruskal-Wallis was used to compare all three groups and Wilcoxon rank-sum test was used for pairwise comparison.	61
6.5	Comparison of <i>SampEn</i> for normal, MI and LBBB groups. Kruskal-Wallis was used to compare all three groups and Wilcoxon rank-sum test was used for pairwise comparison.	61
6.6	Comparing intra-operator variability of synchrony. ROI 1 vs ROI 2 in Bland Alman plot (a) and correlation (b).	63
6.7	Comparing intra-operator variability of entropy. ROI 1 vs ROI 2 in Bland Alman plot (a) and correlation (b).	63
6.8	Comparing intra-operator variability of phase standard deviation. ROI 1 vs ROI 2 in Bland Alman plot (a) and correlation (b).	64
6.9	Comparing intra-operator variability of <i>ApEn</i> . ROI 1 vs ROI 2 in Bland Alman plot (left) and correlation (right).	64
6.10	Comparing intra-operator variability of <i>SampEn</i> . ROI 1 vs ROI 2 in Bland Alman plot (a) and correlation (b).	65
6.11	Scatter plots for the normal group, showing the correlation for each pair of variables with the associated correlation value, with the variable names displayed along the edges of the matrix. The diagonal boxes display the distribution for each variable. The scatter plots on the lower left area show the relationship between each pair of variables, and the Pearson correlation coefficient for each pair of variables is displayed on the upper right area.	66
6.12	Scatter plots for the MI group, showing the correlation for each pair of variables with the associated correlation value, with the variable names displayed along the edges of the matrix. The diagonal boxes display the distribution for each variable. The scatter plots on the lower left area show the relationship between each pair of variables, and the Pearson correlation coefficient for each pair of variables is displayed on the upper right area.	67
7.1	Scatter plots showing the correlation for each pair of variables with the associated correlation value, with the variable names displayed along the edges of the matrix. The diagonal boxes display the distribution for each individual variable. The scatter plots in lower left area show the relationship between each pair of variables, and the Pearson correlation coefficient for each pair of variables is displayed in the upper right area.	74
7.2	Synchrony for patients calculated from baseline RNVG phase image, split into two groups based on LVEF decline.	75
7.3	Entropy for patients calculated from baseline RNVG phase image, split into two groups based on LVEF decline.	75

7.4	Phase SD for patients calculated from baseline RNVG phase image, split into two groups based on LVEF decline.	76
7.5	<i>ApEn</i> for patients calculated from baseline RNVG phase image, split into two groups based on LVEF decline.	76
7.6	<i>SampEn</i> for patients calculated from baseline RNVG phase image, split into two groups based on LVEF decline.	77
7.7	Baseline LVEF for patients, split into two groups based on LVEF decline. . . .	77
7.8	Baseline LVEF plotted against baseline <i>ApEn</i> for both groups. The dashed lines represent the mean <i>ApEn</i> and mean LVEF of the test population.	78
8.1	Scatter plots showing the correlation for each pair of variables with the associated correlation value, with the variable names displayed along the edges of the matrix. The diagonal boxes display the distribution for each individual variable. The scatter plots on lower left area show the relationship between each pair of variables, and the Pearson correlation coefficient for each pair of variables is displayed on the upper right area.	87
8.2	Synchrony for heart failure patients, calculated from baseline RNVG phase image and split into two groups based on response to beta-blocker therapy. A lower value of synchrony corresponds to worse dyssynchrony. Significance was tested using a Wilcoxon rank-sum test.	93
8.3	Entropy for heart failure patients, calculated from the baseline RNVG phase image and split into two groups based on response to beta-blocker therapy. Higher entropy corresponds to worse dyssynchrony. Significance was tested using a two-sample t-test.	93
8.4	<i>ApEn</i> for heart failure patients, calculated from the baseline RNVG phase image and split into two groups based on response to beta-blocker therapy. A higher value of <i>ApEn</i> corresponds to worse dyssynchrony. Significance was tested using a two-sample t-test.	94
8.5	<i>SampEn</i> for heart failure patients, calculated from the baseline RNVG phase image and split into two groups based on response to beta-blocker therapy. A higher value of <i>SampEn</i> corresponds to worse dyssynchrony. Significance was tested using a Wilcoxon rank-sum test.	94
8.6	Phase standard deviation for heart failure patients, calculated from the baseline RNVG phase image and split into two groups based on response to beta-blocker therapy. Significance was tested using a Wilcoxon rank-sum test.	95
8.7	Baseline LVEF for heart failure patients, calculated from the baseline RNVG phase image and split into two groups based on response to beta-blocker therapy. Significance was tested using a Wilcoxon rank-sum test.	95

8.8 RVEF for heart failure patients, calculated from the baseline RNVG phase image and split into two groups based on response to beta-blocker therapy. Significance was tested using a Wilcoxon rank-sum test. 96

Glossary

ANOVA = A One Way Analysis of variance

ApEn = Approximate Entropy

AUC = Area Under the Receiver-Operator Curve

ARVC = Arrhythmogenic Right ventricular Cardiomyopathy

CZT = Cadmium Zinc Telluride

CRT = Cardiac Resynchronisation Therapy

CT = Computed Tomography

CABG = Coronary Artery Bypass Graft

DICOM = Digital Imaging and Communications in Medicine

Echo = Echocardiography

ECG = Electrocardiogram

ESC = European Society of Cardiology

GLS = Global Longitudinal Strain

HFmEF = Heart Failure with Moderate Ejection Fraction

HFpEF = Heart Failure with Preserved Ejection Fraction

HF_rEF = Heart Failure with reduced Ejection Fraction

ICD = Implantable Cardioverter Defibrillator

LASSO = Least Absolute Shrinkage and Selection Operator

LB_{BB} = Left Bundle Branch Block

LVEF = Left Ventricular Ejection Fraction

MRI = Magnetic Resonance Imaging

MSE = Mean Squared Error

MI = Myocardial Infarction

MPI = Myocardial Perfusion Imaging

NYHA = New York Heart Association

PCI = Percutaneous Coronary Intervention

PFTs = Pulmonary Function Tests

RNVG = Radionuclide Ventriculography

ROC = Receiver-Operator Characteristics

ROI = Regions of Interest

RSS = Residual Sum of Squares

RVEF = Right Ventricular Ejection Fraction

SampEn = Sample Entropy

SPECT = Single Photon Emission Computed Tomography

SD = Standard Deviation

Chapter 1

Introduction

1.1 Introduction

There has been increased interest in assessing left ventricular mechanical dyssynchrony within cardiology due to the potential to effect patient treatment and outcome. Mechanical dyssynchrony can be measured using various different imaging modalities, including echo (2-D M-mode, spectral Doppler, and tissue Doppler imaging parameters), single photon emission computed tomography myocardial perfusion imaging (SPECT MPI), radionuclide ventriculography (RNVG), and magnetic resonance imaging (MRI). In nuclear cardiology, dyssynchrony can be assessed using phase images from RNVG with various different parameters without requiring any additional imaging time or radiation dose. To date, measures of dyssynchrony from echocardiography have led the field, but it has not yet been adopted into widespread clinical practice. There is currently limited published data for dyssynchrony assessed by RNVG phase and it has not been widely investigated as a predictor of patient outcome. This research will build on the current dyssynchrony knowledge and attempt to expand the understanding in this area using novel parameters.

1.2 Aims and Objectives

The aim of this PhD is to investigate novel quantitative measures of cardiac left ventricular dyssynchrony using RNVG phase analysis. The main objectives of this PhD are listed below.

1. Develop code for calculating novel dyssynchrony parameters from RNVG phase images.
2. Optimise novel RNVG phase parameters for assessing dyssynchrony.
3. Investigate the normal range and reproducibility for each parameter.
4. Demonstrate the application of novel dyssynchrony parameters and validate using clinical data.

5. Determine if dyssynchrony measured from RNVG phase has the potential to predict clinical outcome.

1.3 Outline of Thesis

A brief introduction to the imaging and clinical terms that will be used throughout the thesis will be given in Chapter 2. Chapter 3 will introduce cardiac mechanical dyssynchrony and the parameters that will be calculated from radionuclide ventriculography (RNVG) phase images to quantify mechanical dyssynchrony. This is followed by a short overview of the statistical tests and machine learning algorithms that will be applied in this research in Chapter 4. To meet the objectives of this thesis, the phase parameters will be optimised using both simulated data and clinical images in Chapter 5. A normal range will be defined using the optimised parameters, and the reproducibility will be assessed in Chapter 6. The predictive value of these novel parameters of left ventricular function will be tested on various patient groups, including patients who are receiving cardiotoxic cancer therapy in Chapter 7. The phase parameters will be applied to the baseline scans to determine if dyssynchrony can predict which patients are more likely to experience a decline in cardiac function during or after chemotherapy. In Chapter 8, the dyssynchrony parameters will be used to assess patients in heart failure with reduced ejection fraction, both pre and post beta-blocker treatment. The research in Chapter 8 will investigate the effect of beta-blocker on dyssynchrony and discover if dyssynchrony at baseline will predict response to beta-blocker. Chapter 9 will summarise and conclude the results of this research.

Chapter 2

Background and Clinical Context

This chapter gives a brief introduction to the imaging and clinical terms that will be used throughout Chapters 3-8. The cardiovascular system will be introduced along with a brief introduction to the cardiac conditions relevant to this research. An overview of the cardiac imaging modalities will also be given.

2.1 The Heart

2.1.1 Cardiovascular System

The heart is divided into four chambers - right atrium, right ventricle, left atrium, and left ventricle, which work together to circulate oxygenated blood around the body. The diagram in Figure 2.1 shows the main components of the heart, including ventricles, atria, and myocardium. The cardiac valves between the chambers operate to ensure that blood flows in only one direction. The left ventricle pumps oxygen-rich blood through the aorta and delivers blood through the arteries to the rest of the body before the veins return the deoxygenated blood to the right atrium. The blood is then passed from the right atrium to the right ventricle through the tricuspid valve and pumped to the lungs via the pulmonary arteries. The blood is oxygenated in the lungs and returned to the left atria, then passed through the mitral valve to the left ventricle. The myocardium is thicker on the left side of the heart because the left ventricle needs to use more force than the right ventricle to pump the blood to the rest of the body.

2.1.2 Cardiac Conduction System

In a normal heart, ventricular contraction is a highly coordinated process, which is essential to maintain high cardiac output. In a normal contraction, the base and apex of the left ventricle will twist in opposite directions, creating a wringing motion. Cardiac contraction is a complex system that uses a combination of cardiac muscle cells and conducting fibres. Figure 2.2 shows an illustration of the electrical conduction path. The conduction starts in the sinoatrial node,

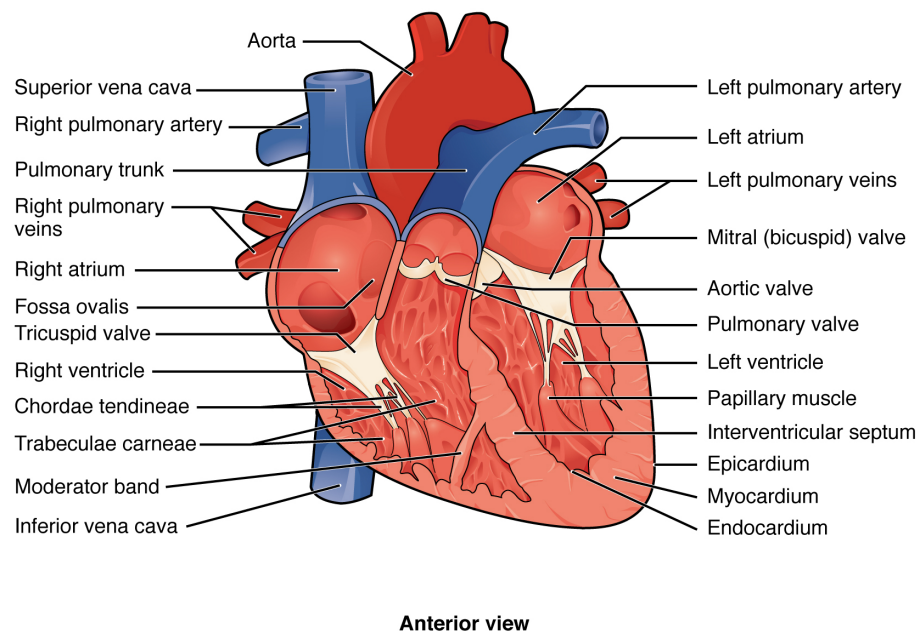


Figure 2.1: Labelled diagram of the heart [1]

where an electrical stimulus is generated, activating the atria. The electrical signal then travels towards the atrioventricular node via the internodal pathways, where the signal is slowed for a brief time before travelling via the bundle of His conduction pathway towards the ventricles. The bundle of His splits into the right and left bundle branches, then into the Purkinje fibres to stimulate the ventricles. This causes the left and right ventricle to contract and pump out blood. The cardiac cycle must be coordinated to function efficiently. Any damage or disruption to the conduction system can cause dyssynchronous contraction.

The electrical signal of the heart can be assessed using an electrocardiogram (ECG). The ECG signal is recorded using 12 leads connected to the patient. An ECG can be used to determine the rate, rhythm and conduction of the heart. The letters P, Q, R, S, T, and U are used to describe each deflection on the ECG, where each deflection represents a different part of the conduction cycle, as seen in Figure 2.3. The P wave is associated with the atria contracting, the QRS complex reflects the depolarization and contraction of the ventricles, and the T wave is associated with the repolarisation of the ventricles. The U wave is thought to represent the repolarisation of the papillary muscles, but it is not usually visible on the ECG. Figure 2.3 shows the shape of a normal QRS from the ECG. The time between two R waves is the R-R interval and can be used for cardiac gating.

2.1.3 Ischaemic Heart Disease

Ischaemic heart disease is a leading cause of death in the UK, and it was the leading cause of death worldwide in 2019 [4, 5]. The disease is caused by plaque building up along the

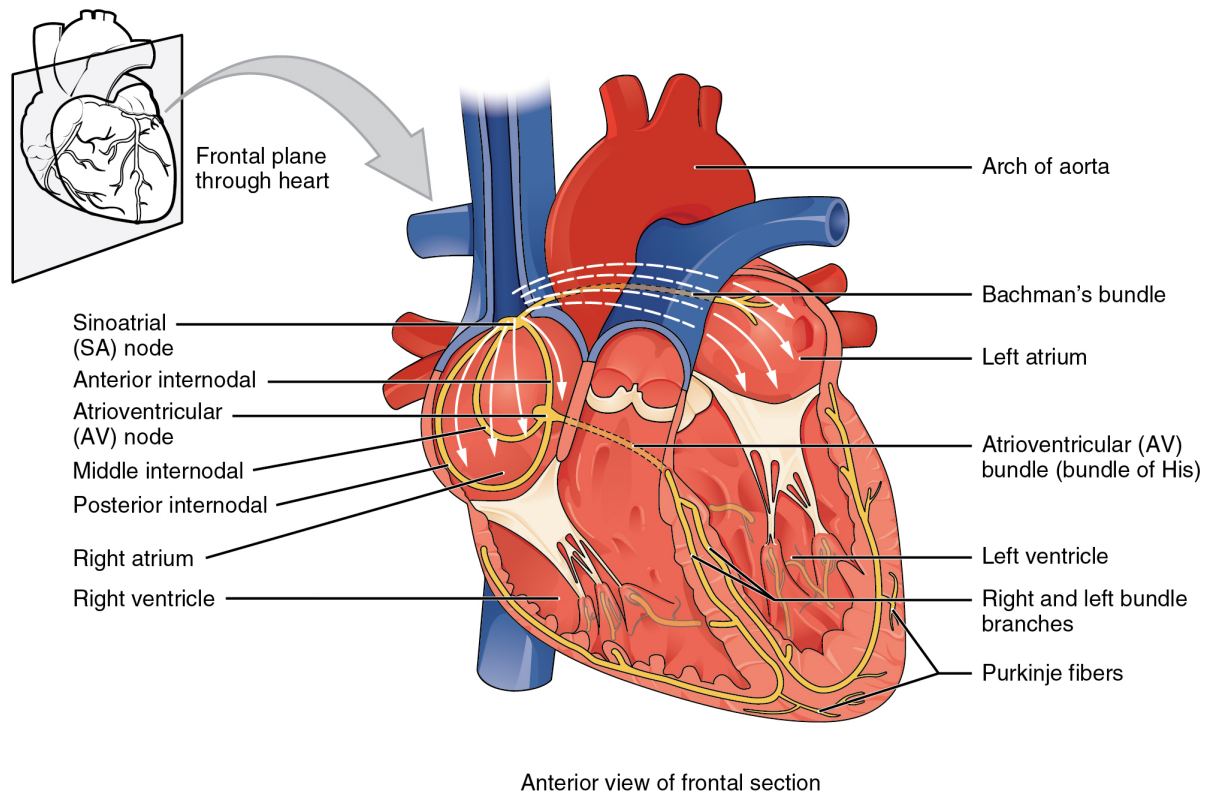


Figure 2.2: Cardiac conduction system [2] showing the position of the sinoatrial node where the electrical stimulus is generated and the path that the electrical signal travels through the heart.

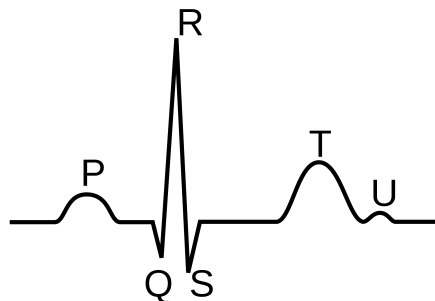


Figure 2.3: ECG waveform. The P wave is associated with contraction of the atria, the QRS complex reflects the contraction of the ventricles, and the T wave is associated with the repolarisation of the ventricles.

coronary arteries' inner walls, causing narrowing and subsequently reduced blood flow to the myocardium. When an obstructed coronary artery supplies the muscle of the heart, it may not be possible to meet the oxygen demands of the body during exertion. This is known as myocardial ischaemia. Ischaemic heart disease can be diagnosed by various imaging modalities, including coronary angiography, nuclear medicine, computed tomography (CT), and magnetic resonance imaging (MRI). The ischaemic cascade is illustrated in Figure 2.4. This figure shows the changes that occur with increasing duration and severity of ischaemia, along with techniques for diagnosis. ECG changes and chest pain are late symptoms of ischaemia, but a perfusion abnormality can be detected with a myocardial perfusion scan (MPI) or contrast MRI much earlier. Ischaemic heart disease can be treated with medication, angioplasty or surgery. Once the cardiac tissue is necrotic, it is no longer reversible.

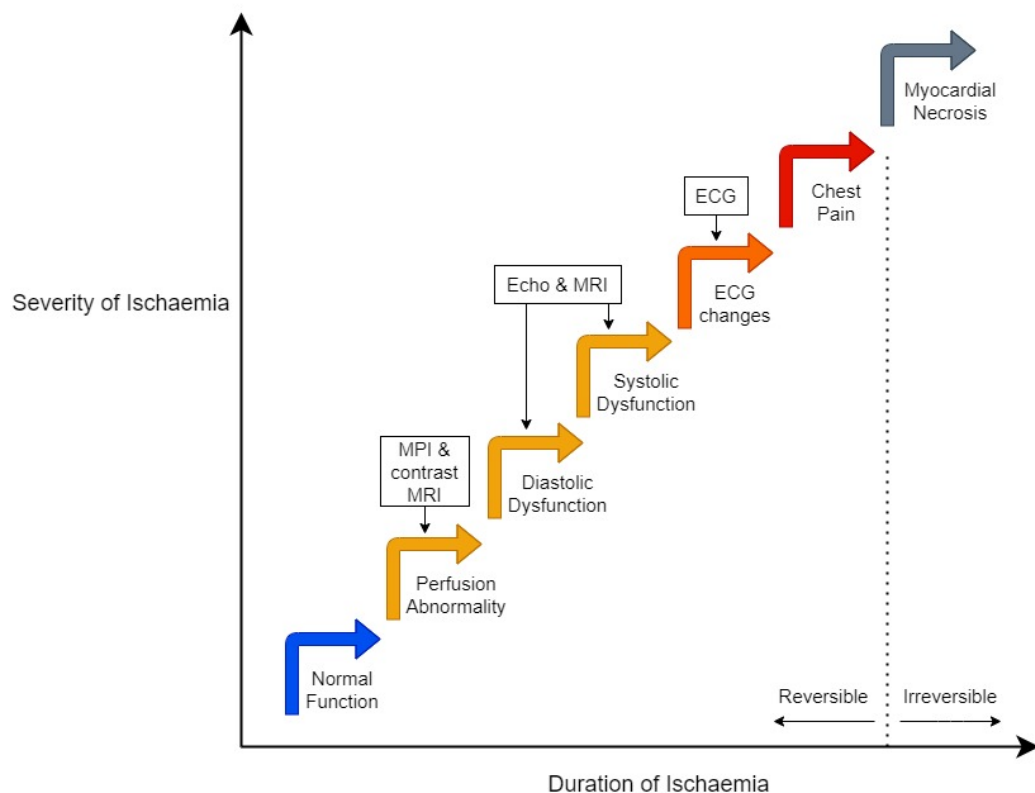


Figure 2.4: Ischaemic cascade. Imaging tests, shown by the yellow arrows, can detect ischaemia before ECG changes or chest pain occurs. Prolonged absence of blood supply to the cardiac muscle will lead to necrosis (represented by the dotted line) and the damage will no longer be reversible.

2.1.4 Myocardial Infarction

Myocardial infarction (MI), also commonly known as a heart attack, can occur when there is a sudden or severe blockage to one of the coronary arteries. This is usually caused by a blood

clot that stops blood from flowing to a part of the heart muscle. The prolonged absence of blood supply will lead to necrosis, meaning heart cells in the occluded territory will die and will not regenerate. These cells are replaced by non-functional scar tissue that will not recover. Scar tissue in the myocardium can affect cardiac contraction and cause dyssynchrony. Patients with a history of previous MI will be compared to normal and LBBB patients in Chapter 5 and Chapter 6 to optimise the radionuclide ventriculography (RNVG) phase parameters and assess the normal range and reproducibility.

2.1.5 Left Bundle Branch Block

Left bundle branch block (LBBB) is a conduction abnormality. For patients with LBBB, the signal from the atrioventricular node is transmitted via the ventricular myocardium, which is slower than the normal conduction system. As a result of the delayed conduction, the left ventricular free wall will contract later than the septum and right ventricle, resulting in dyssynchronous contraction. LBBB can range from very mild, where no treatment is required, to very severe, where the ventricle can no longer operate effectively. LBBB can be diagnosed from an ECG, where the delayed electrical signal from the left ventricle can be seen. On an ECG for a patient with LBBB, the QRS complex would be wider than normal (>120 ms) due to the conduction delay. LBBB can be caused by several different conditions, including but not limited to coronary artery disease, high blood pressure, valve disease, enlarged or weakened heart muscle (cardiomyopathy), infection, myocardial infarction or congenital heart defects. LBBB can also occur when there is no underlying condition. The conduction delay caused by LBBB can affect the timing of contraction, causing mechanical dyssynchrony. In Chapter 5 and Chapter 6, a group of patients with LBBB will be compared to patients with normal conduction as part of the optimisation work for the phase parameters.

2.2 Cardiac Imaging Modalities

2.2.1 Coronary Angiography

Coronary angiography is the gold standard for assessing ischaemia. An interventional cardiologist carries this technique out in a catheterisation laboratory (known as a cath lab). In this procedure, a catheter guide-wire is directed through the blood vessels, with x-ray images to help guide the catheter into the coronary arteries. X-ray fluoroscopy images combined with contrast allows the arteries to be visualised and assess blocked or narrowed coronary arteries. Fractional flow reserve measurements can be used to evaluate the functional significance of stenosis (narrowed artery). Fractional flow reserve measurement is the ratio between the maximum achievable blood flow in a narrowed coronary artery and the theoretical maximum blood flow in a normal coronary artery. Narrowed arteries can be reopened using angioplasty or per-

cutaneous coronary intervention (PCI), also known as a stent. Angioplasty involves using a balloon to reopen a narrowed or blocked artery, and a stent is a small wire-mesh tube that can be expanded in the artery to reopen the artery and improve blood supply. To insert a stent into a narrowed artery, a balloon covered with a stent is inflated once the tip of the catheter is in place. This compresses the plaque and expands the stent, as seen in Figure 2.5. The balloon is then be deflated and withdrawn. A stent can improve blood flow and reduce the patient's symptoms of angina. This procedure is not without risk, so a non-invasive test is often preferred to determine if the patient has ischaemia and if they would benefit from revascularisation with a stent. Results from coronary angiography and MPI are used in Chapter 8 to split the heart failure patients into ischaemic and non-ischaemic groups.

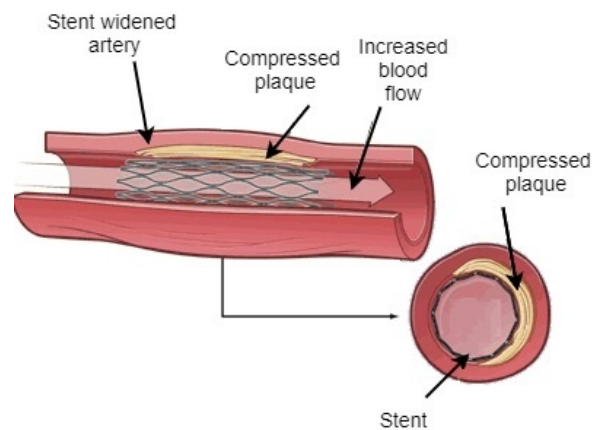


Figure 2.5: Diagram of coronary stent placement. The stent is expanded within the coronary artery during a coronary angiogram to improve blood flow. The cross sectional view shows the stent around the walls of the of the artery and the compressed plaque.

2.2.2 Echocardiography

Echocardiography (echo) uses sound waves to image the heart. The structure and function of the heart, including valve assessment, ejection fraction, and wall motion, can be assessed using echo. This imaging modality has the advantage of being inexpensive, portable, and it does not use ionising radiation. However, it is very dependant on the skill of the operator, so high-quality training is essential. In addition, image quality can be challenging for larger patients or those with scar tissue. Trans-oesophageal echo is a type of echo imaging that uses an endoscope to pass the ultrasound transducer down the oesophagus. This can provide superior imaging because the probe is close to the heart without ribs or lung in the way, but it is more uncomfortable for the patient and has higher associated risks such as oesophageal rupture.

Speckle tracking is an echo imaging technique that can track the motion of tissues in the heart by following the speckle pattern in either the myocardium or blood through each image

frame. Global longitudinal strain (GLS) is a simple parameter derived from speckle tracking to assess cardiac dyssynchrony. GLS measures the change in length of the ventricle as a percentage of the baseline length. An example image showing the GLS assessment can be seen in Figure 2.6. This figure shows how the myocardium is fitted in each longitudinal view. The myocardium is then tracked during the cardiac cycle using speckle tracking. The plots next to the longitudinal views show the motion for each myocardial segment, allowing assessment of regional as well as global measures of strain. The bulls-eye plot on the right of Figure 2.6 displays the measured GLS values for each segment in the ventricle.

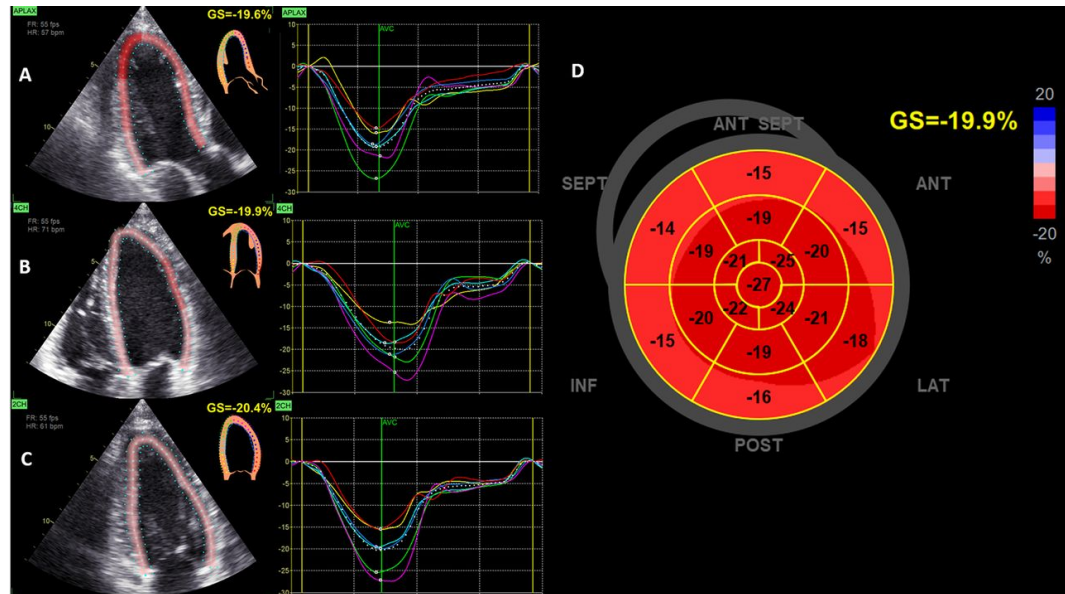


Figure 2.6: Example of global longitudinal strain assessment by echo [3]. The myocardium is automatically fitted then tracked during the cardiac cycle using speckle tracking. The plots next to each longitudinal view show the motion for each segment within the ventricle. The bulls eye plot on the right displays the measured GLS value for each segment in the ventricle.

2.2.3 Cardiac Magnetic Resonance Imaging

MRI uses a magnetic field and radiofrequency coils to image tissues in the body. The measured signal depends on the relaxation times, proton density and other factors such as flow and motion. Cardiac MRI is becoming an increasingly popular tool to investigate cardiac anatomy and assess wall motion and function of the heart. However, it remains expensive and time-consuming, with limited access in some centres for cardiac indications and is unsuitable for some patients who have an older pacemaker.

2.2.4 Computerised Tomography

Computerised Tomography (CT) uses X-rays to produce high-resolution images of the body. CT has made many recent advancements in cardiology and is now recommended in the guidelines to assess ischaemia for low risk symptomatic patients. A contrast agent is used during the cardiac CT scan to visualise any calcification in the coronary arteries. A cardiac CT can provide useful information on the structure of the heart and arteries. This test has good negative predictive power for ischaemia, but it can be challenging to assess the severity of lesions in the arteries.

2.3 Nuclear Cardiology

Nuclear cardiology uses radioisotopes to image the heart non-invasively. There a number of tests available to assess the perfusion and function of the heart. This section will introduce nuclear medicine and describe two of the most common imaging tests in nuclear cardiology - MPI and RNVG. The research carried out in this thesis is based on parameters calculated from RNVG. However, MPI results will be used to define patient groups in Chapters 5 and 8; therefore a brief introduction to MPI will be included.

2.3.1 Radiopharmaceuticals

In nuclear medicine, radiopharmaceuticals are administered to the patient intravenously or orally, depending on the test. The ideal radiopharmaceutical should have a half-life similar to the length of the test to ensure there is enough time to acquire the data, but not so much time that the patient receives an unnecessary radiation dose. A pure gamma emitter with an energy of 50-300 keV is ideal for imaging. Any alpha or beta emission will be absorbed within the patient and increase the patient dose without contributing anything to the image. The radiopharmaceutical should ideally localize only at the target site to improve image quality and reduce radiation to other organs and tissues.

Technetium-99m labelled tracers are the most commonly used radionuclides for medical imaging. Technetium-99m is produced by bombarding Molybdenum-98 with neutrons to create Molybdenum-99, which then decays with a half-life of 66 hours to Technetium-99m. The longer decay time of Molybdenum-99 allows it to be easily transported to medical facilities, where Technetium-99m can be extracted for nuclear medicine imaging tests. Thallium-201 is a cyclotron produced radioisotope that can be used for myocardial perfusion imaging. Thallium-201 is a potassium analogue that uses the sodium-potassium pump to cross into cells of various organs. A summary of the properties of Technetium-99m and Thallium-201 can be seen in Table 2.3.1. Thallium-201 decays by electron capture. Thallium-201 emission has lower energy and a longer half-life than Technetium-99m, resulting in a higher patient dose.

Table 2.1: Commonly used radionuclides in nuclear cardiology

	Technetium-99m	Thallium-201
Half Life	6 hours	73 hours
Energy	140 keV	67-82 keV (88%), 135 and 167 keV (12%)

2.3.2 Gamma Camera

The gamma camera was developed by Hal Anger in 1957 and is well known in the field, so only a brief description is provided here. The gamma camera uses a scintillation detector to image the distribution of radioisotopes within the body. The main components of the gamma camera are shown in Figure 2.7. The gamma camera uses a collimator with lead septa to stop gamma photons that are not travelling parallel to the collimator. Therefore, gamma photons travelling from an oblique angle will be absorbed in the lead septa and do not contribute to the final image. The parallel hole collimator is the most commonly used, but other designs can also be used, including pinhole, diverging, and converging collimators. A parallel collimator was used for all of the research described in this thesis. The parameters that define the collimator's sensitivity and resolution are the hole diameter, length of septa, septal thickness, and the distance from the source.

After passing through the collimator, the gamma photons that interact with the scintillation crystal will produce secondary electrons, which cause the ionisation of several thousand nearby atoms. As each unbound or loosely bound electron falls into a vacant orbit, a photon of equivalent energy is produced. The resulting large number of practically simultaneous flashes of light is the scintillation. Sodium iodide crystals doped with Thallium are the most commonly used scintillation crystal in gamma cameras. The number of visible light photons that are emitted will be proportional to the energy deposited by the incident gamma photon. The conversion efficiency of the scintillation crystal is approximately 10-15%. A light guide is used to couple the output from the scintillation crystal to the photomultiplier tubes. In the photomultiplier tubes, the photons strike the photocathode with enough energy to release electrons. Photoelectrons incident on the first dynode causes excitation and secondary emission. These electrons are then excited towards the following dynodes, and the process is repeated, which has the effect of amplifying the signal. The final signal is proportional to the energy of the incident gamma photon. Positioning logic is used to determine the location of a photon striking the photomultiplier tubes. The detector has a linear response with count rate until the detector saturates. At count rates higher than this, dead time will occur. During clinical imaging, the count rates should always be below this count rate. However, when carrying out quality assurance tests using phantoms, care must be taken to ensure the detector is not saturated.

When a photon has undergone scattering within the patient or the crystal, it is no longer pos-

sible to determine where the gamma photon originated. However, scattered photons lose energy, so some scattered photons can be removed from the final image using the energy spectrum. A pulse height analyser determines and rejects energy signals outside a designated window. The shielding around the camera protects it from light and scattered radiation.

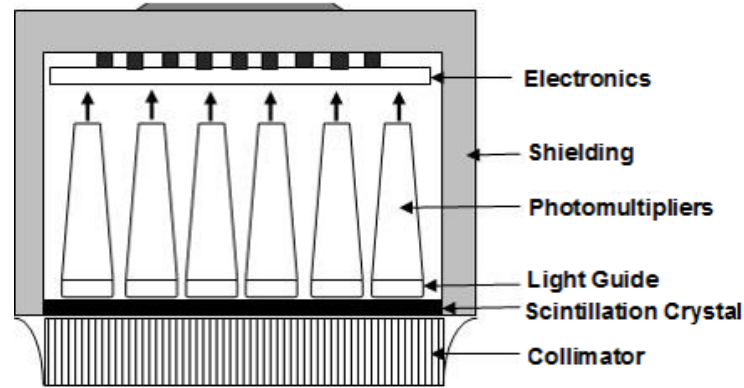


Figure 2.7: The main components of a conventional gamma camera. Gamma photons travelling parallel to the collimator will pass through the lead septa, be converted to visible light by the scintillation crystal before being amplified and converted to an electrical signal by the photomultiplier tubes.

Newer solid-state cardiac gamma cameras are also available, but widespread use in hospitals has been limited by cost. In these detectors, solid-state technology replaces scintillation crystals and photomultiplier tubes. Solid-state cameras used cadmium zinc telluride (CZT) detectors to convert incident gamma photons to an electrical signal directly. CZT gamma cameras have improved sensitivity and spatial resolution compared to conventional gamma cameras, allowing flexibility to reduce patient dose, scan time, and optimise image quality.

Images acquired by the gamma camera can be planar or single photon emission computed tomography (SPECT) images. In a planar image, photons detected from structures at different depths will be superimposed on a two-dimensional image, so activity from underlying or overlying structures can obscure information about the organ or tissue of interest. SPECT is a 3D imaging technique achieved by acquiring planar gamma camera images at different projection angles around the body. The data is then reconstructed into 3D views using either filtered back projection or iterative reconstruction. SPECT provides advantages over planar imaging for separating structures at depth, higher contrast and improved quantification.

2.3.3 Cardiac Gating

Cardiac gating is essential in cardiac imaging to improve image quality and allow cardiac function to be assessed. An illustration of cardiac gating is shown in Figure 2.8. The gating signal is triggered on the R wave of the ECG, and each bin corresponds to a different phase of the heart. The temporal sampling needs to be high enough to ensure the peaks and troughs of the cycle

are not missed. This example is for only 8 frames, but it is more common to use 16 frames, 24 frames, or more depending on the imaging modality. In nuclear cardiology, the maximum number of gating frames is limited by count statistics. Cardiac gating can be either prospective or retrospective. The R-R duration is fixed throughout the scan in prospective gating, even if the heart rate varies. In retrospective gating, the data is binned after the acquisition.

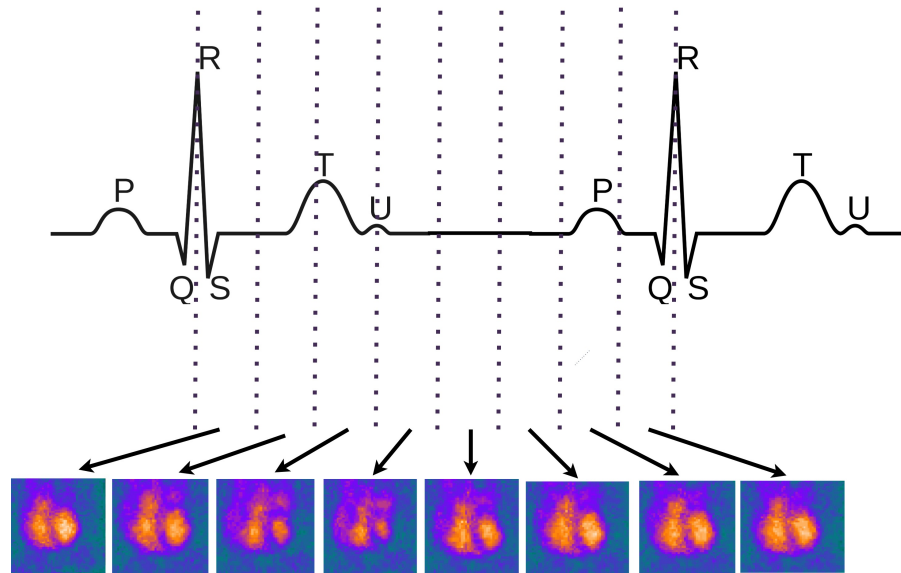


Figure 2.8: Example of 8 frame cardiac gating. The signal is triggered on the R wave of the ECG. Each of the frames corresponds to a different part of the ECG signal.

2.3.4 Myocardial Perfusion Imaging

Myocardial perfusion imaging is used to provide a functional assessment to detect ischaemic heart disease. This test can be performed using Technetium-99m based tracers or Thallium-201. Stress testing can be carried out using a bicycle, treadmill or pharmacological stress agents such as Regadenoson, Adenosine or Dobutamine. Imaging is performed at both stress and rest to assess the myocardial blood supply. Comparing the stress and rest images can identify areas of relatively reduced myocardial blood flow that are associated with ischaemia or scar. Myocardial perfusion imaging can help identify ischaemia and determine which patients are likely to benefit from revascularisation. The MPI images are orientated into three standard cardiac views as shown in Figure 2.9 (a). Example images for a patient with normal perfusion and a patient with ischaemia are shown in Figure 2.9 (b) and (c). The stress images in Figure 2.9 (c) show a large area of reduced tracer uptake anteriorly and laterally with substantial improvement on rest imaging, suggesting severe ischaemia in approximately 50% of the myocardium.

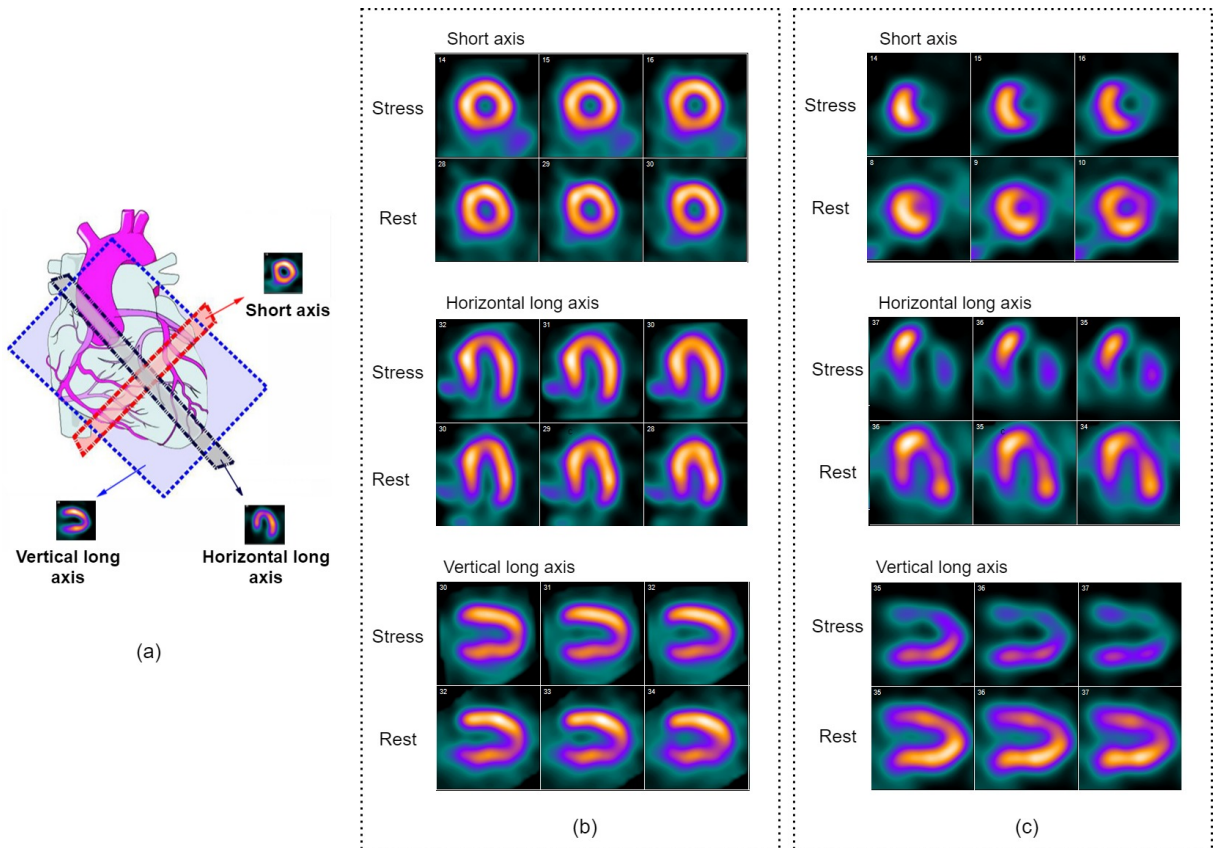


Figure 2.9: (a) Short axis, horizontal long axis, and vertical long axis views used for MPI images. (b) Example of three slices from a normal perfusion scan at stress and rest. (c) Example of a perfusion scan for a patient with severe ischaemia. There is a large anterior and lateral defect on stress imaging which substantially improves on rest imaging.

2.3.5 Radionuclide Ventriculography

RNVG is an established cardiac imaging technique used to measure LVEF and assess ventricular wall motion. To perform an RNVG scan, the patient's red blood cells are labelled with Technetium-99m pertechnetate (^{99m}Tc), allowing the changing volume of blood within the ventricles to be imaged from the resultant gamma emission. Planar or SPECT imaging can be used for RNVG. However, planar RNVG is still commonly used due to its higher reproducibility for ejection fraction assessment [6, 7]. Only planar RNVG will be considered in this research. To acquire a planar RNVG image, the gamma camera must be positioned to achieve the best separation between the left and right ventricles, and the images are gated to the cardiac cycle using an ECG signal. An example of images from planar RNVG can be seen in Figure 2.10. These images show the frames of the RNVG with the highest counts (end-diastolic) and the lowest counts (end-systolic) during the cardiac cycle. The atria can also be seen on the end-systolic frame. Regions of interest (ROI) have been outlined for the left ventricle, right ventricle, and background to measure the number of counts at end-systole and end-diastole to calculate ejection fraction. The data acquired from RNVG can be used to create phase and amplitude images to assess ventricular dyssynchrony. This will be described further in Chapter 3.

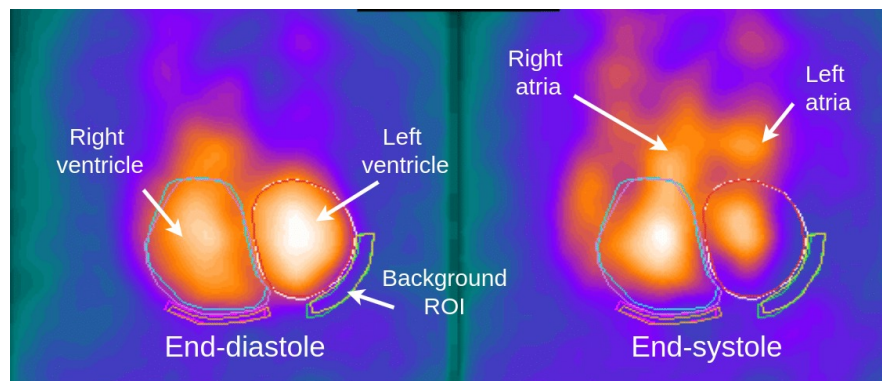


Figure 2.10: Example of end-diastolic (left) and end-systolic (right) frames of an RNVG scan, showing the blood pool in left and right ventricles. At end-systole, the atria can also be seen. Regions of interest (ROI) have been outlined for each ventricle and background to allow calculation of ejection fraction.

Measures of left ventricular cardiac function provide important clinical information relating to diagnosis, treatment, and patient outcome [8–10]. Assessment of LVEF is known to be a powerful prognostic indicator of cardiovascular disease. It predicts morbidity and mortality after a myocardial infarction (MI), and a low LVEF indicates heart failure. RNVG is a well-established technique that can provide a reproducible measure of ejection fraction and is commonly used to assess left ventricular function. Right ventricular ejection fraction (RVEF) can also be assessed using planar RNVG but it is less accurate than other imaging techniques due to the right ventricle overlapping with the right atrium in the best septal view. The ejection fraction is calculated

using the following equation,

$$\text{Ejection fraction} = \frac{(ED_{counts} - Bg_{counts}) - (ES_{counts} - Bg_{counts})}{ED_{counts} - Bg_{counts}} \times 100, \quad (2.1)$$

where ED_{counts} is the number of counts in the ventricle at end-diastole and ES_{counts} is the number of counts at end-systole, and Bg_{counts} is the counts in the background region. Both end-systole and end-diastole regions are background corrected. Inadequate counts in the region of interest or high background counts can compromise image interpretation and affect the accuracy of the measured ejection fraction. Therefore, care must be taken when placing the background region. If it is in an area of high counts, for example, in the descending aorta, the counts measured in the background region will increase, and the ejection fraction will be overestimated. If the background region is outside the body, the ejection fraction will be underestimated.

Echocardiography and MRI can also be used to measure ejection fraction by assessing the ventricular volume at end-systole and end-diastole. However, ejection fraction measurements from different techniques are not directly interchangeable. Each method has its own normal range. Left ventricular ejection fraction will be used to define patient groups or outcome in Chapters 5, 6, 7, and 8.

2.4 Summary

This chapter has provided a brief background introduction to cardiac imaging and introduced the clinical terms that will be used throughout this thesis to define patient groups and assess patient outcome. MI and LBBB patient groups will be used as part of the optimisation work in Chapters 5 and 6 and ejection fractions will be used to assess patient outcome in the clinical studies in Chapters 7 and 8. RNVG imaging will be described further in Chapter 3 for measuring dyssynchrony.

Chapter 3

Ventricular Mechanical Dyssynchrony

3.1 Introduction

The aim of this chapter is to introduce cardiac mechanical dyssynchrony and the parameters that can be calculated from radionuclide ventriculography (RNVG) phase images as measures of mechanical dyssynchrony. The term dyssynchrony is used to describe a variation in the timing of contraction or relaxation within the ventricle (intraventricular dyssynchrony) or the difference in timings between the left and right ventricles (interventricular dyssynchrony). This research focuses on intraventricular dyssynchrony of the left ventricle. Parts of the literature review from this chapter have been published in an invited editorial for the Journal of Nuclear Cardiology [11].

3.2 Mechanical Dyssynchrony

Mechanical dyssynchrony can lead to decreased left ventricular efficiency and has been linked to a worse prognosis [12–15]. On the other hand, an improvement in dyssynchrony is associated with improved survival, as shown in cardiac resynchronisation therapy (CRT) studies [14]. CRT therapy involves implanting a pacemaker into the chest. The pacemaker will detect any irregularities in the cardiac rhythm and emit electrical pulses to correct them. Electrical dyssynchrony was historically used as a surrogate for mechanical dyssynchrony, defined as a QRS duration of >120 ms measured from a 12 lead electrocardiogram (ECG). A wider QRS (>120 ms) would indicate a delay in the conduction, and the electrical activity takes longer than normal to travel through the conduction system. A normal QRS duration is between 90 - 120 ms. Electrical dyssynchrony is widely used in clinical decision making. For example, it is part of the decision criteria for heart failure treatments such as implantable cardioverter-defibrillator (ICD) and cardiac CRT, as defined by the European Society of Cardiology (ESC) heart failure guidelines [16]. However, it is now widely accepted that mechanical dyssynchrony can exist without the presence of electrical dyssynchrony [17]. Therefore, it is essential to be able to measure mechanical

dyssynchrony directly.

Mechanical dyssynchrony can be measured by different cardiac imaging techniques, including echo (2-D M-mode, spectral Doppler, and tissue Doppler imaging parameters), single photon emission computed tomography myocardial perfusion imaging (SPECT MPI), RNVG, and magnetic resonance imaging (MRI). Dyssynchrony assessment has the potential to help select the most appropriate treatment for each patient and improve prognosis. To date, measures of dyssynchrony from echo have led the field, but mechanical dyssynchrony has not yet been adopted into widespread clinical practice.

The main focus to date for dyssynchrony parameters in heart failure has been for predicting CRT response. This is driven by the fact that despite all the research that the selection criteria is based on [16], approximately 30% of patients who undergo CRT therapy do not benefit from the treatment [18]. Therefore, finding methods to predict who will respond would have significant clinical benefits. There have been many studies published investigating imaging parameters as predictors to CRT response with varying degrees of success [14, 18–22]. However, comparing the studies is complex due to the varying definitions of a responder to therapy, patient selection criteria and lead placement. Definitions of response to therapy include an increase in left ventricular ejection fraction (LVEF), change in end-systolic volume, or change in New York Heart Association Symptom Class, with many studies using a combination of all these parameters. In general, the patients labelled as non-responders have no measurable improvement, but it is unknown if the therapy or treatment has prevented further deterioration in this group. One issue when using imaging parameters as a marker of improvement is the associated reproducibility of the technique, which is often not addressed. For example, some studies use an improvement in Simpsons bi-plane LVEF of 5%, measured by echo, as the definition of response to therapy even though the reproducibility of this technique is approximately 10% [23]. Assessment of dyssynchrony will be further investigated in Chapter 8 to determine the effect and predictive value of dyssynchrony for patients with heart failure who are treated with beta-blockers.

Several studies demonstrate the potential of dyssynchrony assessment for breast cancer patients receiving cardiotoxic chemotherapy [24–28], but further research is required before it is fully adopted in any of the guidelines and routine clinical practice. The ESC guidelines for cardiotoxic cancer therapy acknowledge the potential of dyssynchrony, as measured by global longitudinal strain (GLS), to assess left ventricular dysfunction, but also states that there is not yet enough evidence to stop or alter cancer treatment based on these measurements [29]. Chapter 7 will further investigate this application of dyssynchrony.

In nuclear cardiology, dyssynchrony can be assessed using RNVG or SPECT MPI, measured from the average of many cardiac cycles, unlike echocardiography, where measurements are taken from a single beat. The myocardial wall thickness correlates to the change in maximum counts extracted from the myocardial region, allowing assessment of myocardial wall thickening from SPECT MPI. Amplitude and phase images can be created from the regional left ventricle

count changes during the cardiac cycle using a count based method, [30]. A Fourier transform can be applied to the time-activity curve from each voxel of the SPECT MPI over the cardiac cycle to create the phase image, with the resulting phase values relating to the time of myocardial contraction. Chen *et al.* proposed using phase SD and bandwidth of the phase histogram from SPECT MPI as measures of dyssynchrony [30], although the normal range may be software dependent [31]. Results from the Vision-CRT trial [32] demonstrated that an improvement in SPECT MPI dyssynchrony parameters predicts clinical outcome for patients undergoing CRT. SPECT MPI has the added advantage of being able to measure myocardial perfusion and LVEF, as well as dyssynchrony. Furthermore, this technique is well established, low cost, reproducible and readily available. While there is the disadvantage of the radiation dose compared to echo and MRI, the development and increased use of solid-state gamma cameras in nuclear cardiology have resulted in a significantly lower radiation dose to the patient than the conventional gamma camera.

There are fewer dyssynchrony studies published using RNVG imaging. However, there are published studies that have demonstrated some interesting results for predicting CRT response [33,34], predicting outcome for patients with dilated cardiomyopathy and narrow QRS [35], and assessing cardiotoxic response to cancer therapy [36]. RNVG dyssynchrony does not have the same dependence on geometric boundaries as SPECT MPI for assessing dyssynchrony and has a better temporal resolution.

3.3 RNVG Phase and Amplitude Images

Phase images that represent the timing of contraction can be created from RNVG images to provide additional information to assess ventricular function [37,38]. Figure 3.1 is an example of a time activity-curve that shows the change in activity within the left ventricle during the cardiac cycle. This example demonstrates normal emptying and filling of the left ventricle. As the ventricle contracts during systole, the blood in the chamber is pumped out, and the number of counts reduces. During diastole, the left ventricle begins to fill again. The R-R duration is measured in seconds but can be converted to degrees, where 360 degrees represents the length of one cardiac cycle. The timing of ventricular contraction, relative to the R wave of the ECG, can be estimated from a first harmonic fit of the time-activity curve for each pixel in the RNVG image to create a phase map. The phase angle defines the point in the time-activity curve where the Fourier function reaches its peak, representing the onset of contraction. A background threshold of 20% of the maximum pixel value is used to reduce the effect of noise within the phase image. A black pixel will replace any pixel with a value below the set threshold. A higher phase value in the image indicates delayed contraction within the region. It is also possible to create a dynamic cine image of the phase, setting the pixels with the same phase in each frame to a single colour. The pixels within the left ventricle should all be a similar phase value for a phase

image representing normal synchronous contraction. Any areas of dyssynchronous contraction will appear as delays in the phase images and phase histogram.

The example histogram shown in Figure 3.2 shows the frequency of phase angles for the pixels in the region of interest with the corresponding phase image in the top right of the figure. This is an example of a phase histogram for a patient with a normal phase image. First-order statistics such as mean phase and phase standard deviation can be calculated from the phase histogram to assess dyssynchrony [38, 39].

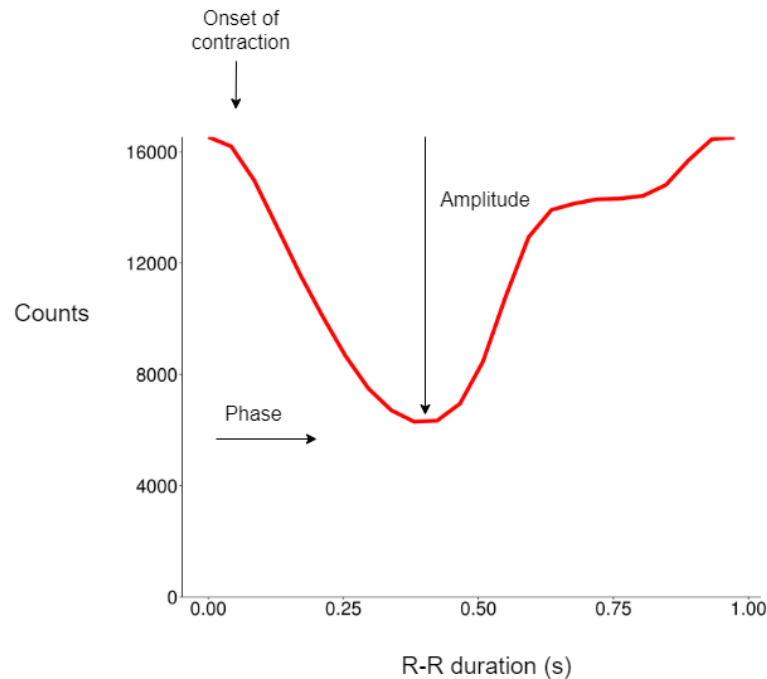


Figure 3.1: The time-activity curve shows the number of counts in the left ventricle over the cardiac cycle. This is a normal shape for a time-activity curve showing normal emptying and filling of the left ventricle. As the ventricle contracts during systole, the blood in the chamber is pumped out, and the number of counts reduces. The maximum change in counts is known as the amplitude and the phase refers to the onset of mechanical contraction.

Figure 3.3 shows the histogram of the left ventricular phase values with the corresponding phase image for four different patients. The atria can often be seen in the phase image, and because they contract at the opposite time from the ventricles, they have different phase values, as illustrated by different colours in the phase image. In Figure 3.3 (a), the phase image has a similar colour throughout the ventricles, and the phase histogram is a narrow peak. This is how a phase image for a patient with normal ventricular contraction would appear. Figure 3.3 (b) is an example of a patient who has had an MI. In the area of the MI, the muscle of the heart is damaged and unable to contract normally. The damaged region is being pulled in late during systole. The phase image shows areas with late phase values (green pixels) in the location of the MI. The associated phase image is no longer a narrow peak but has become more spread out. Any regional phase delays will broaden the phase histogram. Conduction abnormalities such

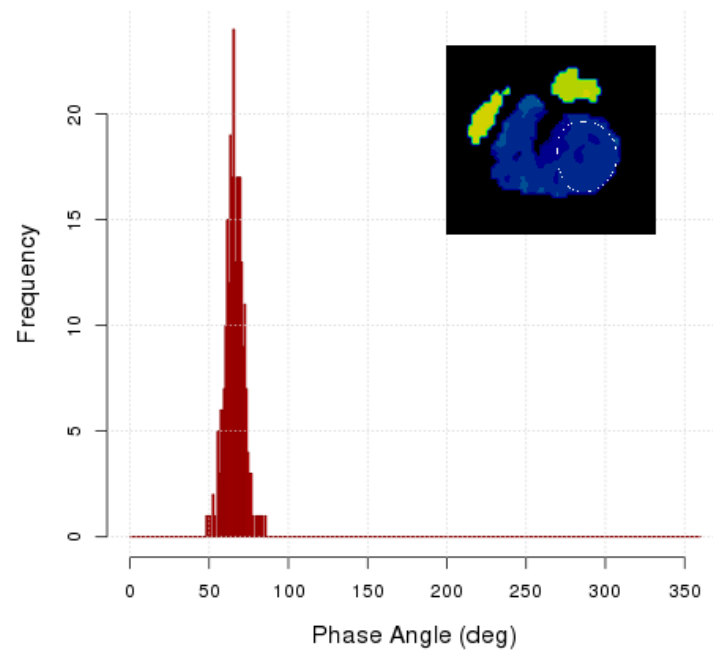


Figure 3.2: Phase histogram showing the frequency of phase angles for the pixels in the left ventricular region of interest. The corresponding phase image can be seen in the top right. This is an example of a phase histogram for normal phase.

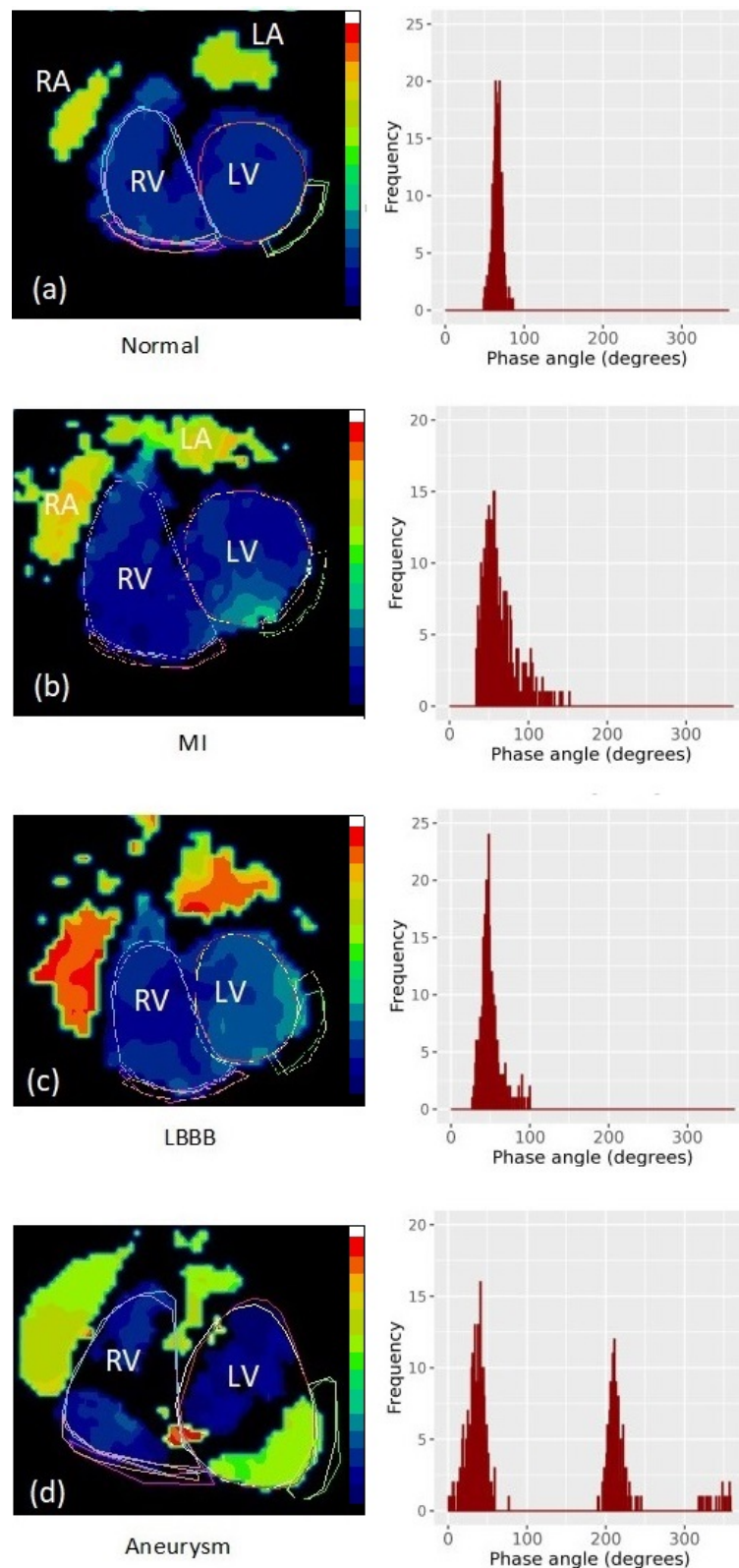


Figure 3.3: Example images showing phase pattern and associated phase histogram for (a) a normal patient with similar phase values throughout the ventricles, (b) a patient with previous myocardial infarction (MI) with late phase values in the area of a MI, (c) a patient with left bundle branch block, where there is a gradual change in phase values across the left ventricle and (d) a patient with a large aneurysm where two distinctly separate segments within the left ventricle are contracting at different times.

as left bundle branch block (seen in Figure 3.3 (c)) also have a distinct phase pattern. There is a gradual change in phase values across the left ventricle, which is also apparent on the phase histogram. Figure 3.3 (d) is a patient with an aneurysm. A left ventricular aneurysm is an area of thinned and weakened tissue in the heart muscle that bulges outward during contraction. Most often, ventricular aneurysms are caused by damage from a previous MI. It is evident from the phase image in Figure 3.3 (d) that a large part of the left ventricle is contracting at the same time as the atria instead of with the rest of the ventricle. There are two distinct parts within the left ventricle contracting at different times. Two separate peaks can be seen on the corresponding phase histogram. This has a severe impact on the efficiency of ventricular contraction. This technique could also detect more subtle phase abnormalities. Quantitative assessment of RNVG phase images will be investigated throughout this thesis.

Amplitude images can be created from time-activity curves to display the magnitude of contraction within the ventricles on a pixel by pixel basis. Amplitude images are also created using a background threshold of 20% to reduce the effect of noise in the image. Phase and amplitude images can help define the ventricles and valve plane when outlining the regions of interest for the measurement of ejection fraction. They are also more sensitive for detecting abnormal wall motion when compared to visual assessment of the blood pool images alone [40].

Figures 3.4 and 3.5 are examples of amplitude images with their associated phase image. Figure 3.4 is a patient with normal contraction. As expected, the pixels within the ventricles in the phase image are all a similar colour because the contraction is synchronous. In the amplitude image, red and white represent a bigger change in counts than the green pixels. The example shows that the lateral and apical segments are contributing more than the septum. This is a normal finding. Both the left and right ventricles pull the septum during systole, so the septum does not contract as much as the lateral and apical segments. An example of a patient with a large aneurysm is shown in Figure 3.5. As previously described, the corresponding phase image indicates two separate regions are contracting at opposite times within the left ventricle. The amplitude image for this example shows that the area with the aneurysm has a bigger change in counts during the cardiac cycle than the remainder of the left ventricle.

3.4 Dyssynchrony Measured From RNVG Phase Analysis

Various statistical parameters calculated from RNVG phase images have been established to quantify mechanical dyssynchrony. This section defines the parameters that will be investigated throughout this work.

3.4.1 Phase Standard Deviation

Most of the dyssynchrony parameters calculated from the RNVG phase are from the first-order statistics calculated from the phase histogram, such as phase standard deviation, which has the

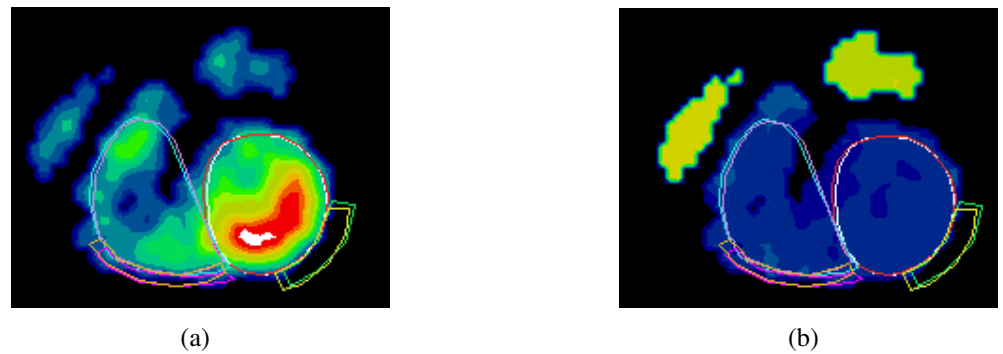


Figure 3.4: (a) Amplitude image, (b) phase image for patient with normal RNVG. In the amplitude image, red and white represent a higher change in counts than the green pixels. The lateral and apical segments are contributing more than the septum, because the septum is also being pulled by the right ventricle so can not contract as much as the lateral and apical segments.

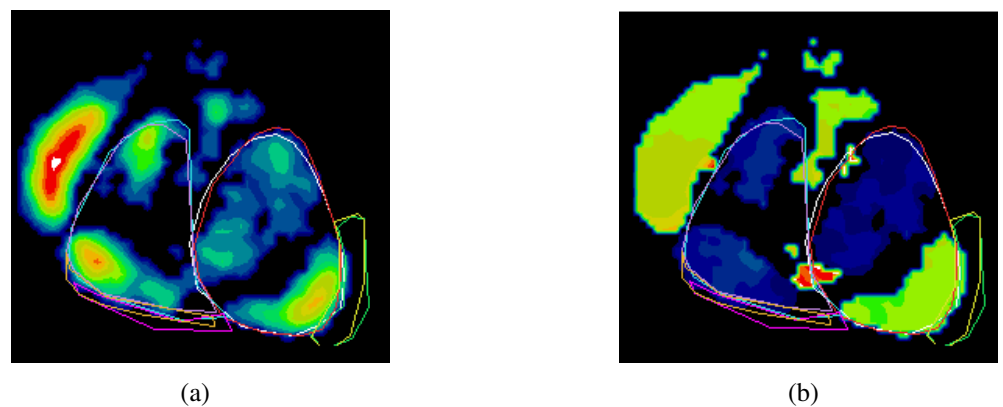


Figure 3.5: (a) Amplitude image, (b) phase image for patient with aneurysm. The phase image has two separate sections within the left ventricle, contracting at opposite times. The associated amplitude image shows that the area with the aneurysm has a higher change in counts during the cardiac cycle than the remainder of the left ventricle.

advantage of being simple to understand and easy to measure. In addition, it is accurate, highly reproducible [41, 42], and has been used in many published studies to quantify dyssynchrony. For example, Fauchier *et al.* [43] demonstrated that phase standard deviation was predictive of cardiac events in a group of patients with idiopathic dilated cardiomyopathy. Another study by Kerwin *et al.* [44] found that atrial sensed biventricular pacing improved left ventricular dyssynchrony as measured using phase standard deviation.

3.4.2 Synchrony and Entropy

O'Connell *et al.* derived synchrony as a measure of ventricular coherence (Equation 3.1) to describe the contraction of the ventricle using the phase and amplitude data extracted from RNVG images [45]. Synchrony is defined as the vector sum of the amplitudes divided by the scalar sum. A ventricle with completely synchronous contraction would have a synchrony value of 1 (Figure 3.6a), whereas for a completely asynchronous contraction the synchrony would be 0 (Figure 3.6b). Synchrony is defined as

$$\text{synchrony} = \frac{|\sum_{i=1}^N v_i|}{\sum_{i=1}^N |v_i|}, \quad (3.1)$$

where N = Number of pixels within the region of interest, v_i = vector defined by the phase and amplitude of the pixel.

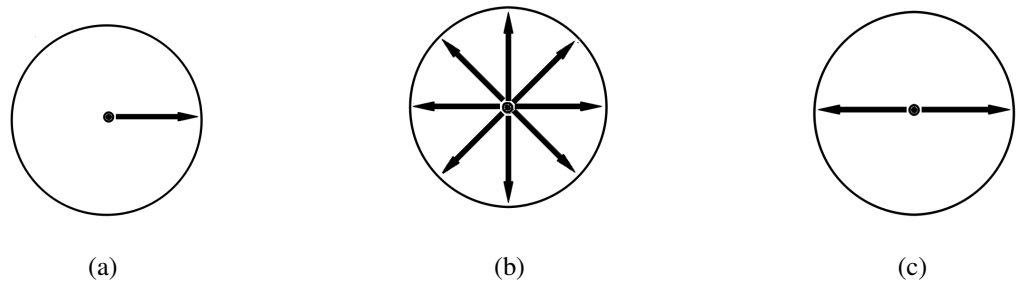


Figure 3.6: Example of phase vectors showing (a) completely synchronous phase, synchrony = 1, (b) completely random phase, synchrony = 0 and (c) two synchronous sub-regions synchrony = 0.

Entropy, as derived from Shannon information theory [46], can be used as a measure of randomness of contraction within the ventricle [45] as described in Equation 3.2. A higher value of entropy would indicate a more random contraction. When comparing a completely random contraction (Figure 3.6b) and a contraction where two sub-regions are synchronous (Figure 3.6c), the synchrony value would be equal. However, entropy can make this distinction. Entropy is defined as

$$\text{entropy} = -\frac{\sum_{i=1}^M p_i \log_2(p_i)}{-\log_2 M}, \quad (3.2)$$

where p_i = frequency of occurrence of each phase bin, M = total number of phase angle bins.

O’Connell *et al.* demonstrated that synchrony and entropy are superior to phase standard deviation for discriminating between normal and abnormal contraction [45]. However, synchrony and entropy are relatively new measures of dyssynchrony, and there are still very few published studies investigating these parameters. RNVG synchrony and entropy of the right ventricle were compared with echo and cardiac MRI for patients with arrhythmogenic right ventricular cardiomyopathy (ARVC) in a paper published by Johnston *et al.* [47]. The study found that synchrony and entropy of the RV successfully distinguished between ARVC and healthy controls and compared well with echo and MRI for ARVC diagnosis. One of the most interesting papers in this area is by Badhwar *et al.* [34], where synchrony and entropy were used to predict outcomes in a group of patients with advanced heart failure who were referred for CRT. In this study, the post CRT improvements in synchrony and entropy were significantly different between responders and non-responders. This study also suggested that baseline synchrony, but not entropy, could predict CRT response.

3.4.3 Approximate Entropy and Sample Entropy

Advanced statistical parameters, such as approximate entropy (*ApEn*) and sample entropy (*SampEn*), can also be used for quantitative assessment of the ventricular contraction. *ApEn* is a regularity statistic developed from Kolmogorov-Sinai entropy by Pincus [48], originally developed to measure irregularity in a time series. *ApEn* calculates the probability that a series of length m remains similar within a tolerance r at the next point in the data series. Unlike synchrony and entropy, *ApEn* and *SampEn* take into account the similarity of adjacent pixel values. *ApEn* is well established in other fields including gait analysis and heart rate variability, but has not previously been widely investigated for assessing ventricular contraction [49–56]. *ApEn* is defined as

$$ApEn = -(N - m)^{-1} \sum_{i=1}^{N-m} \ln \left(\frac{C_{i^{m+1}}(r)}{C_{i^m}} \right), \quad (3.3)$$

where N is the length of data, m is the sequence length, and r is the tolerance. $C_{i^m}(r)$ is the conditional probability that when a sequence is within the tolerance, then the next element will also be within tolerance.

For example, consider the following short sequence of pixel values

25, 24, 28, 29, 23, 30.

The pixel values are considered as a data series. Each group of ‘ m ’ pixels will be compared to every other group of ‘ m ’ pixels within the region of interest, including itself. If the group

is within the tolerance value r , it will be counted. This is carried out for every group of ' m ' pixels then repeated with groups of ' $m + 1$ ' to calculate C_{i^m} and $C_{i^{m+1}}$. To calculate $C_{i^m}(r)$ for this sequence using $m = 2$ and $r = 5$, each group of $m = 2$ pixels should be compared to every other group of $m = 2$ pixels. If they are within tolerance r (in this case $r = 5$), it should be counted as a match. The groups of $m = 2$ pixels for this series are listed below.

$$x_1 = 25, 24$$

$$x_2 = 24, 28$$

$$x_3 = 28, 29$$

$$x_4 = 29, 23$$

$$x_5 = 23, 30.$$

where N is the length of data, m is the sequence length, and r is the tolerance. $C_{i^m}(r)$ is the conditional probability that when a sequence is within the tolerance, then the next element will also be within tolerance.

Now consider x_1-x_1 , x_2-x_1 , x_3-x_1 , x_4-x_1 , and x_5-x_1 . x_1 has 3 matches within tolerance r in this data series, including itself. Therefore,

$$C_{1^m}(r) = \frac{\text{number of matches}}{(N - m + 1)} = \frac{3}{5} = 0.6$$

This would be repeated for each set of m pixels within the sequence to calculate $C_{i^m}(r)$, then repeated for $m+1$ to calculate $C_{i^{m+1}}(r)$. When counting the number of matches, *ApEn* includes a 'self match' of vectors creating a bias towards regularity. Several publications also suggest that *ApEn* lacks relative consistency, meaning that the value of *ApEn* can 'flip' when the input parameters are varied [57, 58]. For example, when using a low value of r , *ApEn* would be higher for a normal data series than for an abnormal data series, but using a higher value of r , *ApEn* can 'flip' and be lower for normal data compared to abnormal. For this reason, the input parameters (m and r) must be fixed when comparing data sets. Cullen *et al.* published the first paper applying *ApEn* to RNVG phase images. The study investigated *ApEn* for serial assessment of a small group of patients who received cardiotoxic chemotherapy [36]. This work found a significant change in ejection fraction and *ApEn* over the course of treatment.

Sample Entropy is a modification of *ApEn* described by Richman and Moorman [59]. Unlike *ApEn*, *SampEn* displays relative consistency regardless of sequence length and tolerance values used and is independent of data length. However, for data sets with less than 100 points, Richman and Moorman suggested that *SampEn* diverged from their predictions. Yentes and Hunt [57] investigated the use of *ApEn* and *SampEn* in gait analysis for data sets below 200 points. They suggest that both *SampEn* and *ApEn* are sensitive to the input parameters, particularly for short data sets. They found *SampEn* to be less sensitive to changes in data length

and have fewer problems with relative consistency. After accounting for differences in N , m and r , Yentes and Hunt demonstrated that chaotic data provided higher values of $ApEn$ but lower $SampEn$. $SampEn$ is defined as

$$SampEn = -\ln\left(\frac{B^{m+1}(r)}{B^m(r)}\right), \quad (3.4)$$

$$B^m(r) = (N - m)^{-1} \sum_{i=1}^{N-m} B_i^m(r), \quad (3.5)$$

where $B_i^m(r)$ = number of sequences of length m that are within tolerance r , excluding self matches, and $B^m(r)$ is the probability that two sequences of length m are similar.

Unlike $ApEn$, the $SampEn$ equation does not include a factor $1/(N - m)$, making it independent of the length of the series. The values of sequence length m and tolerance r that are used will markedly affect the results for both $ApEn$ and $SampEn$, so it is essential to optimise the input parameters for the data being considered [58, 60, 61]. At present, there is no established m , r or normal range for $ApEn$ or $SampEn$ applied to RNVG phase images. $SampEn$, has not been previously investigated for assessing left ventricular dyssynchrony from RNVG phase.

3.5 Conclusions

This chapter has introduced and defined the dyssynchrony parameters that will be investigated in this research. Some of these parameters are established in the field, such as phase standard deviation, while others, such as $ApEn$ and $SampEn$, are novel in cardiac imaging. There is currently no established normal range for $ApEn$ or $SampEn$ applied to RNVG phase images. For measures of dyssynchrony to be used routinely in clinical practice, it is clear that standardisation and a normal cut-off will need to be established for each parameter. There are several methods for assessing dyssynchrony within each imaging modality, and they are not necessarily equivalent. Optimising the input parameters is crucial for both $ApEn$ and $SampEn$. While there has been some discussion in the literature regarding parameter choice, there is currently no consensus on this subject. Mechanical dyssynchrony has potential for several applications over and above predicting CRT response. Some of these applications will be investigated in Chapters 7 and 8.

Chapter 4

Statistical Analysis and Machine Learning

4.1 Introduction

This chapter introduces the statistical tests and machine learning algorithms that will be applied in this research when assessing clinical data. The techniques described in this chapter will be used to compare various patient groups and build predictive models using dyssynchrony parameters from the radionuclide ventriculography phase images. Classification models will be created to predict the outcome for patients receiving cardiotoxic cancer therapy (Chapter 7) and patients with heart failure with reduced ejection fraction (Chapter 8). All data analysis and statistics used in this research were performed in R 3.6.3 (R Development Core Team, Vienna, Austria) [62–66].

Machine learning is a rapidly developing field for many applications, including medical imaging. The accelerated progress in this field is partly due to the increased available computing power and the potential to combine large amounts of clinical data. As a result, there has been significant interest in utilising machine learning in medicine to improve image processing and clinical decision making. There has been a particular interest in deep learning within medical imaging [67–70]. However, simpler machine learning algorithms can also be of benefit. Medicine is a complex field where patient outcomes depend on many factors, but creating models that can combine multiple variables can improve the predictive value of individual measures. This chapter focuses on classification algorithms using logistic regression and LASSO (Least Absolute Shrinkage and Selection Operator) regression techniques which will be used in Chapters 7 and 8.

4.2 Logistic Regression

Linear and nonlinear regression methods are often used in medical research to quantify and describe the relationship between variables. Linear regression is a simple type of regression where the relationship between variables can be described by a straight line. Logistic regression is

a supervised classification algorithm often used in machine learning. For supervised learning, the data contains variables and a known outcome. For example, the outcome may be hospital admission, the presence of disease, or death. The model can be built using either qualitative or categorical variables, and a threshold can be selected to determine the decision boundary. A logistic regression model can be created using interaction terms between variables as well as individual variables. If there is an interaction, the relationship between one variable and the outcome will depend on the value of a second variable and vice versa. Adding an interaction term to a model can change the interpretation of the coefficients. One of the advantages of using logistic regression over other methods is that it is simple to interpret compared with more advanced machine learning models. Logistic regression is commonly used in medicine to classify data into two or more labelled outcomes.

The logistic function is defined by

$$\text{logistic function} = p(x) = \frac{e^{\beta_0 + \beta_1 X}}{1 + e^{\beta_0 + \beta_1 X}}, \quad (4.1)$$

where β are regression coefficients. β_0 = the intercept term, β_1 = the slope, and X = the predictor. The regression coefficients are estimated in the model using training data. The intercept term is the expected mean value of Y when the predictor X , equals 0.

$$\text{odds} = \frac{p(X)}{1 - p(X)} = e^{\beta_0 + \beta_1 X} \quad (4.2)$$

The odds is the ratio of the probability of an event occurring to the probability of the event not happening. The odds ratio measures the association between a predictor and an outcome. If X is increased by one unit, the log odds ratio will change by β_1 . If β_1 is positive, then an increase in X will be associated with an increase in $p(X)$, and negative β_1 will be associated with a reduced value of $p(X)$. Taking the log of both sides of equation 4.2 gives the log odds (also known as logit).

$$\log \text{ odds} = \log \left(\frac{p(X)}{1 - p(X)} \right) = \beta_0 + \beta_1 X \quad (4.3)$$

Multiple logistic regression can also be used when there are multiple predictors, as described by

$$\log \left(\frac{p(X)}{1 - p(X)} \right) = \beta_0 + \beta_1 X + \dots + \beta_n X_n, \quad (4.4)$$

where $X = (X_1, \dots, X_n)$ are n predictors. The logistic function can then be written as

$$\text{logistic function} = p(x) = \frac{e^{\beta_0 + \beta_1 X_1 + \dots + \beta_n X_n}}{1 + e^{\beta_0 + \beta_1 X_1 + \dots + \beta_n X_n}}, \quad (4.5)$$

The maximum likelihood method is used to fit the model. This method will find estimates for the regression coefficients that will maximise the likelihood that the results described by the model will match the observed data. The output of a logistic regression model is converted into a categorical outcome using a sigmoid function (also known as a logistic function) as shown in Figure 4.1. The function shown in this figure is an 'S' shape that cuts through the y-axis at 0.5, defining the decision boundary as 0.5. Therefore, if the predicted probability (t) is ≥ 0.5 , it will be mapped to class 1, and if it is < 0.5 , it will be mapped to class 0. The sigmoid function can be used to map a prediction to a probability between 0 and 1. The equation below describes the sigmoid function

$$\text{sig}(t) = \frac{1}{1 + e^{-t}}, \quad (4.6)$$

where $\text{sig}(t)$ = an output between 0 and 1 and t = the algorithms prediction.

Consider the following example of a logistic regression model to assess the risk of death in coronary bypass patients from Anderson *et al.* [71]. This model contains two predictors - age and history of renal insufficiency. The predictors and coefficients are shown in Table 4.1. The coefficients for age and history of renal insufficiency are positive, meaning that an increase in age or history of renal insufficiency will increase the chance of death.

Table 4.1: Example logistic regression results

Predictor	Coefficient
Intercept	-8.868
Age	0.073
History of renal insufficiency	1.162

To calculate the odds of a coronary artery bypass patient dying using this model, multiply the coefficient for age by the age, multiply the coefficient for renal insufficiency by 1 if renal insufficiency is present or 0 if there is no history of renal insufficiency, and add these terms to the intercept value to obtain the log odds (or logit) of death. The log odds is then converted to the odds by taking the exponential to calculate the probability of death. For example, for a 65 year old patient with renal insufficiency, the log odds would be calculated as follows,

$$\begin{aligned}
 \log \text{ odds} &= (\text{Age} \times 0.073) + (\text{Renal insufficiency} \times 1.162) - 8.868 \\
 &= (65 \times 0.073) + (1 \times 1.162) - 8.868 \\
 &= -2.961
 \end{aligned}$$

Taking the exponential of the log odds gives an odds value of approximately 0.052. Logistic regression is usually reported in terms of the odds rather than the probability of the outcome, but there is a direct relationship between the probability and the odds. The probability can be calculated from the odds as shown in the equation below,

$$\text{Probability} = \frac{\text{odds}}{\text{odds} + 1} \quad (4.7)$$

Therefore, the probability of death in this example would be $0.052 / (1 + 0.052) = 0.049 = 5\%$

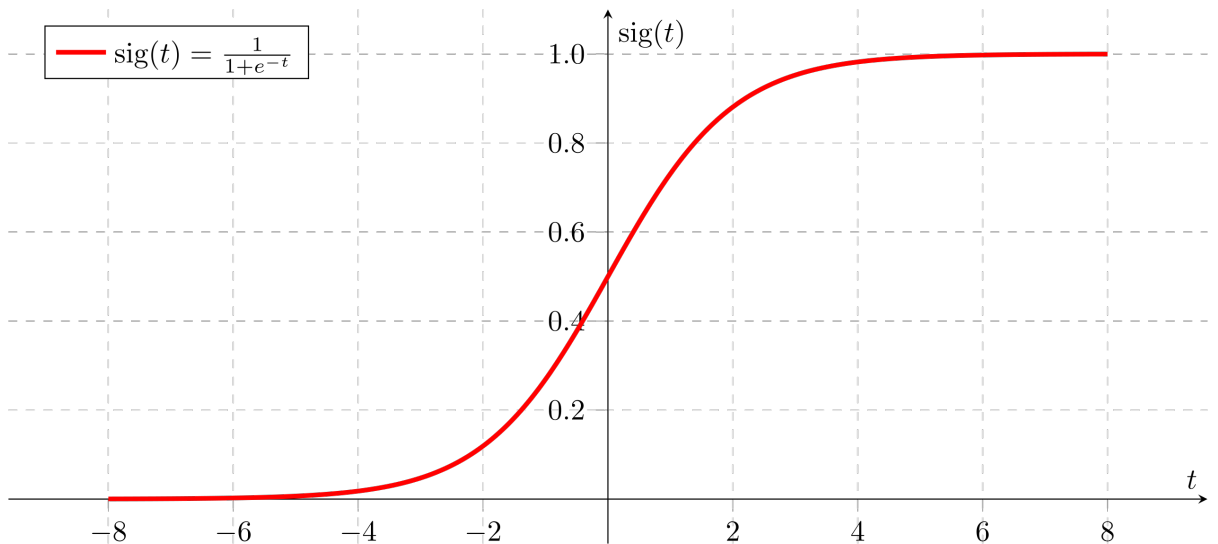


Figure 4.1: The sigmoid function that is used in logistic regression to map a prediction to a probability between 0 and 1. The decision boundary is set to 0.5 on the y-axis.

4.3 Ridge and LASSO Regression

Linear regression is a popular and widely used statistical method, but it has some limitations. One of the limitations of a regression model is the issue of over-fitting the data. One solution to this problem is to use either ridge regression or LASSO. Ridge regression and the LASSO are regression techniques that constrain the regression coefficient estimates, causing them to shrink towards zero. This has the effect of significantly reducing their variance.

Ridge regression uses a similar method to least squares, but the coefficients are estimated by minimising a different quantity. The least-squares fitting procedure estimates the coefficients (β) that will minimise the residual sum of squares (RSS), as described in equation 4.8.

$$RSS = \sum_{i=1}^n \left(y_i - \beta_0 - \sum_{j=1}^p \beta_j x_{ij} \right)^2, \quad (4.8)$$

where β_0 = the intercept term, β_j = regression coefficient for the j^{th} predictor, y_i = outcome, x = a predictor, p = number of predictors, n = number of observations.

Ridge regression will select coefficients that will minimise equation 4.9,

$$\sum_{i=1}^n \left(y_i - \beta_0 - \sum_{j=1}^p \beta_j x_{ij} \right)^2 + \lambda \sum_{j=1}^p \beta_j^2 = RSS + \lambda \sum_{j=1}^p \beta_j^2, \quad (4.9)$$

where λ is a tuning parameter that must be determined separately. The second term, $\lambda \sum_{j=1}^p \beta_j^2$, is known as the shrinkage penalty. If λ is equal to zero, the penalty term will have no effect, and the ridge regression will be the same as the least-squares estimates. Selecting the optimal value of λ is crucial. The penalty will shrink all coefficients towards zero but never equal zero, meaning the final model will include all predictors.

LASSO is a commonly used regression technique that has been used for many applications, including cardiac imaging [72–74]. It is similar to ridge regression, but it penalises the sum of the coefficients absolute values, as shown in Equation 4.10, resulting in many of the coefficients being zeroed and excluded from the model. LASSO models perform variable selection, resulting in a simpler model to interpret, using a subset of the predictors.

$$\sum_{i=1}^n \left(y_i - \beta_0 - \sum_{j=1}^p \beta_j x_{ij} \right)^2 + \lambda \sum_{j=1}^p |\beta_j| = RSS + \lambda \sum_{j=1}^p |\beta_j|, \quad (4.10)$$

A LASSO model will be used for feature selection to identify a subset of predictors related to the response that will subsequently used to fit a model in Chapter 8.

4.4 Cross-Validation

Machine learning algorithms must be carefully trained to avoid inaccuracies that can lead to a poorly performing model. A common problem with statistical models is over-fitting to the training data. This could lead to a fit like the example shown in Figure 4.2. This figure shows the same data with two different fits. The first one has a linear fit that provides a good separation between the red and blue points, and the second plot is an example of an overfitted model. This model would be 100% accurate for the training data but would not perform well for unseen data.

Overfitting can be caused by a number of things, including a poorly selected training set or using too many parameters in the model.

Cross-validation is a method used to reduce over-fitting and improve a model when there is limited data for testing. K-fold cross-validation is a technique where the data is split into k groups of roughly equal size. A model is trained with the remaining $k-1$ groups for each group, and testing is performed on the remaining group. This results in k measures of the model performance, which can then be averaged to provide the k -fold performance. Cross-validation is often carried out using 5 or 10-folds. An example of 5 fold cross-validation is illustrated in Figure 4.3. This illustration shows that 80% of the full data set is used to build the model, and the remaining 20% is used for testing. This is then repeated with the same data using a different split, meaning a new model is created using a different 20% of the data kept back for testing. For 5-fold cross-validation, this process is carried out 5 times, and for each iteration, different data is used for testing. Cross-validation can be performed for any defined number of folds, and repeats can also be used. For example, in 5-fold cross-validation with 3 repeats, the process previously described would be repeated 3 times. The final model would be the average of all of the models. New unseen data should be used to assess the final statistical model where possible.

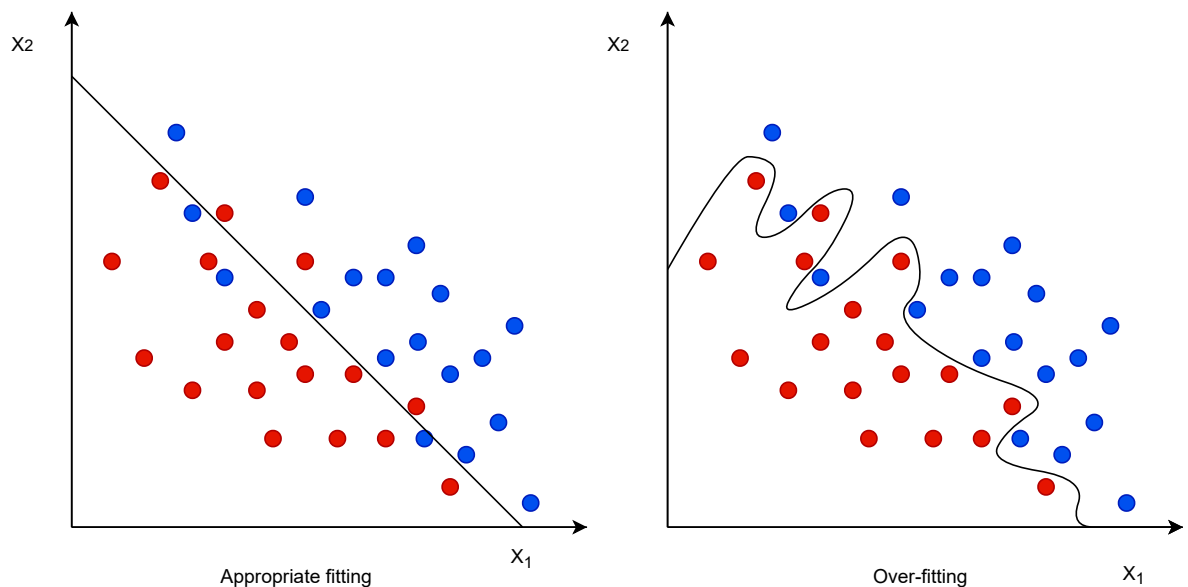


Figure 4.2: Example data showing an appropriate fit (left) to discriminate between the red and blue points and a model that has been over-fitted to the training data (right). The more flexible the model, the more likely it will overfit the training data. This example is for illustrative purposes and has not been fitted mathematically.



Figure 4.3: Illustration of the data split for 5-fold cross-validation. Each iteration is performed using a different test-train split, and the average results are reported.

4.5 Evaluating Model Performance

The performance of a machine learning model can be evaluated using several measures, including the mean squared error (MSE), accuracy, and area under the receiver-operator curve (AUC). These measures allow comparisons to be made between different models.

Mean Squared Error

MSE measures how close the regression line is to a set of data points. The distance from each data point to the regression line is the error, and it is squared to ensure there are no negative values. MSE measures the average of the squares of the errors, described by the equation below.

$$\text{MSE} = \frac{1}{n} \sum_{i=1}^n (y_i - f(x_i))^2, \quad (4.11)$$

where n is the total number of observations, y_i is the true response for the i th observation, and $f(x_i)$ is the prediction for f for the i th observation. An ideal model will have a low MSE using previously unseen test data.

Accuracy

The accuracy measures the proportion of correct results in the selected population, calculated from the equation below.

$$\text{Accuracy} = \frac{(TP + TN)}{(TN + FP + FN + TN)} = \frac{(TP + TN)}{\text{total number of patients}}, \quad (4.12)$$

where TP = true positives, TN = true negatives, FP = false positives, and FN = false negatives.

Sensitivity and Specificity

Sensitivity is the ability of a test to correctly identify those with a positive result (true positive rate), and specificity is the ability of a test to identify those with a negative result (true negative correctly rate).

$$\text{Sensitivity} = \frac{TP}{(TP + FN)} = \frac{TP}{\text{Total with disease}}, \quad (4.13)$$

$$\text{Specificity} = \frac{TN}{(TN + FP)} = \frac{TN}{\text{Total without disease}}, \quad (4.14)$$

where TP = true positives, FN = false negatives, TN = true negatives, and FP = false positives.

Receiver-Operator Characteristics

Receiver-operator characteristics (ROC) is a method to compare diagnostic tests, originally developed during World War II as part of the radar system to differentiate between enemy aircraft and signal noise (e.g. flocks of geese). ROC is a plot of the true positive rate (sensitivity) against the false positive rate (1 - specificity), as seen in the example in Figure 4.4. The red dotted line represents an AUC of 0.5 in Figure 4.4. This would suggest there is no discrimination, and the chances of predicting an outcome would be no better than a random classifier. A perfect algorithm, with 100% sensitivity and 100% specificity, would have an AUC value of 1, represented by the blue line in this example. In contrast, an algorithm that is wrong every time would have an AUC of 0. The area under AUC is commonly used in medical imaging to assess and compare different techniques. Accuracy and AUC will be used to assess the classification models in Chapters 7 and 8.

4.6 Comparing Samples

It is common in medical statistics to compare a variable for two or more groups of patients. Several different tests can be used to determine if there is a statistical difference between these groups. The appropriate test depends on the number of groups in the comparison and the distribution of the data. Firstly, to determine if the data is normally distributed, a Shapiro-Wilk

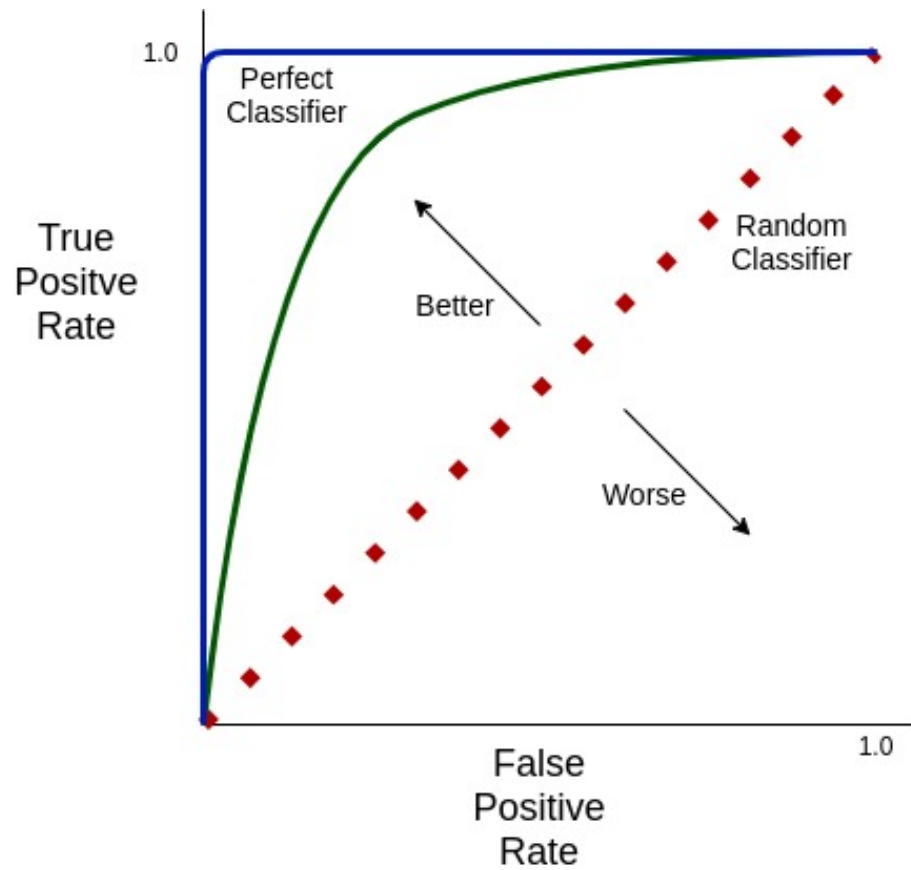


Figure 4.4: An example of an ROC curve. The red dotted line represents a random classifier, with an AUC of 0.5 and the green line represents a good classifier. The perfect algorithm is represented by the blue line and would have an AUC of 1, representing 100% sensitivity and 100% specificity.

normality test can be used for continuous data, or a Chi-Squared test can be used for categorical data. Henze-Zirkler test can be used to test multivariate normality. If the data is normally distributed, then a two-sample t-test can be used to compare the means of two samples or a one-way analysis of variance (ANOVA) test for three samples. If the data does not have a normal distribution, it is appropriate to use a non-parametric test. The Wilcoxon signed-rank test would be selected for two groups or the Kruskal-Wallis test for comparing the means of three groups. The resulting p-values from these tests are often used in medicine to summarise the results. In general, $p < 0.05$ is considered significant, meaning the difference is unlikely to have occurred by chance. These tests will be used throughout this research in Chapters 5 - 8.

Chapter 5

Software and Parameter Optimisation

5.1 Introduction

This chapter describes the software that was written to calculate the dyssynchrony parameters from radionuclide ventriculography (RNVG) phase images and the optimisation of approximate entropy (*ApEn*) and sample entropy (*SampEn*). The optimisation work was performed using R 3.6.3 [62, 75]. The work described in this chapter was the first published optimisation of *ApEn* applied to RNVG phase images [76].

5.2 Software

A program was developed using R 3.6.3 to calculate synchrony, entropy, *ApEn*, *SampEn*, mean phase and standard deviation from DICOM phase images of both the left and right ventricles. DICOM stands for Digital Imaging and Communications in Medicine, and it is the standard image format used in medical imaging. A DICOM image file contains a header and image data within a single file. This image format was used to ensure the program could be used for images from different nuclear medicine software packages and was not restricted by a proprietary image format.

In addition to the R program, a shell script was written to prepare the input images within the Link Medical MAPS 10000 system (Link Medical Ltd., Hampshire, UK) converting amplitude, phase and ROI masks to a DICOM format that can be easily read into the R script. The output of the code includes the left ventricular and right ventricular phase regions of interest that are used in the calculation, the phase spread histograms, and the dyssynchrony parameters. The overall structure of the code is illustrated in Figure 5.1. The region of interest that has been outlined, plus the phase and amplitude images, are read in the code and defined as a matrix. Both images are masked by the region of interest to set a value of zero for all pixels outside the region of interest. The function within the code which is used to calculate the dyssynchrony parameters is shown in Figure 5.2. The pixel values in the matrix are converted from degrees to radians for

the calculation and the matrix is converted into a data series. A phase histogram with 1 degree bins is created, allowing the probability of each phase angle and entropy to be calculated. The vector and the scalar sum of the phase is then calculated before synchrony is assessed. For the calculation of $ApEn$ and $SampEn$, a matrix is created containing rows of the sequences to be compared. There is a function within the code to calculate $ApEn$ and $SampEn$ as seen in Figure 5.2. Each sequence of m pixels is then compared to every other group of m pixels. The loop in the code allows for this comparison to be carried out for every group of m pixels and the number of matches counted before it is repeated. The $SampEn$ calculation is not shown in the flowchart, but it is calculated within the function using the same method as the $ApEn$ calculation. The final results are then printed to a text file. An additional output file is created as shown in Figure 5.3. This file displays the original phase and amplitude images that were read into the code. It also shows the left and right ventricular phase images after the region of interest has been applied and the phase histograms for both left and right ventricles.

5.2.1 Software Validation and Testing

Extensive testing was carried out using simple examples and sample data from the original reference authors, where available, and direct comparison to independently written code. Various combinations of sequence length m and tolerance r have been tested, giving confidence in the results of the code.

5.2.2 Generated Data

In order to gain full control of the input data, a Monte Carlo generator based on a simple repeated random number sampling algorithm was developed using R 3.6.3. Pixels in a chosen region of interest were divided into sixteen radial segments as seen in the image in Figure 5.4, with the phase value for each pixel assigned randomly according to a user-defined probability distribution function for each segment. This was implemented with Gaussian probability distribution functions for which the user would define the mean and standard deviation of the phase values. Pixels outside of the left ventricle region of interest were set to zero and excluded from the calculations. The region of interest size and pixel values of the simulated data were based on clinical data, to ensure the results were applicable across the clinical range of expected values. Simulated normal and myocardial infarction (MI) phase images were created to investigate the effect of the input parameters. Examples of normal and MI generated left ventricular phase images can be seen in Figure 5.5. These images were created based on the phase and standard deviation of clinical images. The simulated normal has similar pixel values of phase throughout the region, represented by the blue pixels. However, the simulated MI image has many pixel values which do not have the same phase value. This represents a delay in the timing of contraction for these areas. In this example, both ventricles are the same size. However, the radius

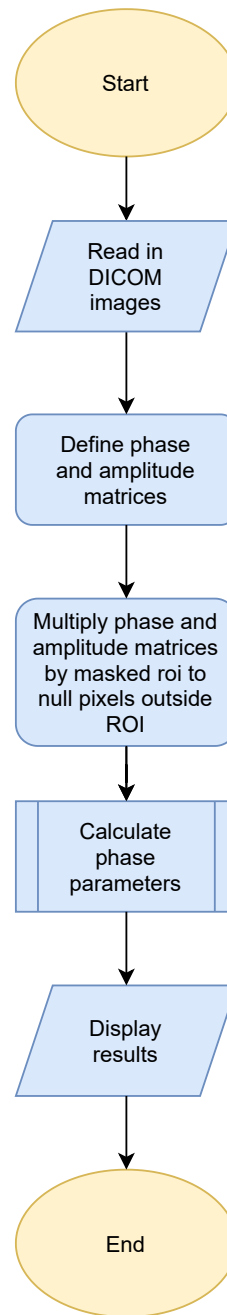


Figure 5.1: Overview of R code used to extract phase parameters. Phase and amplitude images are read into the code in DICOM format. The images are then masked by the region of interest to zero the pixels outside of the region. The phase parameters are then calculated and the results displayed.

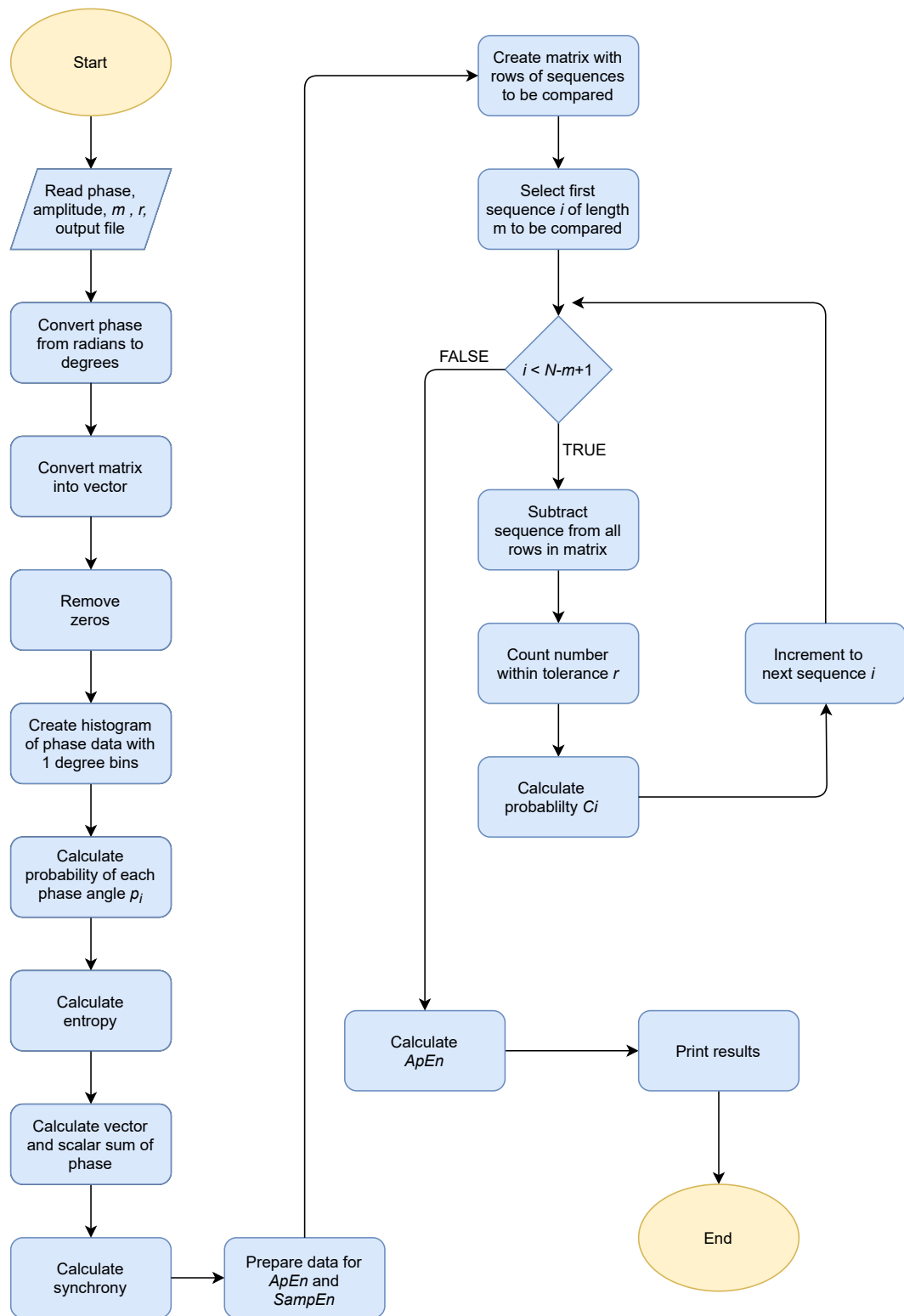


Figure 5.2: Function within R code used to calculate phase parameters for multiple regions of interest. The phase pixel values are converted from radians to degrees, and the image matrix is converted into a 2D sequence before the calculations. Phase histograms for both the left and right ventricles are created with 1 degree bin width. Synchrony and entropy are calculated, then a loop is used to compare a sequence of m pixels to every other sequence of m pixels for the $ApEn$ and $SampEn$ calculations. The calculated phase parameters are then printed to the screen and saved in a text file.

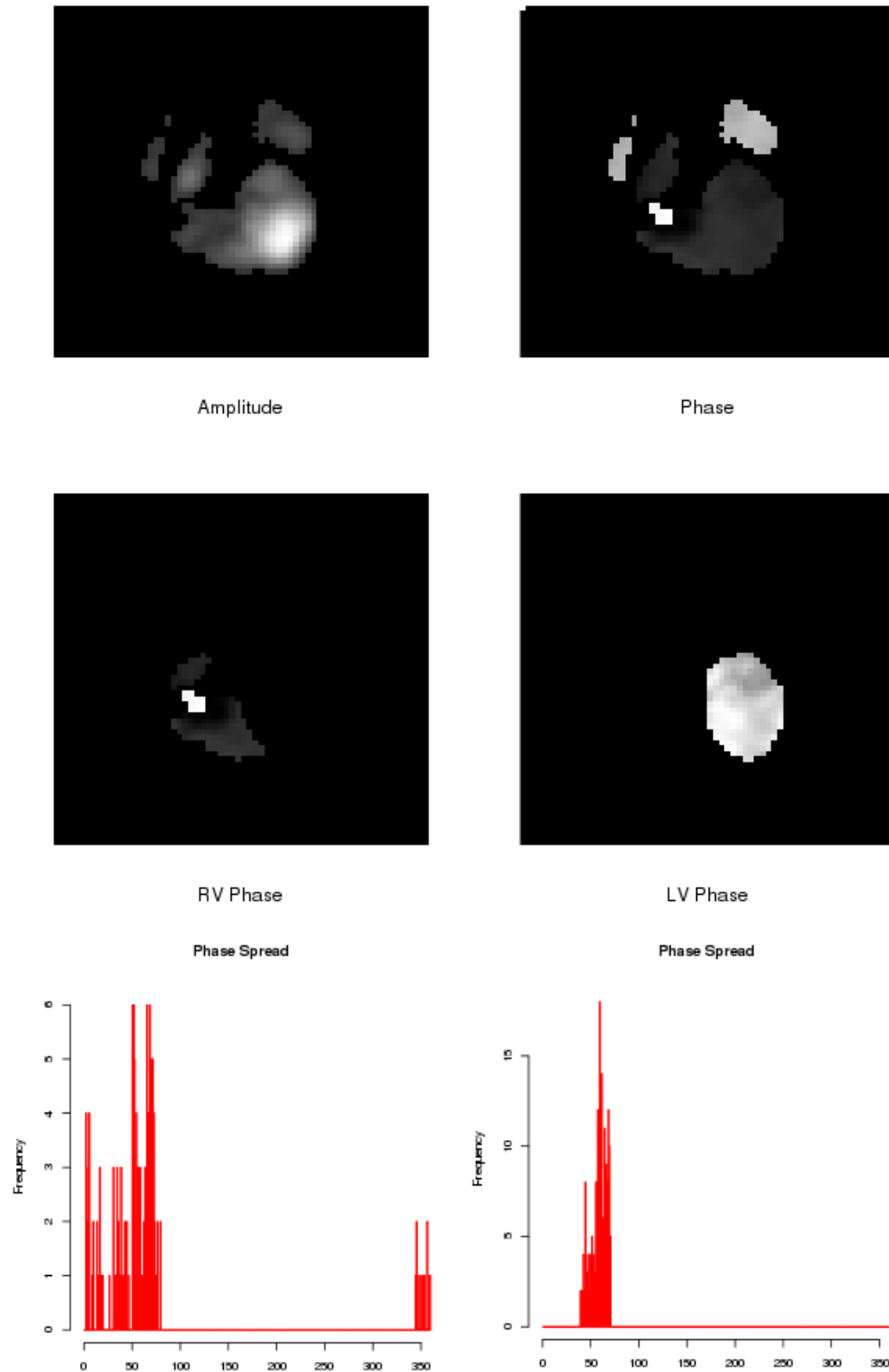


Figure 5.3: Example output image from R code showing the phase and amplitude images that were read into the code, the phase within the selected regions of interest for the left and right ventricles, and the phase histograms for left ventricle (bottom right) and right ventricle (bottom left). The phase histogram is a narrow peak for the left ventricle, suggesting it is normal. The right ventricle has two separate peaks on the histogram.

of the simulated ventricles can be increased or decreased.

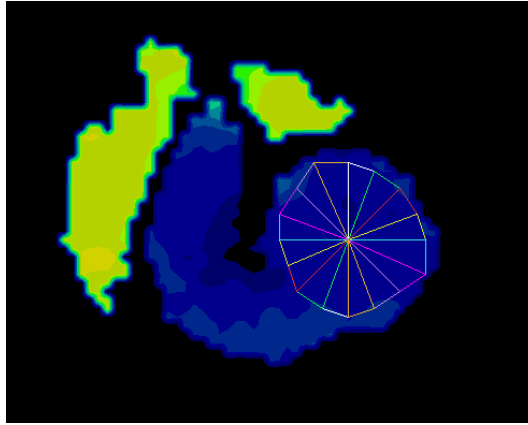


Figure 5.4: Phase image with radial segments, used to acquire mean and standard deviation of the phase for each of the 16 segments. Simulated data was then created in a 16 segment model using phase values based on the patient data.

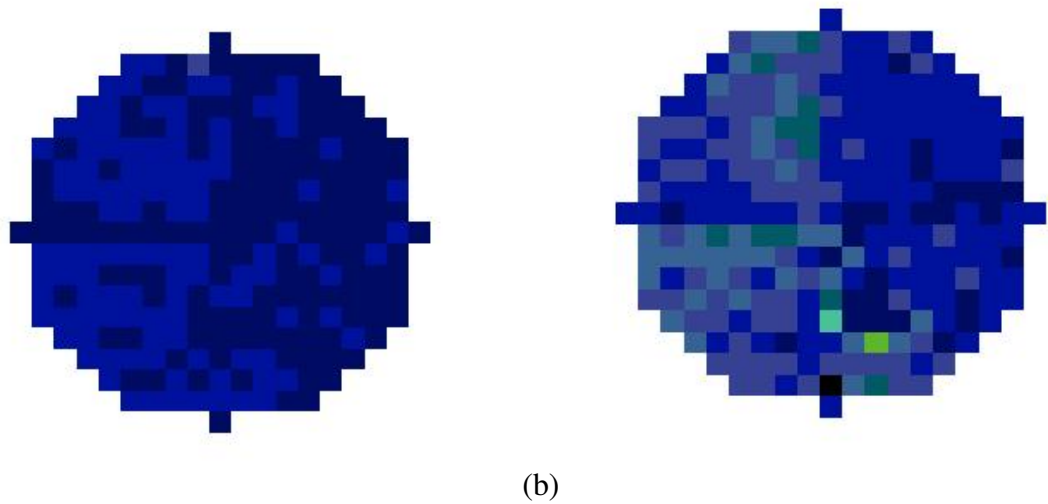


Figure 5.5: Examples of generated images to represent (a) normal phase within the left ventricle ROI and (b) to represent abnormal phase due to the presence of an MI. These images are generated based on mean phase and standard deviation from clinical images.

5.3 Selecting Sequence Length (m) and Tolerance (r)

$ApEn$ and $SampEn$ require values of sequence length m , and tolerance r , to be selected for the calculations. The values chosen will significantly affect the results, so it is important to optimise the input parameters for the application. $ApEn$ and $SampEn$ were calculated for varying values of sequence length m and tolerance r to demonstrate the effect of these input parameters. Some

publications suggest using a value of r between 0.1 - 0.2 of the standard deviation of the dataset [48, 77]. However, for improved consistency, it is better to use a constant value of r [60]. For the groups of patient data used in this work, the average standard deviation of the phase pixel values was 7.9 degrees for the normal group and 16.1 degrees for the MI group. 0.1 - 0.2 times the standard deviation for this data would suggest a range of r between 0.79 and 3.22 degrees, which was initially used as a starting point. Most published papers use $m = 2$, although there is limited justification for this choice in the literature. The final range tested was m between 1 and 5, with r from 0.25 degrees extending until $ApEn$ approached zero for a normal phase image.

The initial optimisation was carried out using simulated images representing a normal and MI phase pattern. This was then repeated using clinical images for normal (187 patients), MI (164 patients) and left bundle branch block (LBBB) (112 patients). The patient groups were defined by their clinical diagnosis, so some of the MI patients may still have normal, or close to normal, left ventricular function with a normal phase image.

The variation of $ApEn$ with sequence length m and tolerance r is shown in Figure 5.6. The plots demonstrate that both m and r affect the value of $ApEn$. As the tolerance r is increased, $ApEn$ reaches zero for the normal data. The plot for the abnormal phase image also decreases towards zero, but after the peak $ApEn$ value, the abnormal phase image still has a higher value of $ApEn$ for the same r value. Increasing m has the effect of changing the maximum $ApEn$ value. If the chosen m is too large, $ApEn$ will be zero. This is not unexpected because at higher values of m there will be fewer matches, and $ApEn$ will decrease towards zero, meaning there would not be sufficient separation to distinguish between normal and abnormal phase images. The effect of m and r for $SampEn$ can be seen in Figure 5.7. As can be seen in this Figure, the selection of m and r will have an effect on the value of $SampEn$. Some combinations of m and r values will produce an infinite value of $SampEn$ (represented as the white areas on Figure 5.7), particularly at higher m values. As r is increased, $SampEn$ will tend towards zero. When m is increased, the number of r values that produce infinite $SampEn$ increases. It is important to avoid these combinations to give a meaningful value of $SampEn$ that can be used for comparison.

The plots in Figure 5.6 and Figure 5.7 illustrate the importance of optimising m and r and suggests that a value of m equal to 1 or 2 would be most appropriate. However, a value of 1 would result in reduced dependence on the spatial relation of each pixel. For this reason, a sequence length of $m = 2$ was chosen.

$ApEn$ was calculated and plotted for simulated normal and MI phase patterns using $m=2$ and a range of r to determine the optimal value of r , as shown in Figure 5.8. These graphs demonstrate that $ApEn$ increases from zero, peaks, then decreases gradually to zero again as r is increased. The maximum discrimination between the two groups that are plotted is $r = 1.75$. Importantly, there is a value of r where the $ApEn$ calculated from both normal and MI images is equal, emphasising the need for using an appropriate value of r . The peak in each plot on Figure 5.8 represents the 'flip point'. If a value of r is selected that is below the 'flip point', then

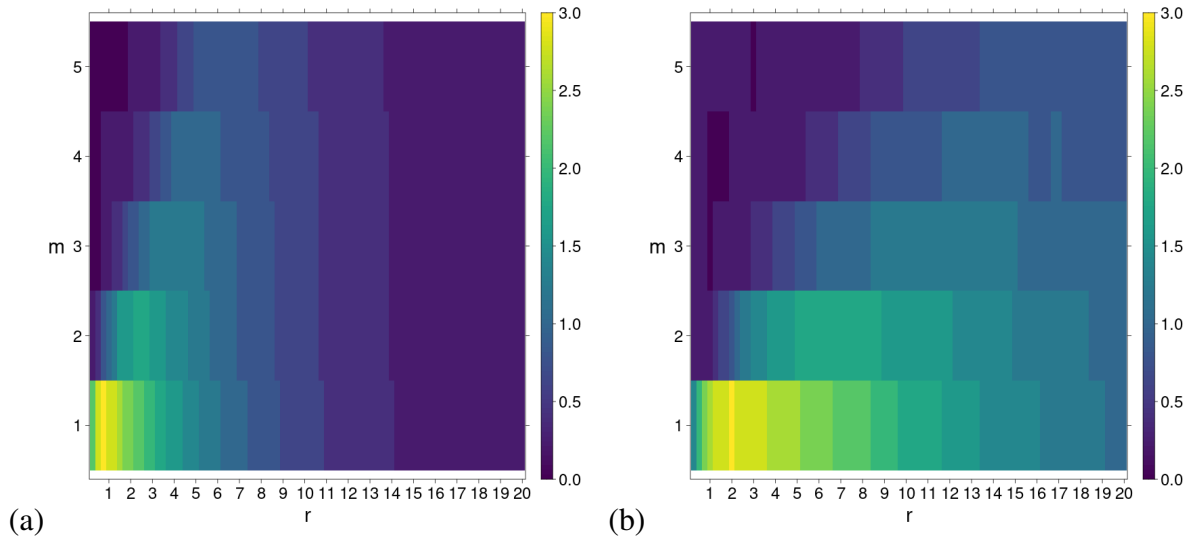


Figure 5.6: Simulated data demonstrating how $ApEn$ varies with m and r for (a) normal phase image and (b) a phase image for an MI

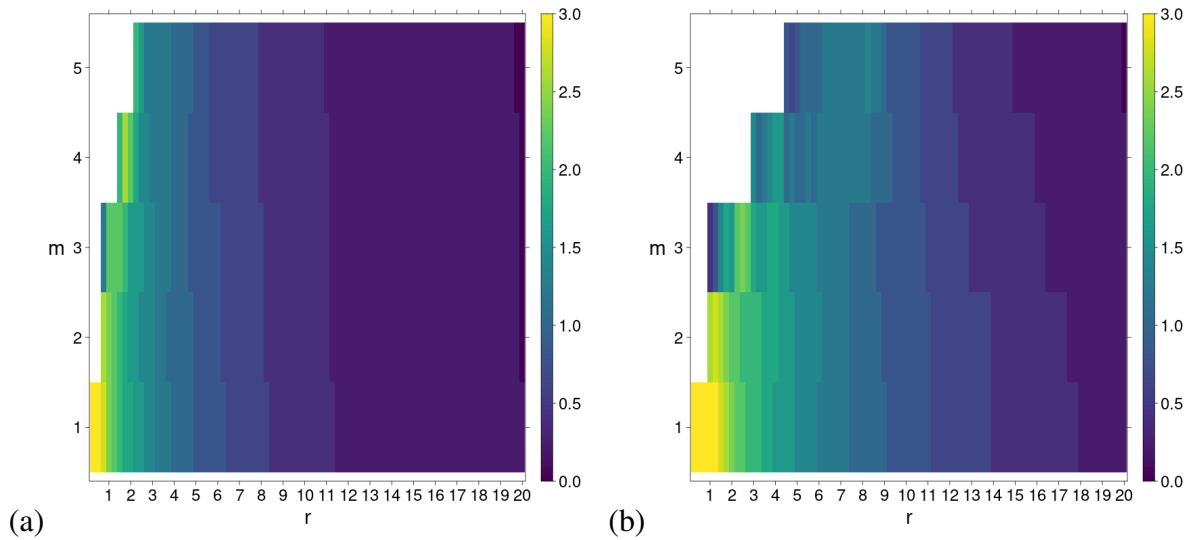


Figure 5.7: Simulated data demonstrating how $SampEn$ varies with m and r for (a) normal phase image and (b) a phase image for an MI. The white areas represent an infinite $SampEn$ value.

a higher $ApEn$ is normal, whilst if a larger value of r is used, a higher $ApEn$ would suggest that the phase is abnormal. These results are consistent with the literature, which suggests that $ApEn$ can flip when the input values are changed [60].

The dyssynchrony calculations and plots were repeated using patient data to confirm the results achieved with the simulated data. Plotting the results of the normal, MI, and LBBB patient groups (Figure 5.9) shows that the maximum discrimination for this group is at $r = 1$, and the point where all three patient groups had equal $ApEn$ was at $r = 2.75$. The normal, MI and LBBB plots in this figure represent the average $ApEn$ for a large number of patients as previously described. The graph shows that the normal group had the highest $ApEn$ before the

peak (also referred to as the 'flip point') and the lowest $ApEn$ of the three groups after the 'flip point'. The most critical point when considering the selection of input parameters is avoiding the area where abnormal and normal are equal and avoiding the 'flip point'. This point on the graph will vary, depending on how 'abnormal' the phase is. At this point, work was continued with two values of r , $r = 1$ and $r = 7$. These values were chosen because they provided adequate separation between normal and abnormal phase but were not close to the 'flip point'.

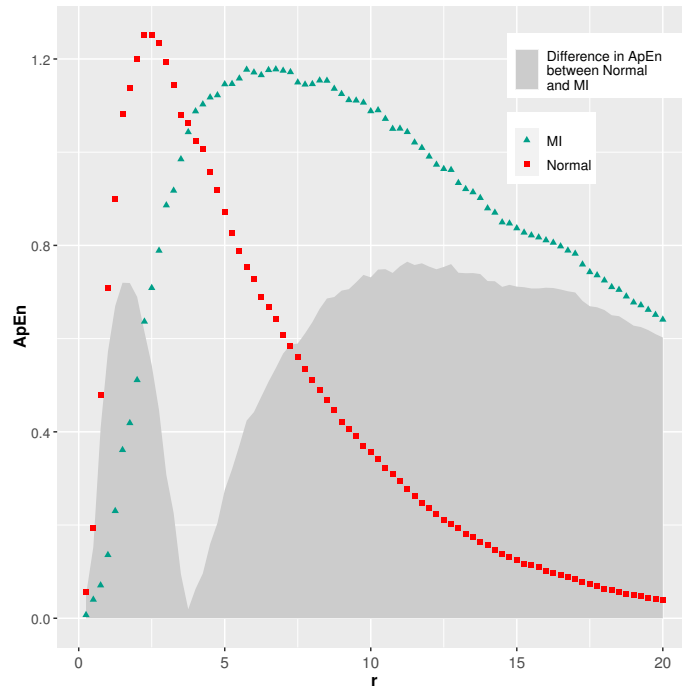


Figure 5.8: Simulated data which represents a phase image for normal left ventricular contraction (in red) and a large MI (in green), demonstrating how $ApEn$ varies with increasing tolerance r , where sequence length $m = 2$. The shaded area represents the difference in $ApEn$ between the normal and MI phase images.

For $SampEn$, if the value of r is too small then $SampEn$ is infinite, as seen in Figures 5.10 and 5.11, and if r is too high it tends towards zero. The normal group has the lowest value of $SampEn$ for both the simulated data and patient data. Unlike $ApEn$, the data is self-consistent, and a normal phase image will always have a lower $SampEn$ than an abnormal phase image. This agrees with published data which states that $SampEn$ is more consistent than $ApEn$ [59]. The important factor in selecting an appropriate r value is avoiding an r that is too low and will produce an infinite value of $SampEn$. From this work, $m = 2$ and $r = 4$ was chosen for $SampEn$.

The optimisation work carried out with both simulated data and patient data provides confidence that the input values selected for $ApEn$ ($m = 2$, $r = 7$) and $SampEn$ ($m = 2$, $r = 4$) are appropriate for the data and their choice can be justified. This work highlights the importance of selecting and optimising input parameters for the data that they will be applied to.

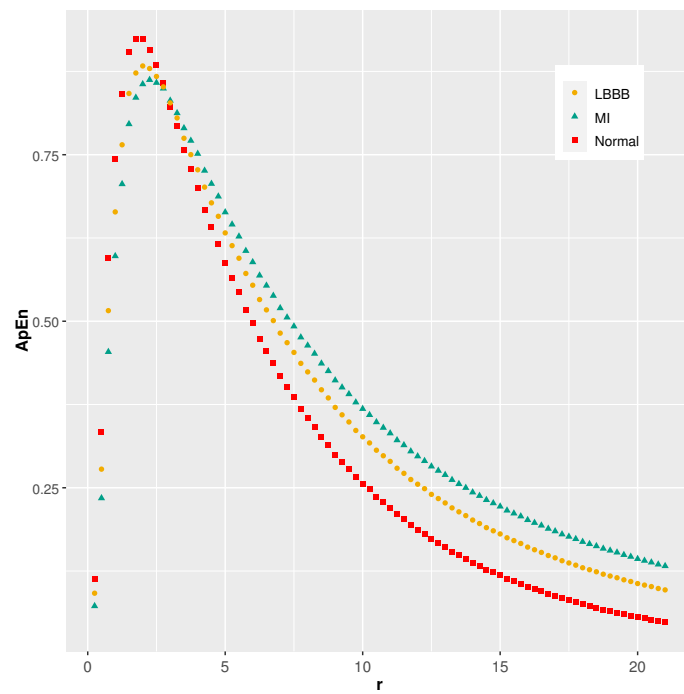


Figure 5.9: Average $ApEn$ for normal (red), MI (green) and LBBB (yellow) patient groups using varying values of tolerance r , where $m = 2$.

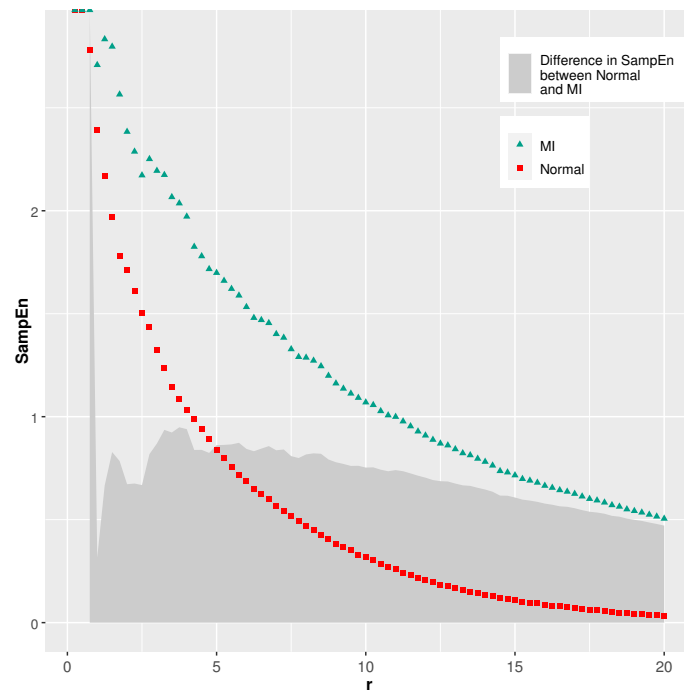


Figure 5.10: Simulated data which represents a phase image for normal left ventricular contraction (in red) and a large MI (in green), demonstrating how $SampEn$ varies with increasing tolerance r , where sequence length $m = 2$. The shaded area represents the difference in $SampEn$

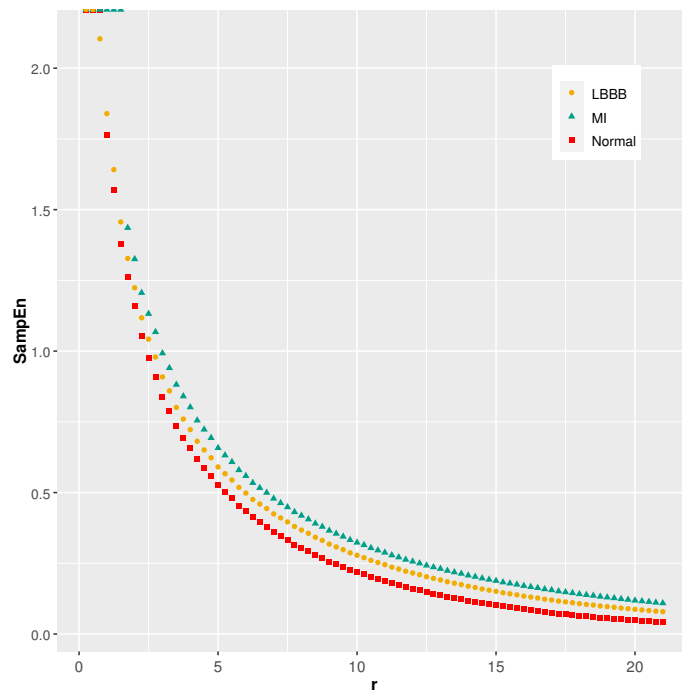


Figure 5.11: Average $SampEn$ for normal (red), MI (green) and LBBB (yellow) patient groups using varying values of tolerance r , where $m=2$.

5.4 Effect of Data Length

Left and right ventricular volumes vary from patient to patient, and subsequently, the number of pixels in the region of interest for each ventricle also varies. Therefore, it is important that $ApEn$ and $SampEn$ are consistent across the range of ventricular volumes.

Simulated data were used to investigate the relation of $ApEn$ and $SampEn$ with the size of the left ventricle. Simulated data were created with a radius varying from 7 to 15 pixels, covering the clinically significant range. $ApEn$ and $SampEn$ were calculated for each left ventricle size to ensure that any difference between patients would be independent of ventricle size.

The results demonstrate that $ApEn$ does not vary significantly as the number of pixels is increased when $r = 7$, as seen in Figure 5.12. However, for $ApEn[r = 1]$ the value of $ApEn$ increases when the left ventricle increases in size, meaning that $ApEn[r = 1]$ is not an appropriate selection for this data. A possible explanation for this might be that when the chosen value of r is low, the bias effect due to the self-matches has a more significant impact. Unlike time-series data like an ECG or gait, it is impossible to control the length of the data series for RNVG phase data. The data length will depend on the size of the left ventricle, which will be patient dependent, so $ApEn$ should be consistent across the clinical range. For this reason, a final value of $r = 7$ was selected for $ApEn$. As the number of pixels in the phase image increases, $SampEn$ remains constant using an $r = 4$ as seen in Figure 5.13. This plot confirms that calculating $SampEn$ using $m = 2$ and $r = 4$ does not depend on data length for the range tested.

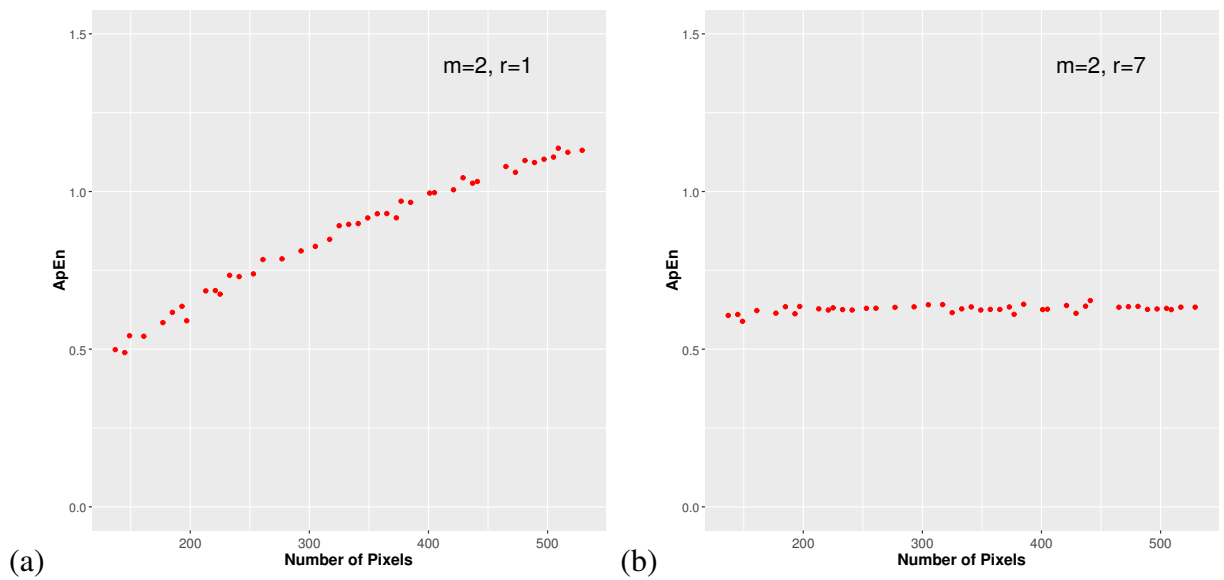


Figure 5.12: Variation of $ApEn$ with left ventricle size for (a) $m = 2, r = 1$ (b) $m = 2, r = 7$, demonstrating a lack of consistency for $r = 1$ with increasing ventricle size for simulated data.

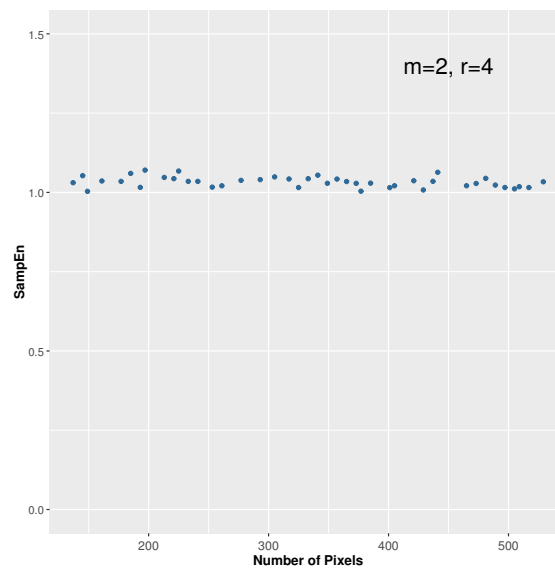


Figure 5.13: Variation of $SampEn$ with left ventricle size for $m = 2, r = 4$, showing consistent $SampEn$ values with increasing ventricle size for simulated data.

The results demonstrate consistency over the clinical range of left ventricle sizes for $ApEn[m = 2, r = 7]$ and $SampEn[m = 2, r = 4]$. Using a lower value of r for $ApEn$ could result in a dependency on sequence length.

5.5 Data Order

First-order measures such as synchrony and entropy have no dependence on data order. However, for *ApEn* and *SampEn*, the order is important. The algorithm reads the phase image and converts it into a matrix, with each pixel representing a phase value. The matrix is then converted into a one-dimensional data series for the calculation. The direction that the matrix is read in will change the order of the pixel values used in the *ApEn* calculation. This section aims to demonstrate the effect of reading the image data in different orders.

ApEn and *SampEn* are usually applied to time series data where the order is set. To investigate the effect of reading the image matrix in different directions, the code was modified to read the data in different orders to allow comparison. The m and r values used for testing the data order were selected based on the optimisation work.

The diagram in Figure 5.14 illustrates the four different directions that the image data were read. In Figure 5.14 (a), the data is read from left to right, and in (b), it is read top to bottom, but this means that in a group of m pixels, they may not be adjacent to each other in the image even though they are adjacent in the data series. For order (a), one pixel could be from the lateral wall of the left ventricle, and the next pixel would be from the septum at the start of the next line. This is unlikely to make a difference in a normal phase image where all the pixels have a similar value but could have an impact when investigating a patient with a more abnormal phase image. The directions shown in Figure 5.14 (c) and (d) will result in groups of ' m ' pixels being adjacent to each other, unlike orders (a) and (b). The group tested consisted of 187 normal and 164 MI patients. Receiver operator characteristic (ROC) analysis was used to determine if the data order affected the ability to discriminate between normal and MI patients. The mean \pm standard deviation, area under the curve (AUC) for separating normal phase from an MI, with 95% confidence intervals (CI) were calculated for each data order.

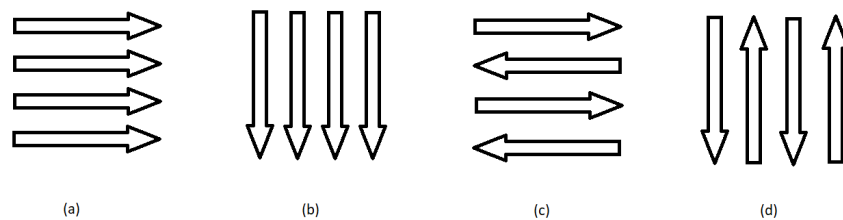


Figure 5.14: The four directions tested for reading the image matrix, reading image from (a) left to right, (b) top to bottom, (c) left - right, right - left etc (d) top - bottom, bottom to top etc.

Tables 5.1 and 5.2 summarise the statistics for *ApEn* and *SampEn* for phase data read in different directions. As expected, there is a small difference in *ApEn* and *SampEn* for different data orders. However, the results indicate that the data order does not affect the ability of *ApEn* or *SampEn* to discriminate between normal and abnormal phase. The ROC curves for each data

Table 5.1: Summary of statistics for $ApEn$ with data order


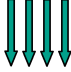


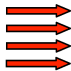
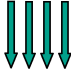
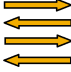

Data Order	Normal Group <i>Mean ± SD</i>	MI Group <i>Mean ± SD</i>	AUC	95% CI
(a) 	0.460 ± 0.138	0.556 ± 0.116	0.72	0.66-0.77
(b) 	0.457 ± 0.129	0.566 ± 0.119	0.75	0.67-0.77
(c) 	0.418 ± 0.135	0.520 ± 0.118	0.73	0.65-0.76
(d) 	0.414 ± 0.133	0.524 ± 0.124	0.74	0.67-0.77

Table 5.2: Summary of statistics for $SampEn$ with data order

Data Order	Normal Group <i>Mean ± SD</i>	MI Group <i>Mean ± SD</i>	AUC	95% CI
(a) 	0.683 ± 0.186	0.816 ± 0.222	0.70	0.64-0.75
(b) 	0.672 ± 0.182	0.822 ± 0.213	0.72	0.67-0.77
(c) 	0.659 ± 0.187	0.802 ± 0.233	0.71	0.65-0.76
(d) 	0.656 ± 0.188	0.811 ± 0.225	0.72	0.67-0.77

order are shown in Figure 5.15 for $ApEn$ and Figure 5.16 for $SampEn$. As seen on these plots, the AUC values for the four variations on data order range from 0.72 to 0.75 for $ApEn$ and 0.70 to 0.72 for $SampEn$. $ApEn$ and $SampEn$ are lower for directions (c) and (d), this is likely because for each group of m the pixels are next to each other, resulting in more matches and lower $ApEn$ and $SampEn$.

The data order did not significantly affect the AUC values. However, intuitively order (c) and (d) are preferred because the pixels in each group of sequence length m are adjacent. Order (c) has been used for the optimisation work for m and r and will be used throughout the rest of this work.

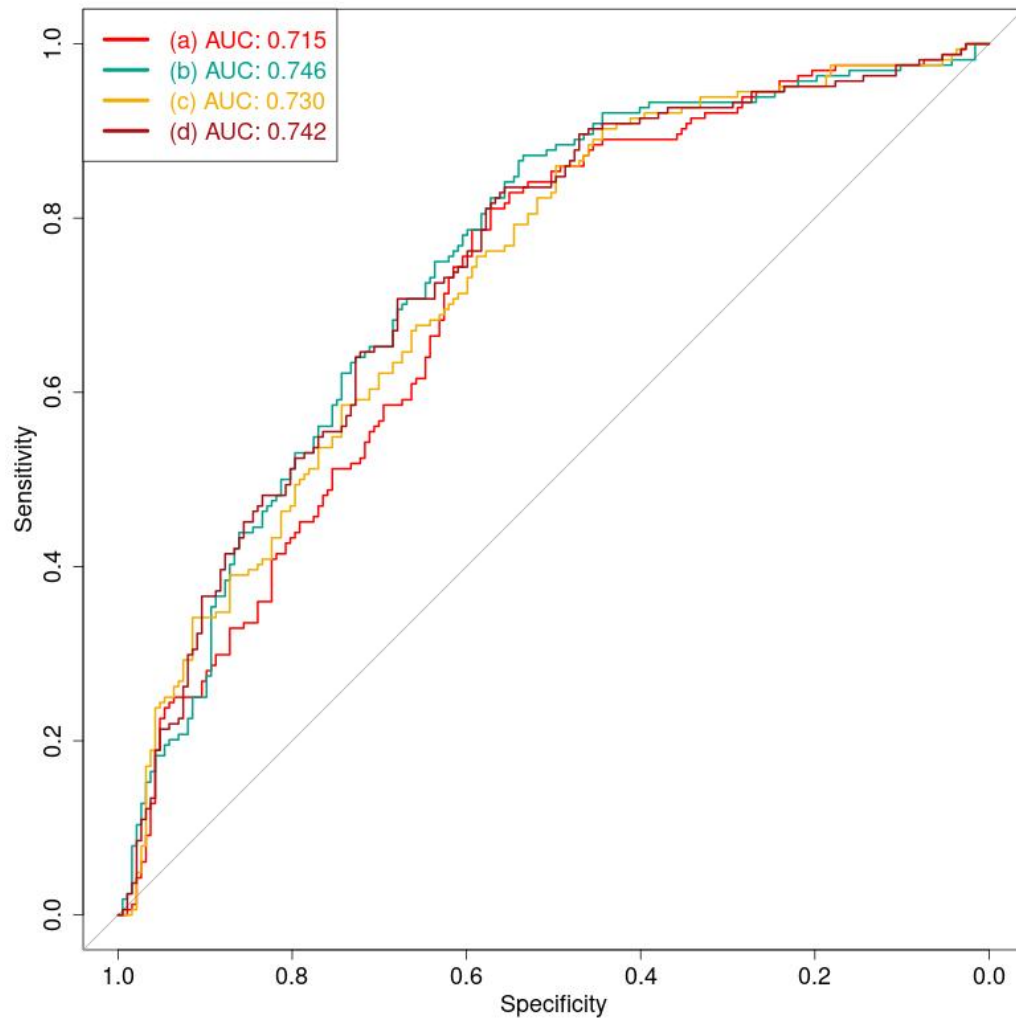


Figure 5.15: ROC analysis of $ApEn$ for each data order, comparing the difference between normal and MI groups.

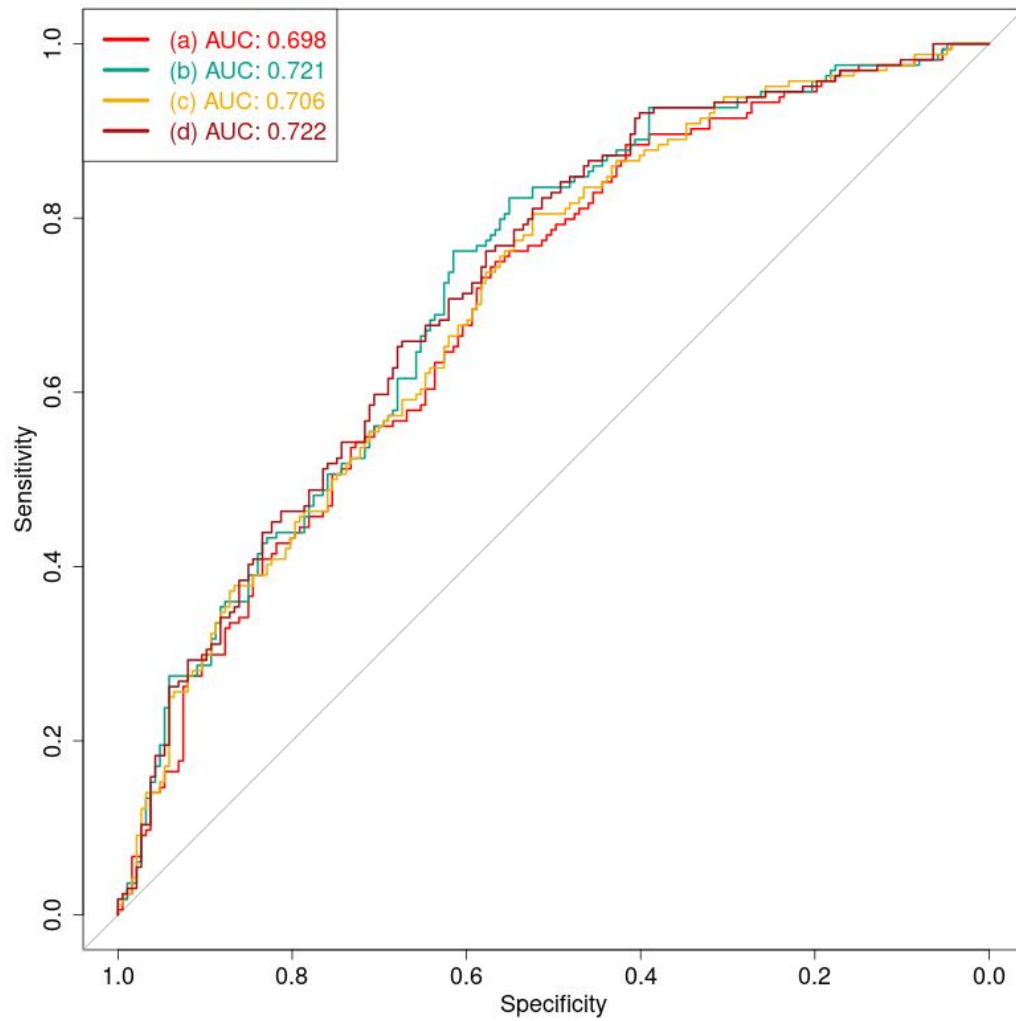


Figure 5.16: ROC analysis of *SampEn* for each data order, comparing the difference between normal and MI groups.

5.6 Conclusions

Appropriate input parameters for *ApEn* and *SampEn* applied to RNVG phase images have been established using both simulated and patient data. The results justify the input parameters selected and demonstrate that they are appropriate for application to RNVG phase images. This work highlights the importance of optimising input parameters when using novel indices, such as *ApEn* and *SampEn*, to characterise clinical images. Standardisation is crucial, and although this work investigates *ApEn* and *SampEn* for the specific application of RNVG phase, it demonstrates the importance of optimisation and standardisation.

Chapter 6

Normal Range and Reproducibility

6.1 Introduction

The work described in this chapter will investigate the normal range, reproducibility, and correlation for dyssynchrony parameters investigated in this thesis. There is currently no standardisation or established normal range for dyssynchrony measured from radionuclide ventriculography (RNVG) phase images. Normal range, reproducibility, and an understanding of the correlation between dyssynchrony parameters will be essential to provide meaningful results and allow comparison between different sites, techniques, and software.

6.2 Normal Range

It is important to establish a normal range for any technique to give the results clinical context. Several studies have investigated the normal range for synchrony, entropy and phase standard deviation calculated from RNVG phase images. The results of these studies are summarised in Table 6.1. The data is limited to small sample sizes from single centre studies and have varying results. For example Singh *et al.* [42] suggest a normal cut-off for phase standard deviation of 13.2 degrees, while Marcassa *et al.* [78] suggest a cut of of 18 degrees (both defined using mean + 2 standard deviations). The variation in 'normal' phase values between the studies in Table 6.1 highlights how dependent a normal range can be on the protocol and software used. Currently, there is no published assessment of the normal range for $ApEn$ and $SampEn$ applied to RNVG phase.

Work was carried out to establish a normal range for each parameter using retrospective data. The patients used to define the normal range were selected based on the following criteria; normal myocardial perfusion, normal LVEF, normal wall motion and no previous cardiac history. However, all of the 'normal' patients were referred to the Department of Nuclear Cardiology with cardiac symptoms. The group consisted of 187 patients (51 male and 136 female). The dyssynchrony parameters were calculated using the optimised m and r values for $ApEn$ and

Table 6.1: Comparison of RNVG dyssynchrony normal range from the literature

	n	Synchrony	Entropy	Phase SD
O'Connell <i>et al.</i> 2005 [45]	22	0.99 ± 0.01	0.37 ± 0.08	12.2 ± 5.4
Johnson <i>et al.</i> 2015 [47]	49	0.97 ± 0.08	0.41 ± 0.12	13 ± 3
Badhwar <i>et al.</i> 2016 [34]	30	0.99 ± 0.01	0.45 ± 0.02	NA
Vallejo <i>et al.</i> 2010 [41]	22	NA	NA	10 ± 2
Singh <i>et al.</i> 2013 [42]	108	NA	NA	8.2 ± 2.5
Marcassa <i>et al.</i> 2007 [78]	56	NA	NA	9.1 ± 4.5

Results are presented as mean \pm standard deviation (SD). n = number of patients included in the study.

SampEn that were established in Chapter 5, and a 1 degree bin width for entropy. Results are presented as mean \pm standard deviation. A normal cut off is suggested for each parameter in Table 6.2 using two standard deviations. Although the 'normal' group used for this work met all of the previously defined criteria, they may have unknown underlying cardiovascular conditions or mildly abnormal phase images. All of the 'normal' patients were referred to Nuclear Cardiology with symptoms of ischaemic heart disease. Therefore, this normal range should be confirmed using healthy normal volunteers. A comparison of patients with normal dyssynchrony, as defined by global longitudinal strain, would also be of interest. However, this is outwith the scope of this work and would require ethics approval.

Each parameter was also used to compare 187 normal patients to the 164 myocardial infarction (MI) patients and 112 left bundle branch block (LBBB) patients. A Shapiro-Wilks test was used for each parameter to assess if the data were normally distributed before selecting the appropriate statistical test for comparison. The results of this comparison are summarised in Table 6.3. The table shows the mean and standard deviation for each parameter and the results of the significance test between the three groups. Plots for each parameter are shown in Figures 6.1-6.5. The boxplots for each dyssynchrony parameter show the median and interquartile range for the normal, MI and LBBB. Synchrony, entropy, phase standard deviation, and *SampEn* were normally distributed, so ANOVA was used to compare all three groups, and a two-sample t-test was used for pairwise comparison. The data for *ApEn* was not a normal distribution, therefore, Kruskal-Wallis was used to compare the groups and Wilcoxon sign-rank test was used for pairwise comparison. When comparing the normal, MI and LBBB patients, all of the dyssynchrony parameters tested showed a significant difference between the three groups and for pairwise comparison. The results demonstrate that both the LBBB and MI groups are more dyssynchronous than the normal group. The biggest difference in dyssynchrony is between the normal and MI group, with the MI group being the most dyssynchronous, which is not surprising. There is some overlap in dyssynchrony values for each of the parameters, but there will be some patients with LBBB or history of an MI who do not have any dyssynchrony. The LBBB group all have electrical dyssynchrony, but not all will have associated mechanical dyssynchrony. Some patients in the normal group may also have some mild dyssynchrony, so

some overlap is expected between the groups. There is one outlier on the synchrony plot for the MI group. Further investigation revealed that this point represents a patient with a large aneurysm with two regions within the left ventricle contracting at opposite times, resulting in a synchrony value close to zero.

Table 6.2: Normal Range (n=187)

	Mean \pm SD	Normal cut-off
Synchrony	0.99 \pm 0.01	> 0.97
Entropy	0.56 \pm 0.04	< 0.64
ApEn	0.42 \pm 0.14	< 0.70
SampEn	0.66 \pm 0.19	< 0.84
Phase SD	7.9 \pm 2.0	< 9.9

SD = standard deviation. The normal cut-off for each parameter is defined from the mean + 2 SD of 187 patients.

Table 6.3: Results comparing normal, MI and LBBB groups.

	Normal	MI	LBBB	P-value
Synchrony	0.99 \pm 0.01	0.96 \pm 0.08	0.98 \pm 0.03	p < 0.001
Entropy	0.56 \pm 0.04	0.64 \pm 0.06	0.61 \pm 0.06	p < 0.001
ApEn	0.42 \pm 0.14	0.52 \pm 0.12	0.48 \pm 0.12	p < 0.001
SampEn	0.66 \pm 0.19	0.81 \pm 0.23	0.72 \pm 0.19	p < 0.001
Phase SD	7.9 \pm 2.0	16.1 \pm 11.6	11.7 \pm 7.6	p < 0.001

Results are presented as mean \pm standard deviation for each group. Significance was tested using ANOVA or Kruskal-Wallis test depending on the normality of the data.

The mean normal values are compared with the studies in Table 6.1. There is only published normal data available for synchrony, entropy and phase standard deviation. There is some variation between the studies, which could be attributed to different processing software. Most of the studies use software that was written in-house rather than a commercially available product. The phase pixel values may not be interchangeable between different software, as they depend on various factors including histograms bins, temporal and smoothing filters, and noise. Smoothing filters and bin size have not been investigated in this work. Only clinically used filters and matrix size were used. In a comparison of normal and LBBB patients, Wassenaar *et al.* [79] concluded that the bin size and the histogram threshold value did not impact AUC (area under the receiver-operator curve). Wassenaar *et al.* also demonstrated that the smoothing did not impact the ability of synchrony and entropy to detect abnormal phase; however, the AUC did improve with decreased smoothing. Phase standard deviation was demonstrated to have a stronger dependence on the image smoothing than synchrony or entropy. Therefore, the normal range will apply only to the Link Medical Maps software with the image parameters used in clinical practice that were used in this research. The criteria for defining a 'normal' patient also varies between the studies.

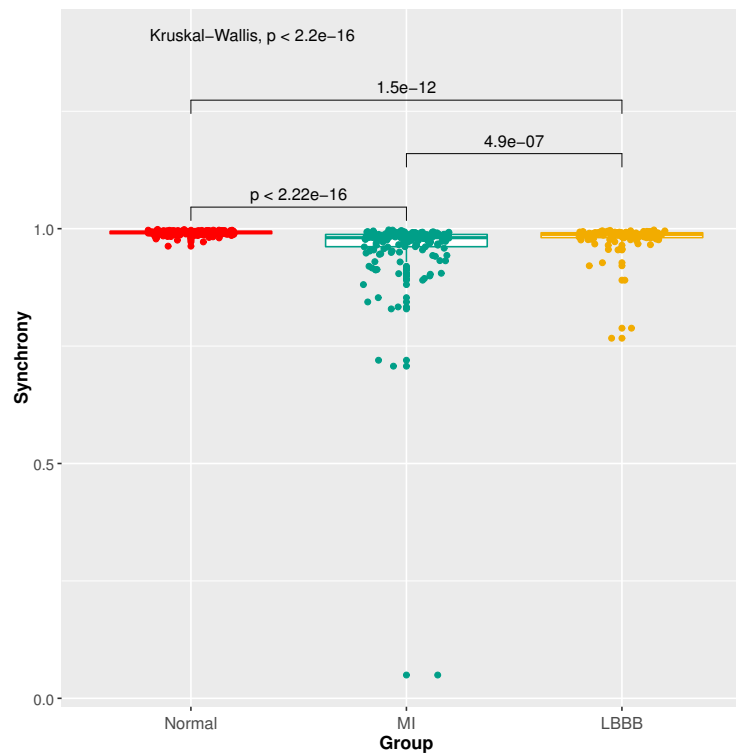


Figure 6.1: Comparison of synchrony for normal, MI and LBBB groups. Kruskal-Wallis was used to compare all three groups and Wilcoxon rank-sum test was used for pairwise comparison.

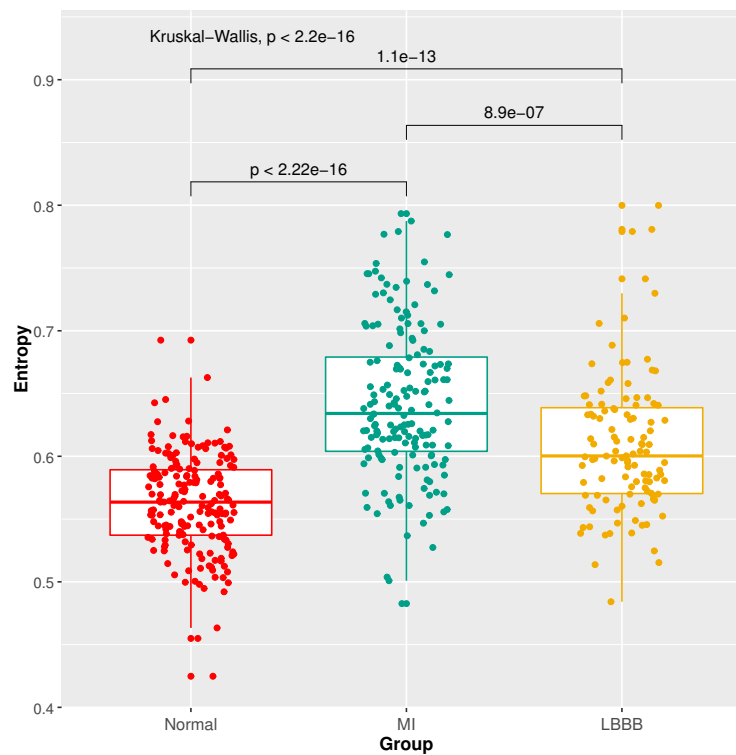


Figure 6.2: Comparison of entropy for normal, MI and LBBB groups. Kruskal-Wallis was used to compare all three groups and Wilcoxon rank-sum test was used for pairwise comparison.

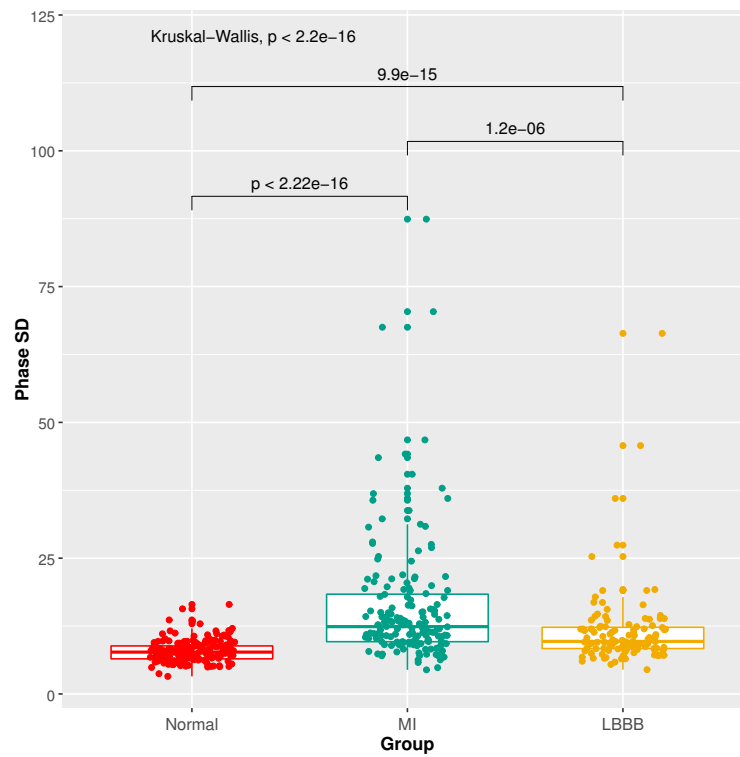


Figure 6.3: Comparison of phase standard deviation for normal, MI and LBBB groups. Kruskal-Wallis was used to compare all three groups and Wilcoxon rank-sum test was used for pairwise comparison.

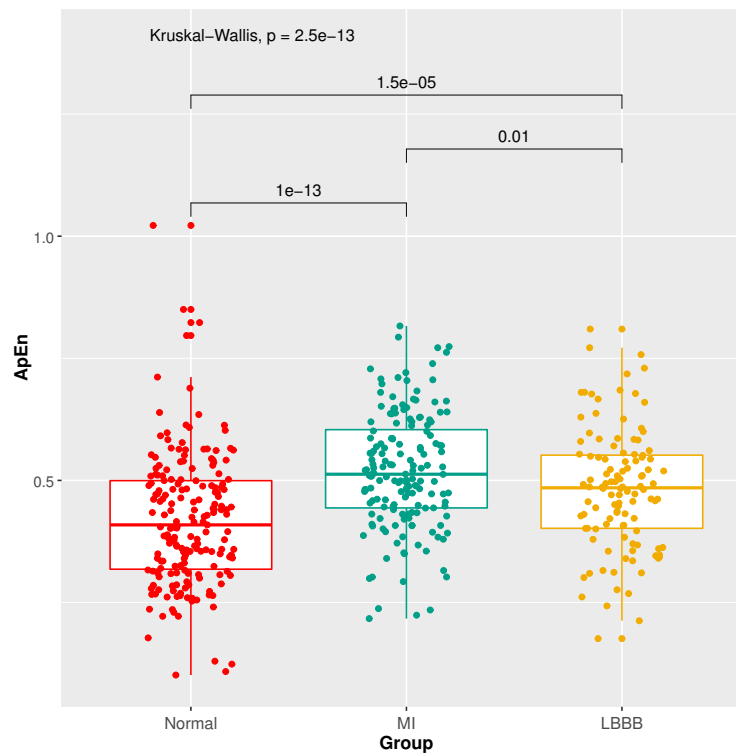


Figure 6.4: Comparing $ApEn$ for normal, MI and LBBB groups. Kruskal-Wallis was used to compare all three groups and Wilcoxon rank-sum test was used for pairwise comparison.

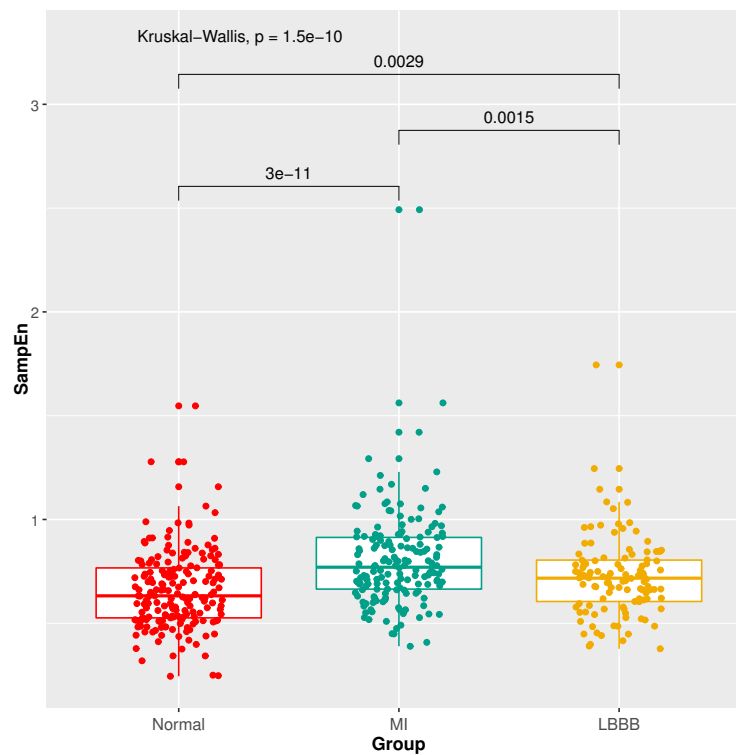


Figure 6.5: Comparison of $SampEn$ for normal, MI and LBBB groups. Kruskal-Wallis was used to compare all three groups and Wilcoxon rank-sum test was used for pairwise comparison.

6.3 Reproducibility

Ideally, all imaging parameters that are used clinically should have high reproducibility. It is important to be aware of all of the limitations of a technique, including the reproducibility of the measurement, particularly if the measurement is being used to guide clinical decisions. This section will assess the intra-operator variability for phase standard deviation, synchrony, entropy, *ApEn*, and *SampEn*.

For each RNVG, two ROIs were compared, both drawn by a single trained operator to assess intra-operator variability. For the second attempt, the operator could not see their first attempt. For each ROI, synchrony, entropy, phase standard deviation, approximate entropy (*ApEn*) and sample entropy (*SampEn*) were calculated from the phase image. The group investigated consisted of 463 patients, including a mixture of normal and abnormal phase. The results for intra-operator variability are summarised in Table 6.4. The correlation and Bland-Altman plots for each parameter are shown in Figures 6.6-6.10. The Bland-Altman plots show the difference between the two paired dyssynchrony measurements plotted against the average of the two measurements. The plots for synchrony (Figure 6.6) show that it has the highest correlation of all of the parameters, but the synchrony values are all tightly clustered around 0.99. The other parameters have a larger range of dyssynchrony values and also demonstrate a high correlation. There does not appear to be any change in the difference as the dyssynchrony value changes for any of the parameters. Overall, the results demonstrate a high correlation for all parameters tested with no evidence of bias, suggesting there is good intra-operator reproducibility for assessing dyssynchrony with RNVG phase parameters.

Further work to investigate the inter-operator variability should also be carried out, but good intra and inter-operator variability have been previously demonstrated for synchrony, entropy, and phase standard deviation [41, 45, 78, 79]. Inter-operator variability is often only assessed for image processing. However, to fully assess the inter-operator reproducibility, each patient should be positioned and scanned by the technologist, then removed from the camera before being set up and the scan repeated by a second independent operator.

The intra-operator reproducibility measured for the dyssynchrony parameters was higher than some studies report [78]. This may be due to the fact that this study was carried out in a specialised nuclear cardiology department, where the clinical technologists have received extensive training and feedback on processing RNVGs.

Table 6.4: Correlation values for intra-operator variability

	Correlation
LV Synchrony	0.999
LV Entropy	0.995
LV ApEn	0.986
LV SampEn	0.994
LV Phase SD	0.998

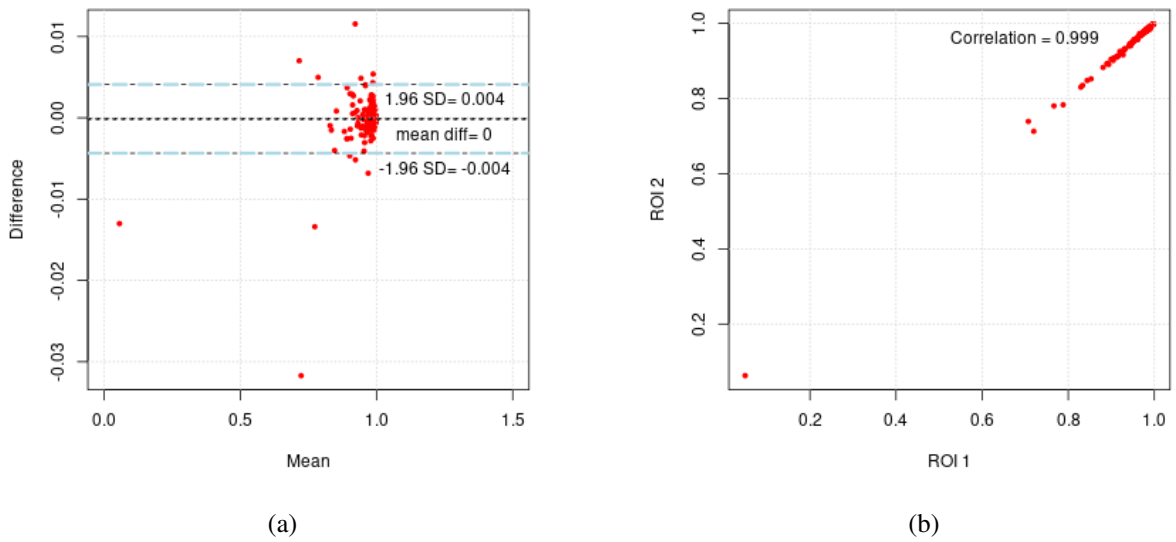


Figure 6.6: Comparing intra-operator variability of synchrony. ROI 1 vs ROI 2 in Bland Altman plot (a) and correlation (b).

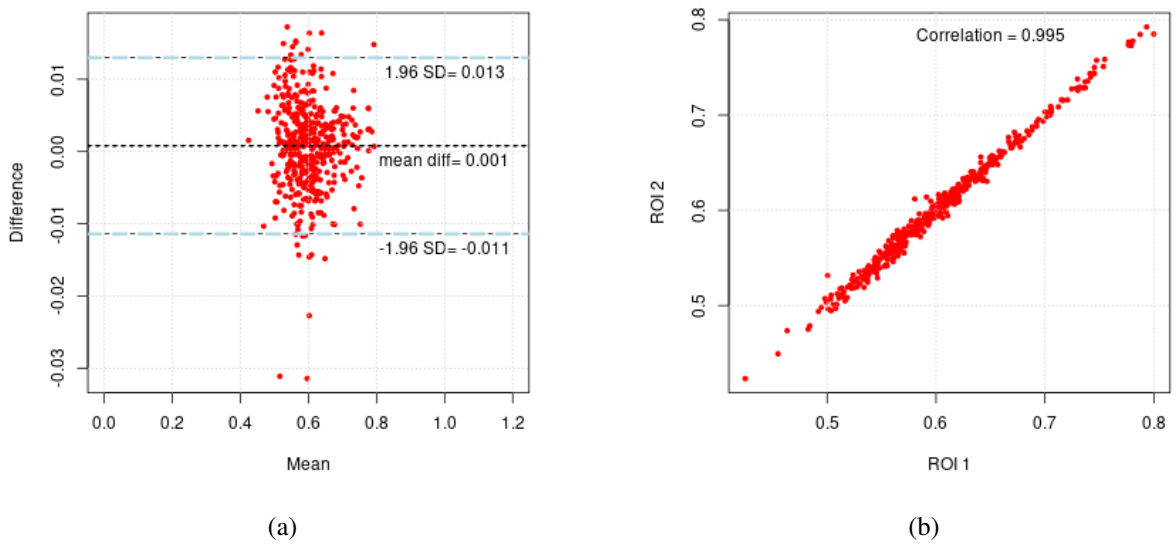
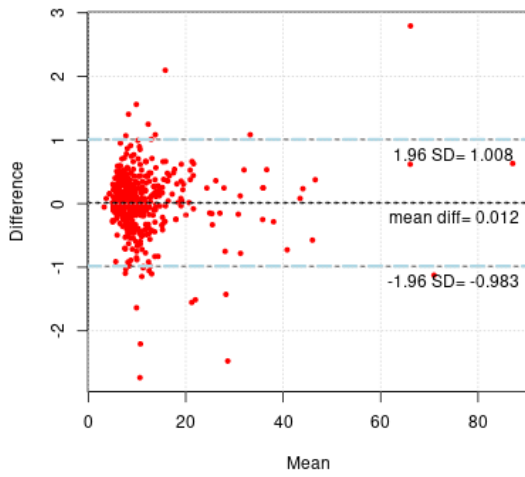
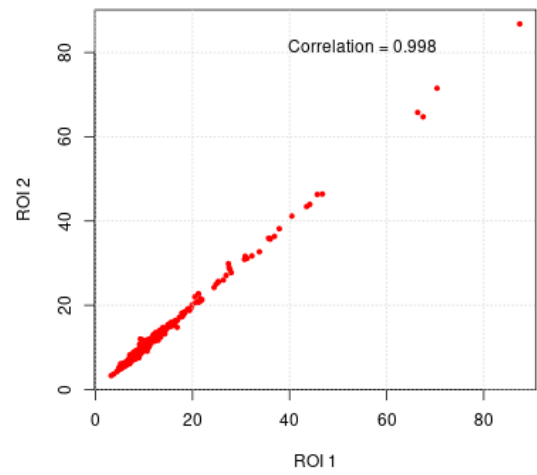


Figure 6.7: Comparing intra-operator variability of entropy. ROI 1 vs ROI 2 in Bland Altman plot (a) and correlation (b).

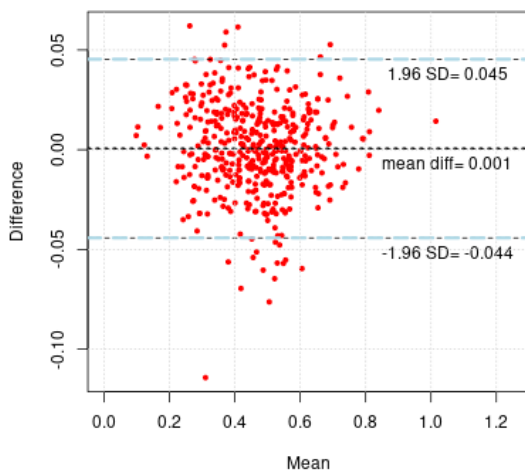


(a)

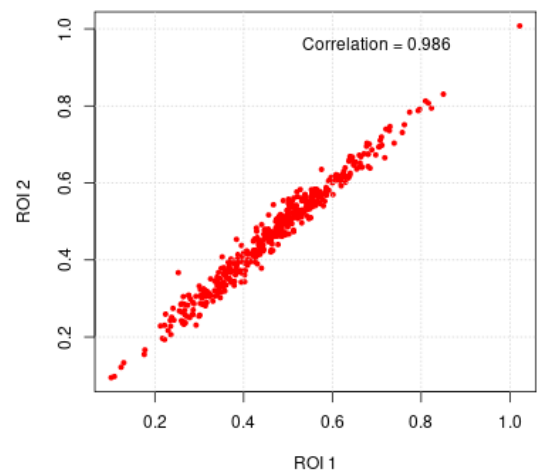


(b)

Figure 6.8: Comparing intra-operator variability of phase standard deviation. ROI 1 vs ROI 2 in Bland Alman plot (a) and correlation (b).



(a)



(b)

Figure 6.9: Comparing intra-operator variability of ApEn. ROI 1 vs ROI 2 in Bland Alman plot (left) and correlation (right).

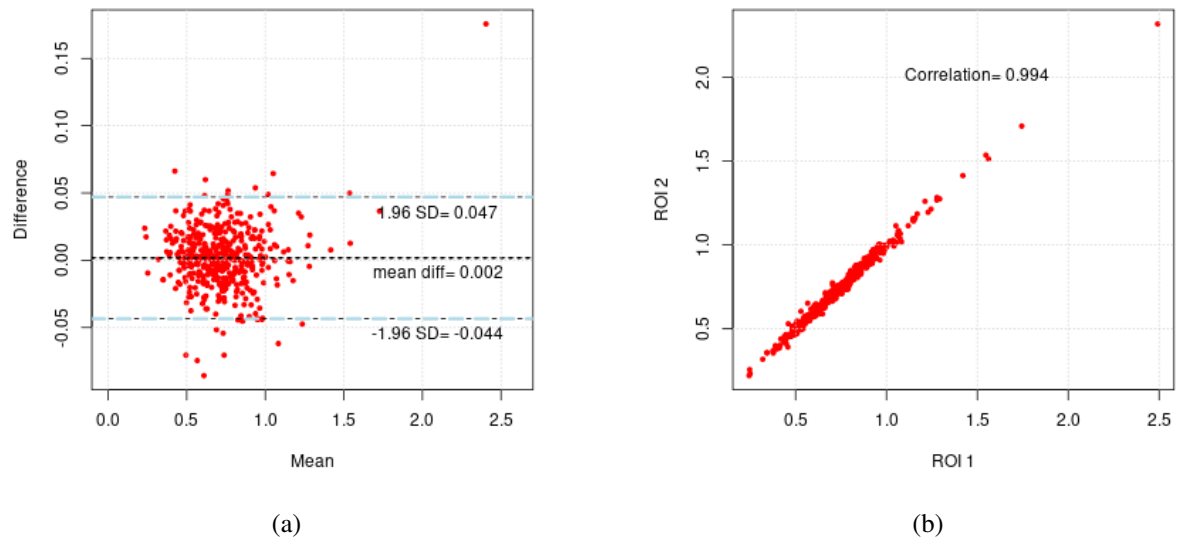


Figure 6.10: Comparing intra-operator variability of *SampEn*. ROI 1 vs ROI 2 in Bland Altman plot (a) and correlation (b).

6.4 Correlation Between Dyssynchrony Parameters

This section aims to determine if there is any correlation between the phase parameters that are under investigation. If there is a high correlation, then there may be no benefit in using multiple measures of dyssynchrony, and a single measure may be sufficient.

Clinical phase images were separated into normal and MI groups. The correlation was tested between all pairs of dyssynchrony measures for both normal and MI groups, and the results were plotted in a pairs correlation matrix using R.

The results demonstrate a high correlation between the dyssynchrony measures for normal phase patients (Figure 6.11). In this matrix of plots, the labels along the top and right edges show the dyssynchrony parameters that are being considered for each plot, while the x and y-axis labels are shown on the left and bottom of the matrix. The diagonal boxes display the distribution for each individual variable. The scatter plots on the lower triangle show the relationship between each pair of variables, and the Pearson correlation coefficient for each pair of variables is displayed on the upper triangle. The high correlation between dyssynchrony parameters is not unexpected because all of the parameters are measured from the same phase data. However, when the MI group is considered, the correlation is reduced between the parameters as shown in Figure 6.12. This suggests there may be additional clinical benefit using multiple dyssynchrony parameters for the assessment of abnormal phase.

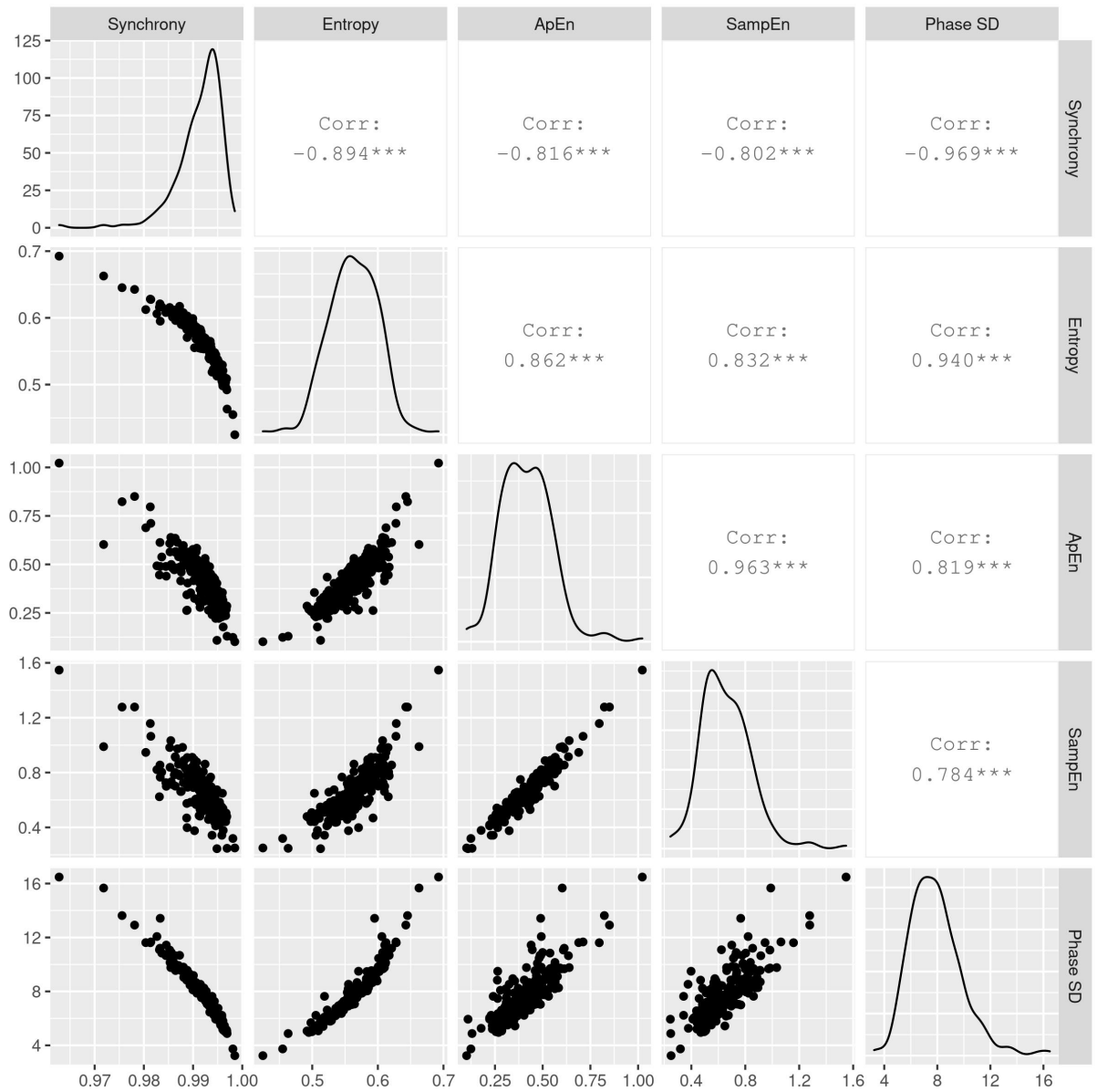


Figure 6.11: Scatter plots for the normal group, showing the correlation for each pair of variables with the associated correlation value, with the variable names displayed along the edges of the matrix. The diagonal boxes display the distribution for each variable. The scatter plots on the lower left area show the relationship between each pair of variables, and the Pearson correlation coefficient for each pair of variables is displayed on the upper right area.

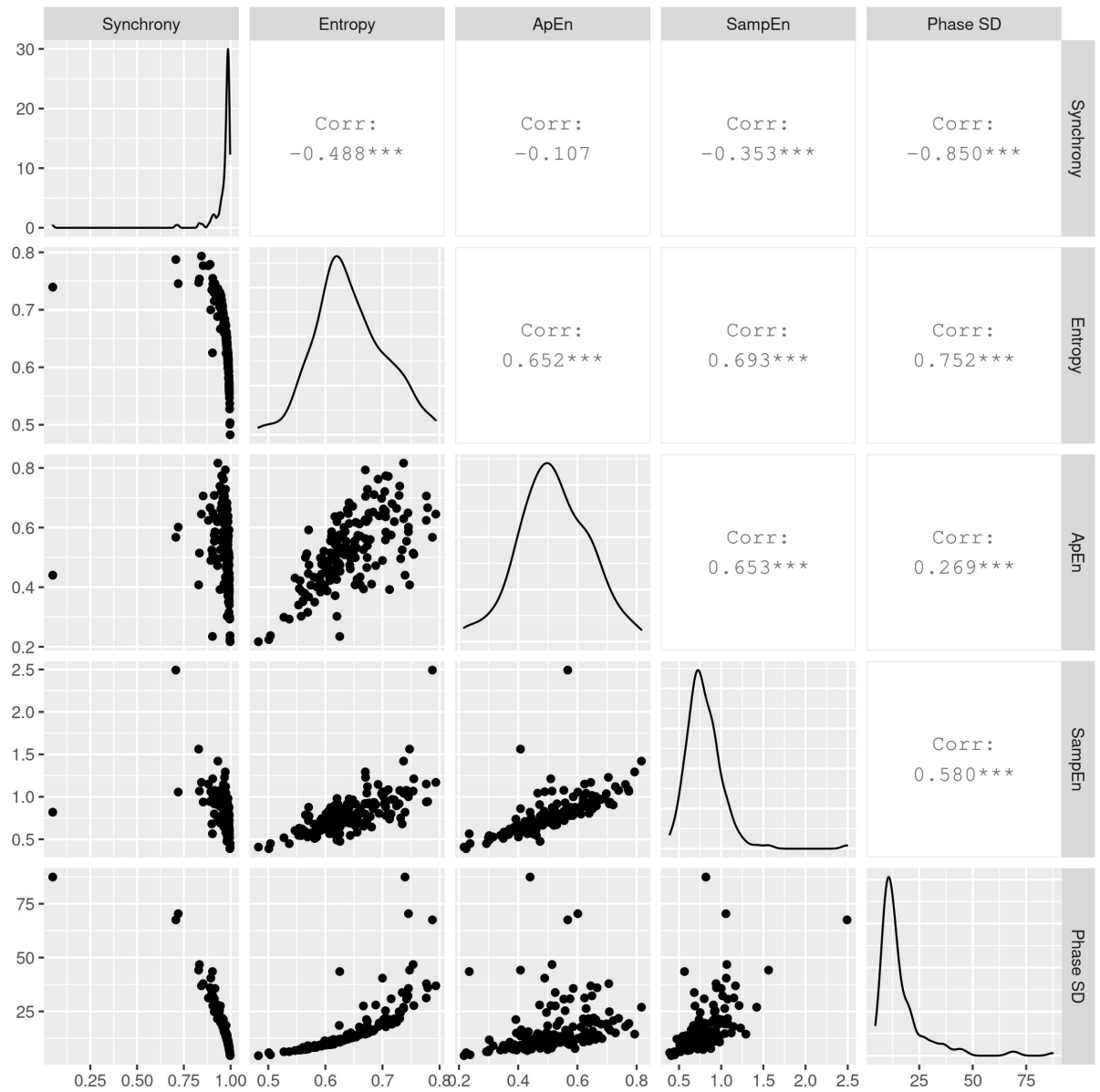


Figure 6.12: Scatter plots for the MI group, showing the correlation for each pair of variables with the associated correlation value, with the variable names displayed along the edges of the matrix. The diagonal boxes display the distribution for each variable. The scatter plots on the lower left area show the relationship between each pair of variables, and the Pearson correlation coefficient for each pair of variables is displayed on the upper right area.

6.5 Conclusions

Reproducibility and normal range have been established with clinical data from the nuclear cardiology department at Glasgow Royal Infirmary for data processed using MAPS Link Medical 10000 software. This work confirms that the dyssynchrony parameters have high intra-operator reproducibility, in agreement with the results of other published work. It is clear that standardisation will be essential for these parameters to become widely used. This is an issue not unique to RNVG; it has also been an issue for new parameters in other imaging techniques, such as global longitudinal strain by echo. It is well established that different software can produce different results with a different normal range for global longitudinal strain [80]. Operator training and experience is one aspect that can significantly impact the reproducibility of each imaging parameter, and it is important for any technique that requires operator input for acquisition or processing. Further investigation would be required to confirm the reproducibility and normal range for clinical use at other sites.

Chapter 7

Risk Stratification for Chemotherapy

Patients

This chapter aims to determine if phase parameters applied to baseline radionuclide ventriculography (RNVG) phase images can measure contraction abnormalities prior to cardiotoxic chemotherapy to predict which patients are at a higher risk of cardiac dysfunction. The work described in this chapter was published in the *Journal of Nuclear Cardiology* and was the first published study investigating RNVG phase parameters as a predictor of cardiac dysfunction following chemotherapy [81].

7.1 Introduction

Survival from breast cancer has improved substantially over the last 30 years due to earlier diagnosis and advances in treatment with adjuvant radiotherapy and chemotherapy. However, cardiotoxicity associated with cancer therapy is now the leading cause of morbidity and mortality for survivors [82, 83]. Anthracycline/trastuzumab-based chemotherapy regimens have been linked with increased risk of cardiovascular disease [84]. Anthracyclines are a class of chemotherapy drugs that come from *Streptomyces* bacterium and can treat many different cancers. Anthracyclines have several modes of action, including increasing DNA breaks and preventing DNA and RNA synthesis. Trastuzumab, also commonly known by the brand name Herceptin, is a targeted cancer drug used to treat HER2 receptor-positive cancers. Trastuzumab attaches to HER2, a protein that causes cancer cells to grow and divide, to control the growth and help the immune system attack and destroy the cancer cells. Trastuzumab is commonly used to treat some types of breast cancer, oesophageal cancer, and stomach cancer. Anthracycline and trastuzumab are highly effective therapies against many types of cancer, but anthracycline-based regimens are associated with the dose-dependent risk of cardiotoxicity and heart failure, whilst trastuzumab is not generally associated with reversible cardiotoxicity. However, non-reversible cardiac dysfunction can occur with both trastuzumab and anthracycline, despite inter-

vention [85]. There is a significantly increased risk of cancer therapy-related cardiac dysfunction (CTRCD) when trastuzumab is combined with anthracyclines [86].

Cardiac monitoring is recommended for patients receiving anthracycline/trastuzumab-based treatments, which currently relies on the serial assessment of left ventricular ejection fraction (LVEF). Each patient will have a baseline LVEF measurement using echo or RNVG, then serial LVEF assessment every three months during treatment. The European Society of Cardiology guidelines (ESC) considers a 10% point decrease of left ventricular ejection fraction (LVEF) to below the lower limit of normal (<50%) to be an indicator of cardiotoxicity and recommend altering or stopping treatment to prevent further left ventricular dysfunction or the development of symptomatic heart failure [29].

One potential limitation of the current guidelines is that LVEF decline is often a late phenomenon. Therefore, it would be useful to identify sub-clinical cardiac abnormalities and identify patients at higher risk before treatment starts. In addition to LVEF assessment, there is growing interest within the field in using early markers of myocardial changes, including speckle tracking longitudinal strain from echocardiography, as previously described in Chapter 2, to assess myocardial deformation. Published data suggest that longitudinal strain may be able to detect myocardial changes earlier than LVEF [26], but this has not previously been investigated using RNVG dyssynchrony parameters.

7.2 Methods

7.2.1 Data Acquisition

A retrospective study was undertaken to review 193 consecutive female breast cancer patients (mean age: 54) who had RNVG scans at Glasgow Western Infirmary Hospital between 2005 and 2008. All patients included in this study had a baseline RNVG before receiving cardiotoxic cancer therapy and follow up scans. The RNVG scans were acquired at intervals of approximately 3 months for up to 2 years following the baseline study, with each patient having between 2 and 9 RNVGs. Based on the current guidelines, patients with a baseline LVEF of <55% would not start treatment; therefore, these patients were excluded from the study.

In-vivo labelling was performed using an intravenous administration of pyrophosphate 20 minutes prior to injection of 800 MBq (21.6mCi) of Technetium-99m pertechnetate. Each study was acquired using a Picker 3000XP 3-headed gamma camera (Picker International, Cleveland Heights, Ohio, USA) with a low energy high-resolution collimator. The gamma camera was carefully positioned to achieve the best septal separation, and the scan was acquired for 5 million counts using frame mode acquisition, a matrix size of 64x64, and 24-frame gating. The LVEF was assessed by an experienced operator using Picker Lightbox software with a manual dual region technique to measure the ejection fraction.

Only the raw images were available for this study. Therefore the baseline RNVG for all 193 patients was reprocessed using MAPS Link medical software to create the phase and amplitude images from the first-order Fourier harmonic, as described in Chapter 2. A single left ventricle region was manually outlined for each baseline study, using the end-diastolic image with reference to the phase and amplitude images. 16 patients were excluded at this stage (11 patients with gating problems were picked up from the phase image and time-activity curve, 4 patients with a baseline LVEF below 55% and 1 patient with a baseline scan below diagnostic quality due to poor radiopharmaceutical labelling), leaving 177 patients. The gating issues were due to the fact that prospective cardiac gating was used rather than retrospective. The gating bins and beat acceptance window are determined before the scan and cannot be adjusted afterwards in prospective gating. This is a problem if the patient's heart rate changes during the acquisition.

7.2.2 Data Analysis

The LVEF from all follow up RNVG studies were compared to the baseline to establish the maximum LVEF drop for each patient. The reported LVEF from the initial analysis was used along with the phase images created using MAPS Link Medical software. Based on the ESC guidelines, patients were split by LVEF decline into 2 groups. In-house software written in R 3.6.3 (R Development Core Team, Vienna, Austria) [62, 75] was used to calculate synchrony, entropy, phase standard deviation, approximate entropy ($ApEn$), and sample entropy ($SampEn$) for the baseline scans, using input parameters $m = 2$ and $r = 7$, as described in Chapters 3 and 5.

7.2.3 Statistical Analysis

Shapiro-Wilk's test was used to check the normality of the distribution for each parameter, and the Henze-Zirkler test was used to test multivariate normality. Significance testing was performed for each parameter, using the unpaired t-test or Wilcoxon rank-sum test, depending on the outcome of the univariate test of normality. In addition, Hotelling's T^2 test was used to determine if there was a significant difference between multivariate means of the different populations [66]. A logistic regression model, as described in Chapter 4, was fitted in R using the interaction between one of the significant dyssynchrony parameters and baseline LVEF [62, 65]. The area under the receiver operator curve (AUC) and accuracy were reported for the model. A p-value of < 0.05 was considered significant for all tests. The correlation between the parameters was also tested.

7.3 Results

Patients were split into two groups based on the change in LVEF during treatment. Group 1 maintained a normal LVEF ($> 50\%$) during treatment, and Group 2 had a decline in LVEF of

more than 10% to below 50%. The guidelines would recommend that the treatment for Group 2 is altered or stopped. Figure 7.1 displays the scatter plots showing the correlation for each pair of variables on the lower left area with the associated Pearson correlation value on the upper right area of the figure. The variable names are displayed along the edges of the matrix. The diagonal boxes show the distribution for each individual variable. This figure shows that dyssynchrony predictors had high a correlation with each other. This compares well with the correlation plots for normal patients in Chapter 6. *ApEn* and *SampEn* had the highest correlation of 0.95. The scatter plots and associated Pearson correlation values demonstrate that LVEF does not correlate strongly with any of the dyssynchrony parameters.

ApEn, *SampEn*, phase SD and age were normally distributed while synchrony, entropy and baseline LVEF were not. Multivariate normality testing for *ApEn* combined with baseline LVEF revealed that both groups were normally distributed. A Chi-squared test was used for categorical data, and a two-sample t-test or Wilcoxon rank-sum test was used depending on the normality of the specific variable for the significance tests. Boxplots comparing the results for each dyssynchrony parameter can be seen in Figures 7.2 - 7.6. The boxplots for each dyssynchrony parameter show the median and interquartile range for the patients who maintained a normal ejection fraction and those who had a significant decline in ejection fraction during or after treatment. These plots demonstrate that the left ventricle is more dyssynchronous at baseline for the group with decreased LVEF during or after treatment.

However, *ApEn*, *SampEn* were the only measures of dyssynchrony that were significantly different between the two groups. The dyssynchrony values measured for both group 1 and group 2 are all within the normal cut-off defined in Chapter 6. There was also a significant difference in LVEF at baseline as shown in Figure 7.7. Patients with a lower (but still normal LVEF) at baseline were more likely to go on to develop cardiac dysfunction, as measured by LVEF decline. The results for all predictors are summarised in Table 7.1. This table shows the mean and standard deviation for each dyssynchrony parameter, along with the significance test used and the p-value. Age and number of patients for each group are also reported. There was no significant difference ($p > 0.05$) in age, synchrony, entropy, or phase standard deviation between the two groups. However, there was a significant difference ($p < 0.05$) in *ApEn*, *SampEn*, and baseline LVEF. The combination of *ApEn* and baseline LVEF was also significantly different between the two groups.

Figure 7.8 demonstrates that combining the baseline LVEF with the baseline *ApEn* can improve the separation between the groups. This figure shows the baseline LVEF plotted against baseline *ApEn* for both groups, with the dashed lines representing the mean *ApEn* and mean LVEF of the test population. The majority of patients who experienced a significant decline in LVEF are in the lower right quadrant of this graph, indicating that patients with a lower LVEF and higher *ApEn* at their baseline RNVG are more likely to have an LVEF drop of more than 10% to below 50%. In contrast, none of the patients in the upper left quadrant on this graph

(higher LVEF and lower $ApEn$) experienced a significant decline in LVEF. Due to the high correlation between $ApEn$ and $SampEn$, only one was used in the logistic regression model. $ApEn$ was selected because it had previously been investigated for the assessment of RNVG phase [36]. A summary of the logistic regression model, created with 10-fold cross-validation and 3 repeats as previously described in Chapter 4, is shown in Table 7.2. The table shows the coefficient and p-value for each predictor and the AUC and accuracy for the model. All of the individual predictors within this model were significant. The fitted logistic regression modelling demonstrated that $ApEn$, baseline LVEF and their interaction were significant predictors for cardiac dysfunction following cancer therapy. The logistic regression model achieved an AUC of 0.88 and an accuracy of 93% using only $ApEn$, baseline LVEF, and the interaction between them.

Table 7.1: Summary of results for each phase parameter for predicting cardiac dysfunction

	Mean (SD)		Significance Test	P -Value
	Group 1	Group 2		
Number of patients	166	11	—	—
Age	55 (11)	56 (15)	Wilcoxon rank-sum	0.799
Synchrony	0.991 (0.004)	0.989 (0.004)	Wilcoxon rank-sum	0.121
Entropy	0.559 (0.040)	0.584 (0.028)	Wilcoxon rank-sum	0.054
$ApEn$	0.348 (0.107)	0.418 (0.076)	Two sample t-test	0.014
$SampEn$	0.291 (0.091)	0.342 (0.070)	Two sample t-test	0.039
Phase SD	7.9 (2.0)	8.9 (1.8)	Wilcoxon rank-sum	0.094
Baseline LVEF	73.5 (6.1)	64.5 (6.7)	Two sample t-test	0.001
($ApEn$, baseline LVEF)	—	—	Hotelling's T^2	0.001

Data are presented as mean (\pm SD) for continuous variables and absolute number of the population for categorical data. Group 1 maintained a normal LVEF (> 50%) during treatment, and Group 2 had a decline in LVEF of more than 10% to below 50%. To test significance, a Chi-squared test was used for categorical data and two sample t-test or Wilcoxon rank-sum test was used for continuous data depending on the normality of the specific variable. The p-values for significant variables are in bold.

7.4 Discussion

The results confirm a significant difference in $ApEn$ between the group with LVEF decline of more than 10% to below 50% (Group 2) and the group that maintained a normal LVEF throughout treatment (Group 1). In addition, $ApEn$ performed better than synchrony, entropy and phase SD for predicting cardiac dysfunction in this cohort. $SampEn$ was also significantly different between the groups, but it was highly correlated with $ApEn$. The high correlation is

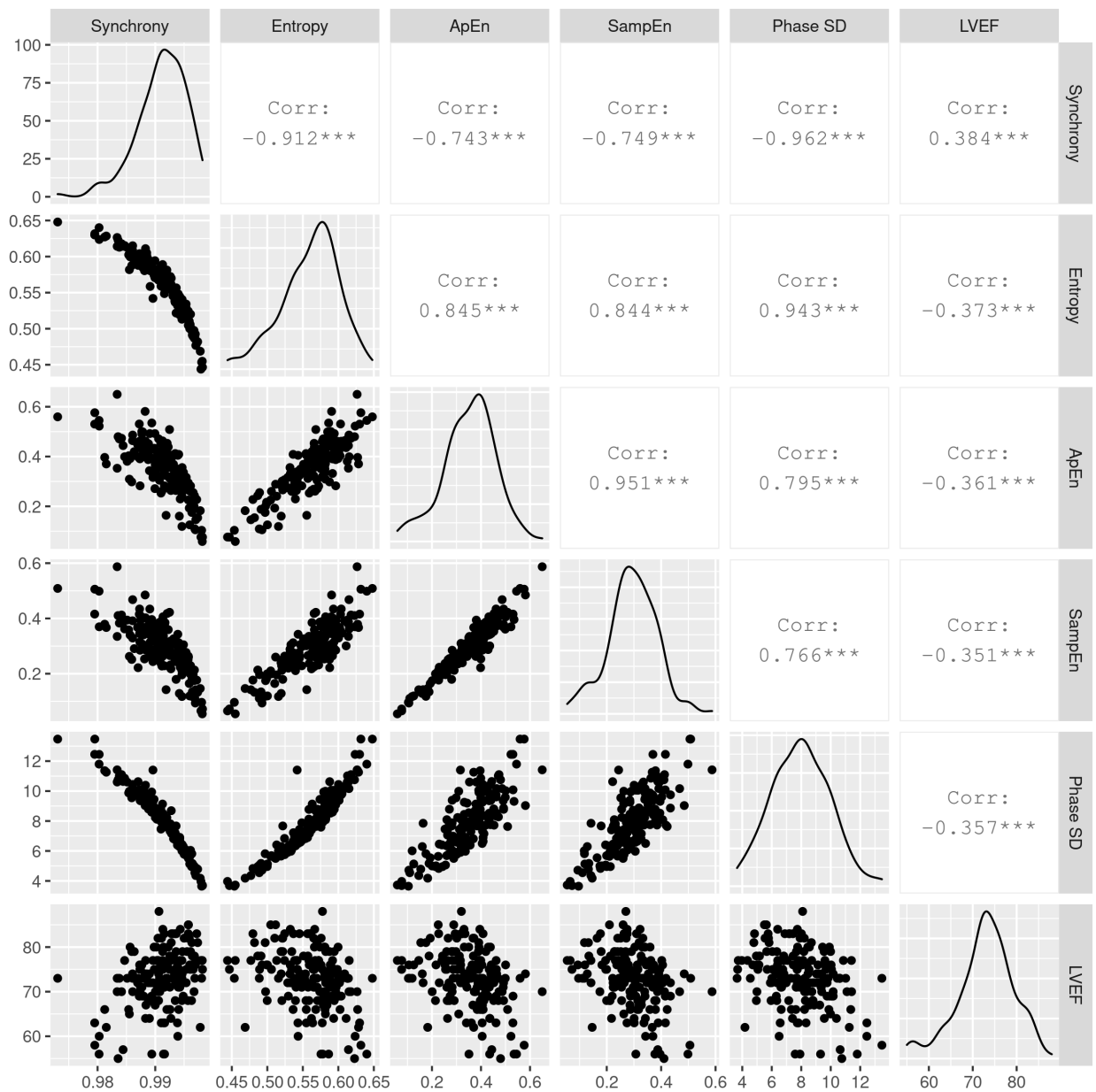


Figure 7.1: Scatter plots showing the correlation for each pair of variables with the associated correlation value, with the variable names displayed along the edges of the matrix. The diagonal boxes display the distribution for each individual variable. The scatter plots in lower left area show the relationship between each pair of variables, and the Pearson correlation coefficient for each pair of variables is displayed in the upper right area.

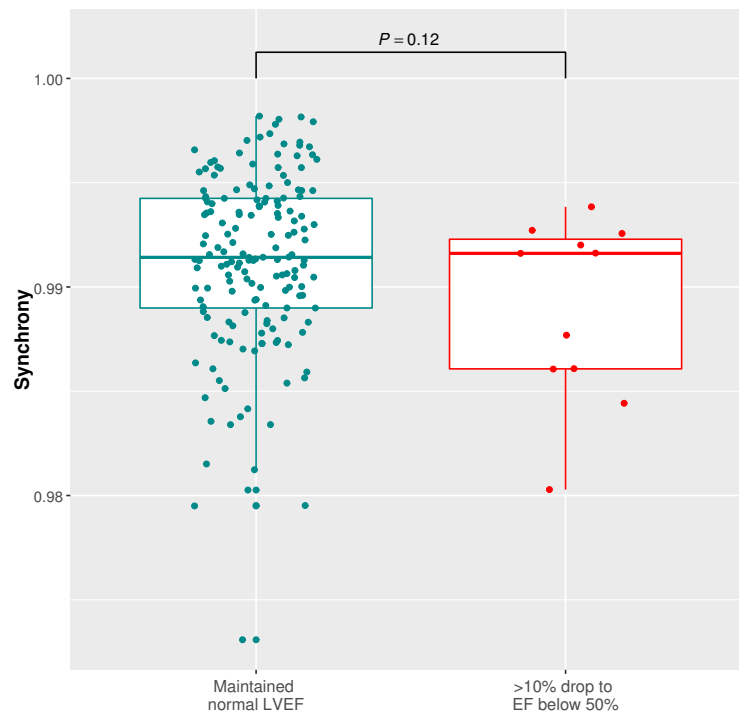


Figure 7.2: Synchrony for patients calculated from baseline RNVG phase image, split into two groups based on LVEF decline.

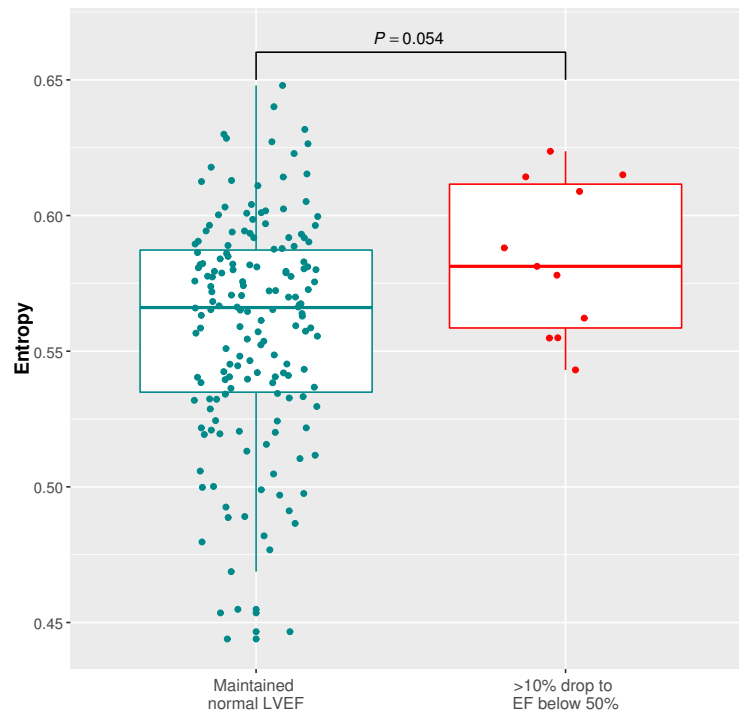


Figure 7.3: Entropy for patients calculated from baseline RNVG phase image, split into two groups based on LVEF decline.

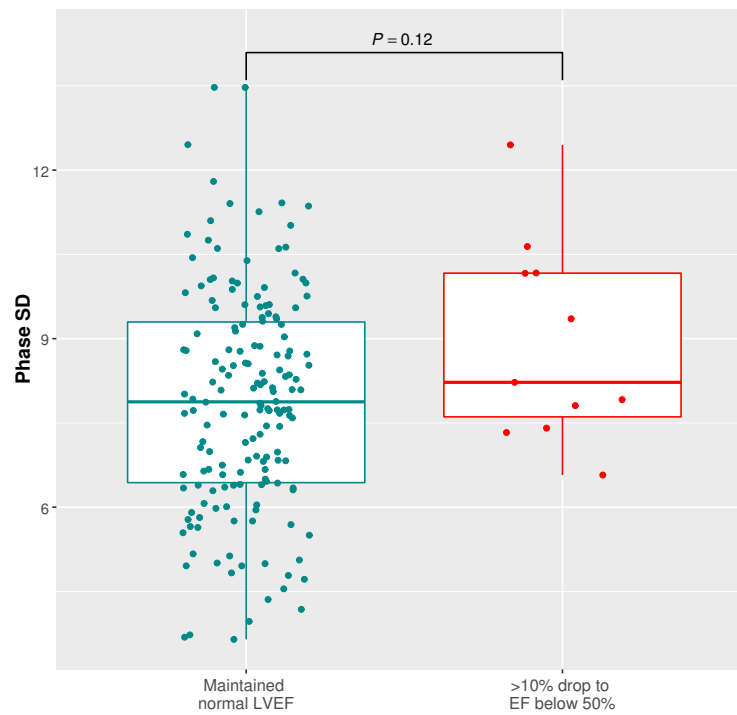


Figure 7.4: Phase SD for patients calculated from baseline RNVG phase image, split into two groups based on LVEF decline.

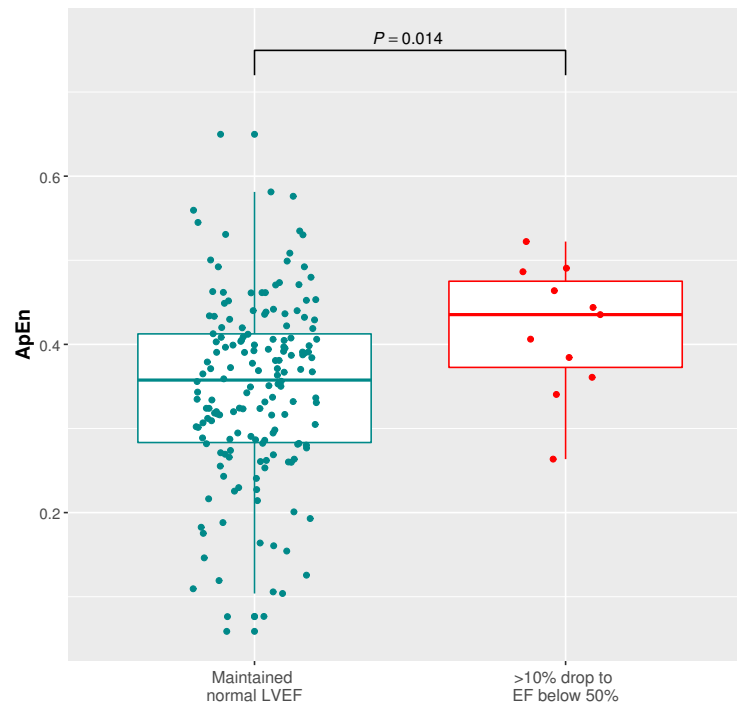


Figure 7.5: $ApEn$ for patients calculated from baseline RNVG phase image, split into two groups based on LVEF decline.

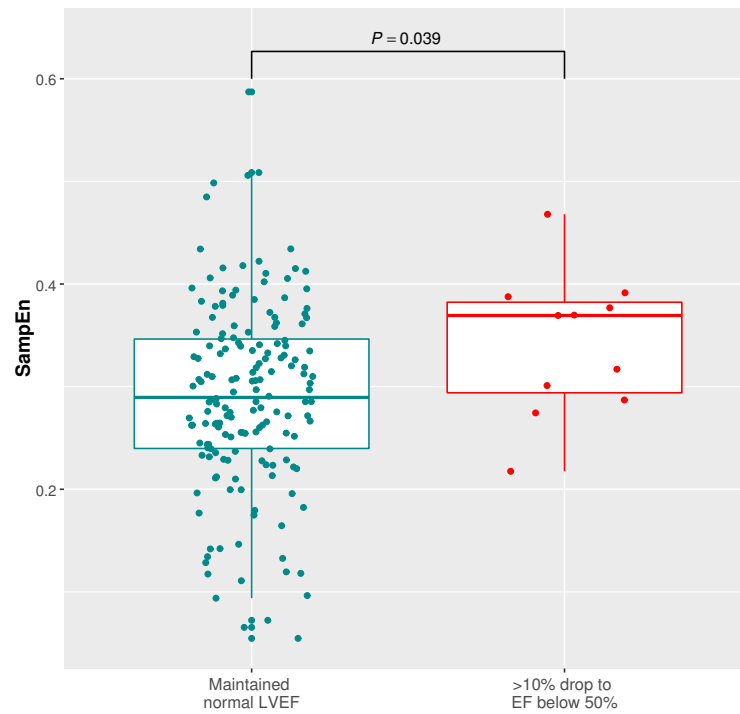


Figure 7.6: *SampEn* for patients calculated from baseline RNVG phase image, split into two groups based on LVEF decline.

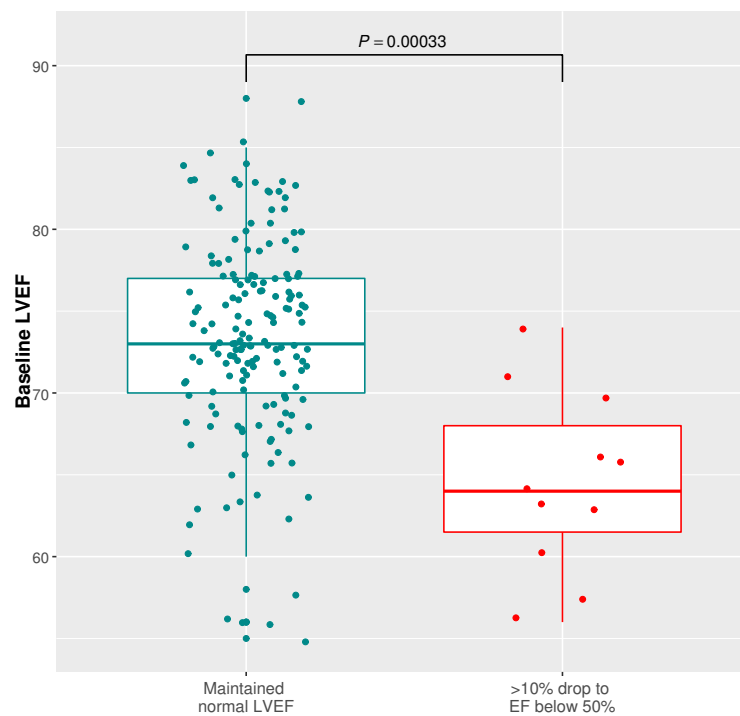


Figure 7.7: Baseline LVEF for patients, split into two groups based on LVEF decline.

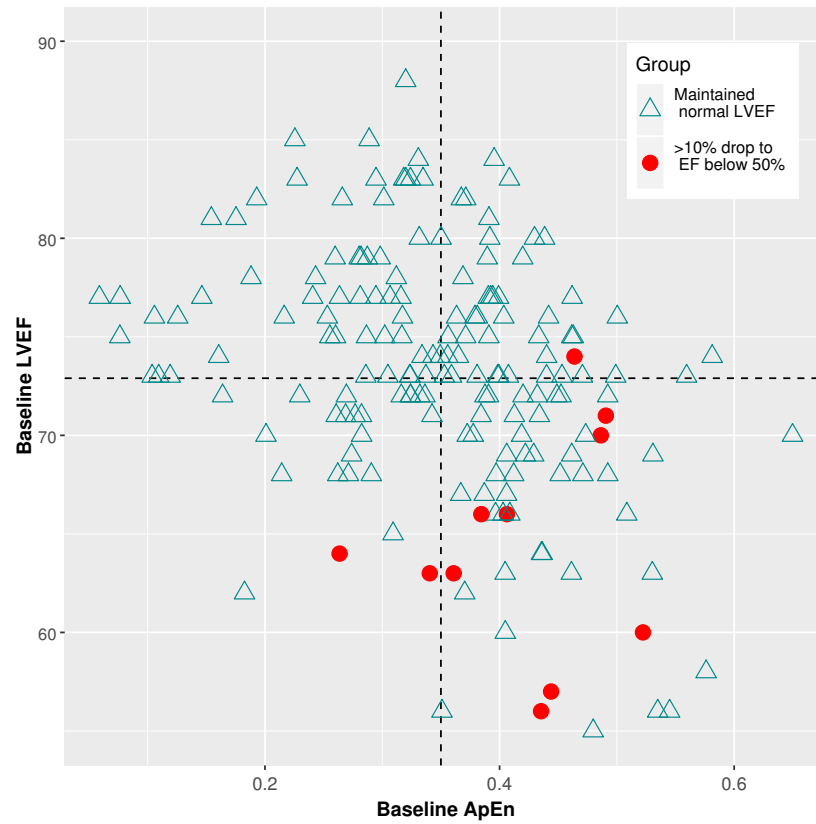


Figure 7.8: Baseline LVEF plotted against baseline $ApEn$ for both groups. The dashed lines represent the mean $ApEn$ and mean LVEF of the test population.

Table 7.2: Logistic Regression Model to predict response to cardiotoxic chemotherapy

Predictor	Coefficient	P value	AUC	Accuracy
(Intercept)	53.7263	0.013		
<i>ApEn</i>	-99.1931	0.004		
Baseline LVEF	-0.8518	0.009		
<i>ApEn</i> , LVEF interaction	1.5253	0.033		
Model			0.88	93%

Logistic regression model results built from 10-fold cross validation with 3 repeats. The p-values for significant variables are in bold.

not unexpected as *SampEn* is a modification of *ApEn*, and they were calculated from the same data.

Improved discrimination between the groups was achieved by considering the combination of baseline LVEF and baseline *ApEn*. The results suggest that patients with a lower LVEF and higher *ApEn* at their baseline RNVG (lower right quadrant in Figure 7.8) are at a higher risk of developing cardiac dysfunction during or after treatment. Of the patients tested, no one who fell within the top left quadrant in Figure 7.8 had an LVEF drop to below 50%. In addition, the logistic regression model demonstrated that the interaction between *ApEn* and baseline LVEF was significant, suggesting that LVEF combined with *ApEn* has predictive value at the baseline scan.

These results should be interpreted with caution due to the small number of patients who had a significant LVEF decline during treatment. Further work with additional data for testing would be desirable. The results agree well with published studies using echocardiography which have investigated global longitudinal strain to detect sub-clinical changes before any decline in LVEF, with several studies demonstrating that a change in global longitudinal strain during treatment precedes the drop in LVEF [24–27]. Ali *et al.* [28], found that global longitudinal strain could detect subtle left ventricular abnormalities prior to chemotherapy and was predictive of cardiac events. They also found a significant difference in baseline LVEF between the groups. Cullen *et al.* investigated the use of *ApEn* from RNVG for serial assessment of patients receiving Herceptin [36]. This small study found a significant change in ejection fraction and *ApEn* over the course of treatment, but this study did not assess *ApEn* as a predictor of LVEF decline. Despite published results using strain to demonstrate subtle abnormalities before treatment, this is the first RNVG study investigating *ApEn* as a predictive measure.

ApEn has shown to be promising in this patient cohort and can be calculated quickly without any additional scanning, dose or processing time. To summarise, patients with higher *ApEn* and low LVEF at baseline may be more susceptible to the cardiotoxic effects of the therapy. Further improvement could potentially be achieved by combining *ApEn* with other clinical parameters

and assessing as part of a wider texture analysis. Additional data would be necessary to define a decision boundary using these parameters to highlight those most at risk.

Limitations of Study

Due to this study being retrospective, limited information was available detailing the treatment and doses. Therefore, this study does not discriminate between different chemotherapy regimes. Of the 177 patients included in this study, only 11 had an LVEF decline of more than 10% to below 50%. Although the initial results are promising, a larger prospective study would be desirable to continue this work.

7.5 Conclusions

Patients who have a normal LVEF before treatment may have subtle phase abnormalities, which can be detected from the baseline RNVG. The results of this study suggest that *ApEn* combined with the baseline LVEF could potentially predict which patients are at a higher risk of developing cardiac dysfunction, as measured by a decline in LVEF, before treatment commences. If patients who are at a higher risk of cardiac dysfunction can be identified, patient treatment and monitoring could become more personalised to the individual, helping to achieve the best outcome for each patient.

Chapter 8

Effect of Beta-blockade on Dyssynchrony

This chapter investigates the effect of beta-blocker therapy on dyssynchrony for symptomatic patients with heart failure with reduced ejection fraction (HFrEF), as assessed by radionuclide ventriculography (RNVG) phase. One of the knowledge gaps highlighted by the European Society of Cardiology (ESC) guidelines [16] is identifying non-responders to current guideline-advised medical treatment. Therefore, another aim is to determine whether baseline dyssynchrony can predict which patients will respond to beta-blockers by investigating baseline clinical data and dyssynchrony measurements from the RNVG phase. Subgroups split by ischaemic aetiology will also be investigated. This work detailed in this chapter has been submitted to the Journal of Nuclear Cardiology.

8.1 Introduction

Heart failure affects approximately 1-2% of the adult population in developed countries, increasing to over 10% for those >70 years old [87–90]. Heart failure occurs when the heart can no longer meet the demands of the body, resulting from a variety of causes, including abnormalities of the myocardium, valves, pericardium, endocardium, heart rhythm and conduction. Common symptoms of heart failure include; shortness of breath, fatigue and ankle swelling. Various treatments are available which aim to improve symptoms, morbidity and mortality. However, identifying the underlying cause is crucial to determine the most appropriate treatment.

There are four different stages of heart failure defined by the New York Heart Association (NYHA) class system [91] as outlined in Table 8.1. The NYHA class system is widely used in cardiology but has limitations due to being defined only by patient symptoms. Patients with a higher NYHA class of heart failure are more likely to have severely impaired cardiac function. It was previously thought that heart failure was associated with reduced LVEF. However, it is now known that heart failure can occur with reduced LVEF (HFrEF), moderate LVEF (HFmEF), or preserved LVEF (HFpEF). In the European society of cardiology guidelines, reduced LVEF is defined as <40%, moderate LVEF is 40-49%, and preserved LVEF is >50%. This chapter

focuses on non-valvular heart failure with reduced ejection fraction HFrEF. In HFrEF, LVEF is known to be a good predictor of outcome and is included in the decision criteria for many HFrEF treatments [16].

Patients with heart failure will often have a dyssynchronous ventricular contraction, and there is interest in quantifying left ventricular dyssynchrony for patients with HFrEF. For example, there have been many studies published investigating imaging parameters as predictors to cardiac resynchronisation therapy (CRT) response with varying degrees of success as summarised in the review by Hawkins *et al.* [19]. Despite promising results in single centre studies [92, 93], the results have not been reproduced in larger multi-centre trials [18], leaving many unanswered questions in this area. RNVG phase parameters offer an alternative index for the quantification of ventricular dyssynchrony and may be a valuable adjunct in the assessment of patients with heart failure.

Table 8.1: NYHA Class Definition

Class	Patient symptoms
I	No limitation of physical activity. Ordinary physical activity does not cause undue fatigue, palpitation, dyspnoea (shortness of breath)
II	Slight limitation of physical activity. Comfortable at rest. Ordinary physical activity results in fatigue, palpitation, dyspnoea (shortness of breath)
III	Marked limitation of physical activity. Comfortable at rest. Less than ordinary activity causes fatigue, palpitation, or dyspnoea.
IV	Unable to carry on any physical activity without discomfort. Symptoms of heart failure at rest. If any physical activity is undertaken, discomfort increases.

8.1.1 Beta-blockade Therapy

Beta-blockade therapy is well established and currently recommended by the ESC guidelines as first line treatment for patients in symptomatic HFrEF [16]. Beta-blockers were originally contraindicated for heart failure patients due to their predicted negative inotropic effect. Negative inotropes weaken the force of the heart's contraction. However, somewhat paradoxically, beta-blockers reverse adrenoceptor downregulation and improve both morbidity and mortality via several potential mechanisms [94]. In addition, the direct effect of decreasing heart rate may also be beneficial by decreasing myocardial oxygen demand and improving coronary blood flow.

Several large scale clinical trials have demonstrated the benefits of beta-adrenoceptor blockers for heart failure patients, reducing morbidity and mortality. [95, 96]. It is known that post

beta-blockade therapy, patients show significantly improved LVEF [97], but the effect of beta-blockade on cardiac dyssynchrony has not been widely investigated.

Several published studies investigate the use of echo derived dyssynchrony parameters, such as septal to lateral wall delay for heart failure patients [12, 15, 98]. However, there are currently no published studies investigating the effect of beta-blocker using dyssynchrony measured from RNVG imaging. Currently, there is no consensus on the definition of a responder, but an improvement in LVEF or 10% or more is widely accepted as a significant improvement of left ventricular function. The importance of right ventricular function has not been as widely investigated as that of the left ventricle, but there is an increasing interest in the field in understanding right ventricular involvement in heart failure [99].

8.2 Method

8.2.1 Study outline

A secondary analysis of a previously performed prospective study was carried out on data from 98 patients who were part of a study at Glasgow Royal Infirmary investigating beta-blocker therapy for HFrEF in 2005-2006. An application to the ethics board to further investigate the data was approved. Table 8.2 details the recruitment criteria for the original study. All patients who were enrolled had evidence of left ventricular systolic dysfunction, NYHA class II-IV, and were stabilised on standard heart failure treatment. Patients who had recent intervention were excluded to ensure that any change in function would be secondary to beta-blocker and not intervention related. Those with atrial fibrillation or severe valve disease were excluded as these conditions can make the assessment of left ventricular systolic function less reliable.

As part of this study, the patients had an RNVG and Thallium-201 myocardial perfusion imaging (MPI), titration of beta-blocker and a second RNVG six months post beta-blocker. Patients were initially given 1.25 mg of Bisoprolol (a beta-blocker), with the dose increasing stepwise to 2.5 mg, 5 mg, 7.5 mg and 10 mg at intervals of two weeks. Before each step increase, patients underwent clinical review. Each patient continued on their maximum tolerated dose of Bisoprolol. Patients who did not tolerate the prescribed beta-blockers and those who did not attend the second RNVG scan were excluded from this study. Of the 12 patients who were excluded, 8 patients did not tolerate beta-blocker, 3 patients did not attend for the second RNVG for unknown reasons, and 1 patient died before the second RNVG. After the exclusion criteria were applied, there were 86 patients remaining. The baseline characteristics are listed in Table 8.3, including Age, Sex, NYHA class, presence of diabetes and hypertension, and whether the patient has an implantable cardiac defibrillator (ICD).

Table 8.2: Study inclusion and exclusion criteria

Inclusion Criteria
Left ventricular systolic dysfunction as assessed by echo or RNVG (<40%)
Chronic stable HF symptoms (NYHA class II-IV)
Stabilised on standard HF treatment (without beta-blocker)
Clinically stable and free from all cause admission for 1 month
Exclusion Criteria
Use of beta-blockers in the last 6 months
Asthma or COPD with significant reversibility on PFTs
Atrial fibrillation
PCI within 3 months
CABG within 6 months
MI within 1 year
Resting HR < 60 bpm
Sitting systolic blood pressure < 85 mmHg
Severe valve disease

The patient cohort was split depending on whether or not they had heart failure of ischaemic aetiology. Ischaemia was defined based on the following criteria,

- (i) A stenosis of more than 50% in at least one of the three major coronary arteries as assessed by coronary angiogram
- (ii) Previous MI or PCI
- (iii) Thallium-201 MPI (defined by two experienced reporters)

Ischaemia from the myocardial perfusion scan was defined by two experienced reporters. Of this patient cohort, 54 were ischaemic, and 32 were non-ischaemic. For this study, an improvement in LVEF of 10% was used as the definition of response to beta-blocker therapy.

8.2.2 Data Acquisition and Processing

All patients underwent planar RNVG imaging before and six months after beta-blockade. In-vivo labelling was performed using intravenous administration of pyrophosphate 20 minutes prior to injection of Technetium-99m pertechnetate. The administered dose for each scan was 800 MBq (21.6mCi). The gamma camera was positioned to achieve the best septal separation

between the left and right ventricles. Imaging was acquired on an Optima gamma camera (GE Healthcare, Waukesha, WI) using list mode acquisition and processed using MAPS Link Medical 10000 software. The raw data were reconstructed into a 24 frame 64 x 64 matrix with the exclusion of heartbeats 10% greater than the mean inter-beat (R-R) interval.

Left and right ejection fractions were calculated from the gated images by two experienced operators, using a single region of interest method. This technique systematically underestimates the ejection fraction, but it has higher reproducibility than a dual region technique. It is essential to understand the normal range for the technique used because not all ejection fraction measurements are interchangeable. The locally established normal range for LVEF by this method is $> 40\%$ and the inter-observer variability is 3.1% [100]. Synchrony, entropy, approximate entropy ($ApEn$), sample entropy ($SampEn$), and phase standard deviation were calculated from the RNVG phase images both pre and post beta-blockade as previously described in Chapter 3.

8.2.3 Statistical Analysis

Shapiro-Wilk's test was used to check the normality for each parameter, and significance testing was performed, using the t-test or Wilcoxon rank-sum test, depending on the outcome of the univariate test of normality. For paired data, a paired two-sample t-test or Wilcoxon signed-rank test was used. The Chi-squared test was used to test the significance of categorical parameters. Lasso regression was used for feature selection. A logistic regression model was fitted in R using the selected predictors. Additional logistic regression models were fitted for a subset of the data using only the most important predictors. The area under the receiver operator curve (AUC), accuracy and significance were reported for each model. A p-value of < 0.05 was considered significant for all tests as previously described. The correlation between the parameters was also tested.

8.3 Results

8.3.1 Effect of Beta-Blocker on Dyssynchrony

The patient baseline characteristics are summarised in Table 8.3 for all 86 patients and split by ischaemic (54 patients) and non-ischaemic aetiology (32 patients). The data are presented as mean (\pm standard deviation) for continuous variables and absolute number (% of the population) for categorical data. A Chi-squared test was used for categorical data and two sample t-test or Wilcoxon rank-sum test was used for significance testing depending on the normality of the specific variable. These results show a significant difference in age between the ischaemic and non-ischaemic groups; the non-ischaemic group was younger, with a mean age of 54. Not unexpectedly, there are more diabetic patients in the ischaemic group. There was no significant difference between sex, hypertension, ICD or NYHA class.

Figure 8.1 displays the scatter plots showing the correlation for each pair of variables on the lower left area with the associated Pearson correlation value on the upper right area of the figure. The variable names are displayed along the edges of the matrix and the diagonal boxes show the distribution for each individual variable. This figure shows that dyssynchrony predictors do not correlate as highly as the normal patients in Chapter 6 or breast cancer patients in Chapter 7. The scatter plots and associated Pearson correlation values demonstrate that LVEF and RVEF do not correlate strongly with the dyssynchrony parameters.

Comparison was made pre and post beta-blockade as summarised in Table 8.4. This table shows mean values for each of the dyssynchrony parameters, LVEF and RVEF. The significance test was selected based on the normality of the data. The p-values demonstrate that there was a significant improvement in all of the dyssynchrony parameters, LVEF, and RVEF measured post beta-blockade. The dyssynchrony values summarised in the table suggest that this patient cohort has severe mechanical dyssynchrony compared with the normal patients in Chapter 6 and the chemotherapy patients in Chapter 7. The mean values for all of the dyssynchrony parameters, both pre and post beta-blocker, fall outside of the normal range defined in Chapter 6. The patients were divided into ischaemic and non-ischaemic groups as shown in Table 8.5, where the dyssynchrony, LVEF, and RVEF were assessed both pre and post beta-blockade. The table shows that both the ischaemic and non-ischaemic groups demonstrated improved dyssynchrony, LVEF, and RVEF after beta-blockade. The only parameter that did not significantly improve after beta-blockade was *ApEn* for the non-ischaemic group. *ApEn* did improve from 0.54 to 0.49 for the non-ischaemic group, but this was not significant, possibly due to the small number of patients in this group (32 patients). From Table 8.5 it appears that the non-ischaemic group have more left ventricular dyssynchrony than the ischaemic group at baseline, but this difference was not significant for any of the dyssynchrony parameters ($p > 0.05$). There was minimal difference between the ischaemic and non-ischaemic patients when assessing dyssynchrony with entropy and *ApEn*.

8.3.2 Predicting Response to Beta-Blocker

The patients were split into two groups, based on response to beta-blocker, as defined by an increase in LVEF of 10% or more by RNVG. Based on this definition, 36 patients responded to beta-blocker, and 50 patients did not. Table 8.6 shows the clinical and dyssynchrony parameters at baseline for each group. The data in this table are presented as mean (\pm standard deviation) for continuous variables and absolute number (% of the population) for categorical data. For the imaging parameters tested, synchrony, entropy, *SampEn*, phase standard deviation, LVEF, and RVEF were significantly different between the two groups. Overall, the patients who responded to beta-blocker had a more dyssynchronous left ventricular contraction and lower left and right ejection fractions than those who showed no significant improvement in LVEF. There was no significant difference in sex, presence of hypertension, or diabetes. The results for the full group

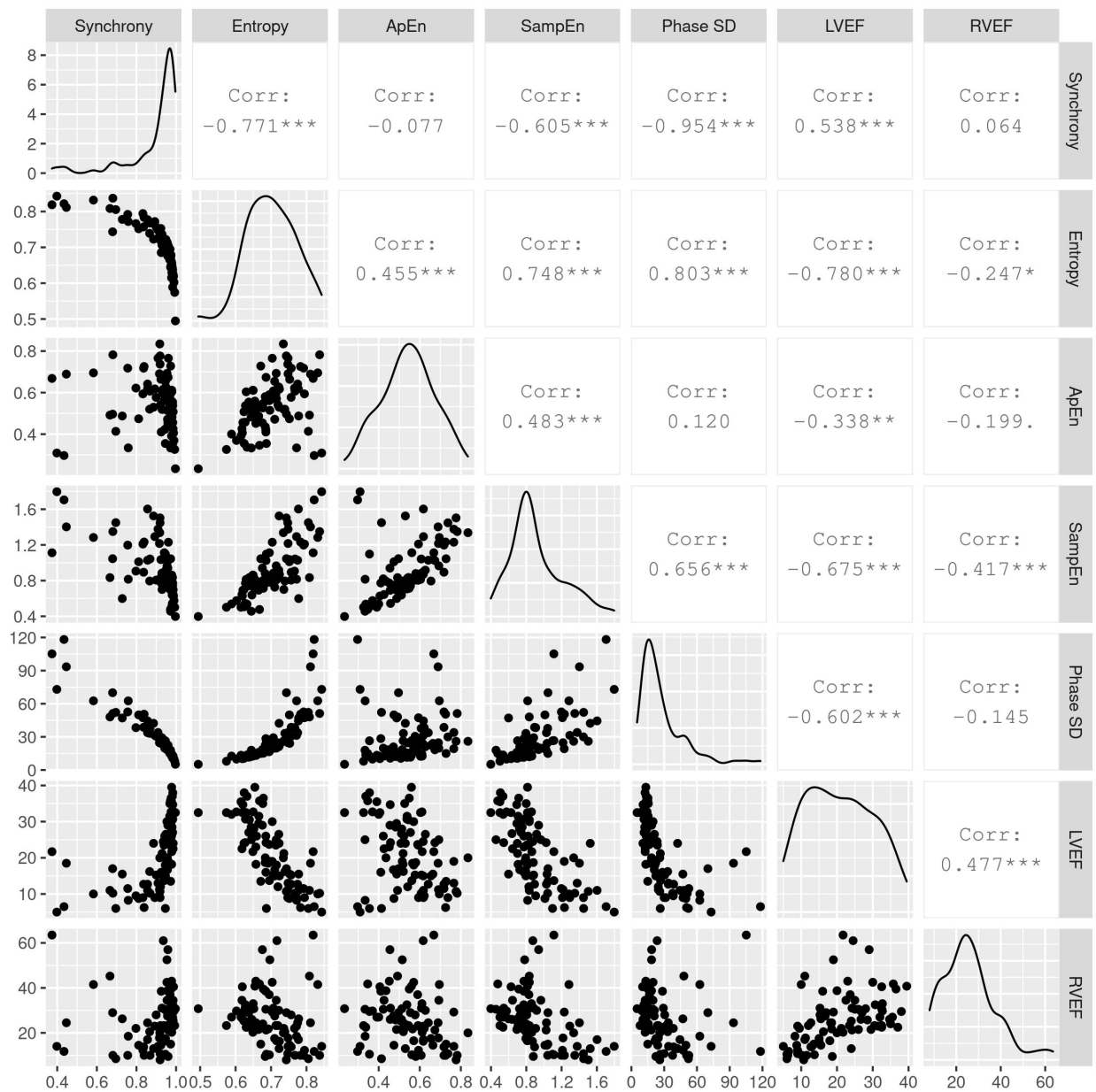


Figure 8.1: Scatter plots showing the correlation for each pair of variables with the associated correlation value, with the variable names displayed along the edges of the matrix. The diagonal boxes display the distribution for each individual variable. The scatter plots on lower left area show the relationship between each pair of variables, and the Pearson correlation coefficient for each pair of variables is displayed on the upper right area.

Table 8.3: Baseline patient characteristics

	All (n= 86)	Ischaemic (n=54)	Non-ischaemic (n=32)	P value
Age	64 (\pm 14)	69 (\pm 9)	54 (\pm 16)	< 0.001
Female	31 (36%)	18 (33%)	13 (41%)	0.65
Hypertensive	42 (49%)	29 (54%)	13 (41%)	0.34
Diabetic	19 (22%)	16 (30%)	3 (9%)	0.05
ICD	2 (2%)	0	2 (6%)	0.26
NYHA Class II	48 (56%)	30 (56%)	18 (56%)	} 0.42
NYHA Class III	37 (43%)	24 (44%)	13 (41%)	
NYHA Class IV	1 (1%)	0	1 (3%)	

ICD = Implantable cardioverter defibrillator.

Data are presented as mean (\pm standard deviation) for continuous variables and absolute number (% of the population) for categorical data. To test significance, a Chi-squared test was used for categorical data and two sample t-test or Wilcoxon rank-sum test was used for continuous data depending on the normality of the specific variable.

in Table 8.6 demonstrate a significant difference for ischaemic aetiology and age, suggesting that younger patients and those with non-ischaemic heart failure were more likely to respond to beta-blocker therapy. However, age is not significant for either group once the data is split by ischaemic aetiology. This suggests that the significant difference in age for those who responded to beta-blocker is because the ischaemic group is older, rather than age itself being a predictor.

Plots for the full group and ischaemic/non-ischaemic subgroups for each parameter are presented in Figures 8.2 to 8.8. Each plot has three panels showing boxplots for all patients, ischaemic patients, and non-ischaemic patients. For each patient group, the boxplots compare the responders and non-responders. A higher value of *ApEn*, *SampEn*, phase standard deviation, and entropy corresponds to worse dyssynchrony, while a lower value of synchrony corresponds to worse dyssynchrony. The plots for synchrony, entropy, *SampEn*, phase standard deviation, LVEF, and RVEF show a significant difference between the responders and non-responders. This difference becomes larger when considering only the non-ischaemic group. None of the parameters assessed demonstrated a significant difference for the ischaemic group.

Splitting the cohort by ischaemic aetiology demonstrates that dyssynchrony was significantly worse at baseline for the non-ischaemic patients who responded to beta-blocker therapy. Dyssynchrony also was predictive of the non-ischaemic group's response. In contrast, for the ischaemic group, none of the dyssynchrony parameters were significantly different between responders and non-responders, as seen in Table 8.7. The table shows that there was no signif-

Table 8.4: Comparing RNVG parameters pre and post beta-blockade

Predictor	Pre BB Mean (\pm SD)	Post BB Mean (\pm SD)	Significance test	P-value
Synchrony	0.90 (\pm 0.14)	0.95 (\pm 0.09)	Wilcoxon signed-rank	< 0.001
Entropy	0.70 (\pm 0.07)	0.65 (\pm 0.06)	Paired two sample t-test	< 0.001
ApEn	0.54 (\pm 0.13)	0.48 (\pm 0.13)	Paired two sample t-test	< 0.001
SampEn	0.91 (\pm 0.3)	0.72 (\pm 0.21)	Wilcoxon signed-rank	< 0.001
Phase SD	28.0 (\pm 21.2)	18.8 (\pm 14.3)	Wilcoxon signed-rank	< 0.001
LVEF (%)	21 (\pm 9)	30 (\pm 11)	Wilcoxon signed-rank	< 0.001
RVEF (%)	26 (\pm 12)	33 (\pm 12)	Wilcoxon signed-rank	< 0.001

SD = standard deviation. A paired significance test for each parameter was selected based on normality of the specific variable.

icant difference in age, sex, presence of hypertension, or diabetes for both the ischaemic and non-ischaemic groups.

Table 8.5: Comparing RNVG parameters pre and post beta-blockage, split by presence of ischaemia

Predictor	Ischaemic (n=54)			Non-ischaemic (n= 32)		
	Pre BB Mean (\pm SD)	Post BB Mean (\pm SD)	P-value	Pre BB Mean (\pm SD)	Post BB Mean (\pm SD)	P-value
Synchrony	0.91 (\pm 0.11)	0.94 (\pm 0.09)	< 0.001	0.87 (\pm 0.17)	0.95 (\pm 0.08)	0.001
Entropy	0.70 (\pm 0.06)	0.66 (\pm 0.07)	< 0.001	0.70 (\pm 0.08)	0.64 (\pm 0.06)	< 0.001
ApEn	0.55 (\pm 0.12)	0.47 (\pm 0.13)	0.001	0.54 (\pm 0.14)	0.49 (\pm 0.14)	0.103
SampEn	0.86 (\pm 0.24)	0.71 (\pm 0.2)	< 0.001	1.00 (\pm 0.37)	0.74 (\pm 0.23)	0.001
Phase SD	25.1 (\pm 16.8)	19.4 (\pm 14.5)	< 0.001	33 (\pm 26.6)	17.9 (\pm 14.1)	0.001
LVEF (%)	21 (\pm 8)	28 (\pm 10)	< 0.001	20 (\pm 11)	32 (\pm 11)	< 0.001
RVEF (%)	28 (\pm 12)	32 (\pm 10)	< 0.001	22 (\pm 10)	35 (\pm 14)	< 0.001

SD = standard deviation. Paired two sample t-test and Wilcoxon signed-rank tests were used to test the significance, depending on normality of the specific variable.

Table 8.6: Baseline clinical and dyssynchrony measures for the full heart failure cohort (n=86), for predicting response to beta-blocker

Predictor	Response to BB (n=36)	No Response (n=50)	Significance test	P-value
Age	58 (\pm 17)	67 (\pm 11)	Wilcoxon rank-sum	0.0182
Female	13 (36%)	18 (36%)	Chi-squared	1.0000
Hypertension	6 (17%)	13 (25%)	Chi-squared	0.3627
Diabetic	15 (42%)	27 (54%)	Chi-squared	0.4438
Ischaemic	17 (47%)	37 (74%)	Chi-squared	0.0210
Synchrony	0.86 (\pm 0.16)	0.92 (\pm 0.12)	Wilcoxon rank-sum	0.0099
Entropy	0.73 (\pm 0.07)	0.69 (\pm 0.07)	Two sample t-test	0.0081
ApEn	0.57 (\pm 0.13)	0.53 (\pm 0.13)	Two sample t-test	0.1361
SampEn	1.05 (\pm 0.34)	0.81 (\pm 0.23)	Wilcoxon rank-sum	0.0008
Phase SD	33.8 (\pm 23.3)	23.9 (\pm 18.7)	Wilcoxon rank-sum	0.0064
LVEF (%)	17 (\pm 8)	24 (\pm 9)	Wilcoxon rank-sum	0.0006
RVEF (%)	21 (\pm 10)	29 (\pm 12)	Wilcoxon rank-sum	0.0002

SD = standard deviation. Data are presented as mean (\pm SD) for continuous variables and absolute number (% of the population) for categorical data. Response is defined as an improvement in left ventricular ejection fraction of more than 10%. To test significance, a Chi squared test was used for categorical data and unpaired two sample t-test or Wilcoxon rank-sum test was used for continuous data depending on the normality of the specific variable.

Table 8.7: Comparing baseline clinical and dyssynchrony measures, split by etiology (n=86), for predicting response to beta-blocker.

Predictor	Ischaemic			Non-ischaemic		
	Responded to BB (n=17)	No Response (n=37)	P-value	Responded to BB (n=19)	No Response (n=13)	P-value
Age	68 (\pm 7)	70 (\pm 10)	0.2878	50 (\pm 18)	60 (\pm 11)	0.1788
Female	6 (35%)	12 (32%)	1.0000	7 (37%)	6 (46%)	1.0000
HTN	5 (29%)	11 (30%)	0.3627	1 (5%)	2 (15%)	0.3627
Diabetic	10 (59%)	19 (51%)	0.4438	5 (26%)	8 (62%)	0.4438
Synchrony	0.93 (\pm 0.07)	0.9 (\pm 0.13)	0.8682	0.8 (\pm 0.18)	0.96 (\pm 0.08)	0.0003
Entropy	0.7 (\pm 0.06)	0.7 (\pm 0.06)	0.7606	0.75 (\pm 0.06)	0.64 (\pm 0.06)	< 0.0001
ApEn	0.56 (\pm 0.12)	0.54 (\pm 0.13)	0.5426	0.57 (\pm 0.14)	0.48 (\pm 0.13)	0.0727
SampEn	0.9 (\pm 0.27)	0.84 (\pm 0.23)	0.4945	1.19 (\pm 0.33)	0.73 (\pm 0.21)	0.0002
Phase SD	22.3 (\pm 10.1)	26.4 (\pm 19)	0.8393	44.1 (\pm 26.9)	16.8 (\pm 16.3)	0.0003
LVEF (%)	20 (\pm 7)	22 (\pm 9)	0.4562	14 (\pm 8)	29 (\pm 8)	0.0003
RVEF (%)	26 (\pm 12)	29 (\pm 12)	0.3763	16 (\pm 6)	30 (\pm 9)	0.0001

SD = standard deviation. Data are presented as mean \pm SD for continuous variables and absolute number with % of the population for categorical data. To test significance, a Chi squared test was used for categorical data and two sample t-test or Wilcoxon rank-sum test was used for continuous data depending on the normality of the specific variable.

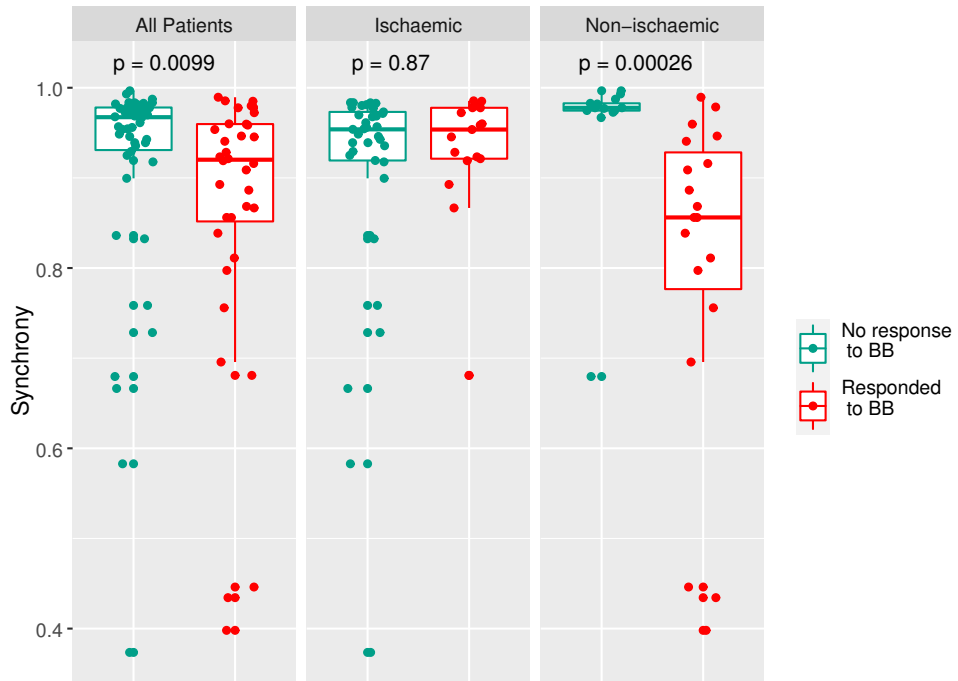


Figure 8.2: Synchrony for heart failure patients, calculated from baseline RNVG phase image and split into two groups based on response to beta-blocker therapy. A lower value of synchrony corresponds to worse dyssynchrony. Significance was tested using a Wilcoxon rank-sum test.

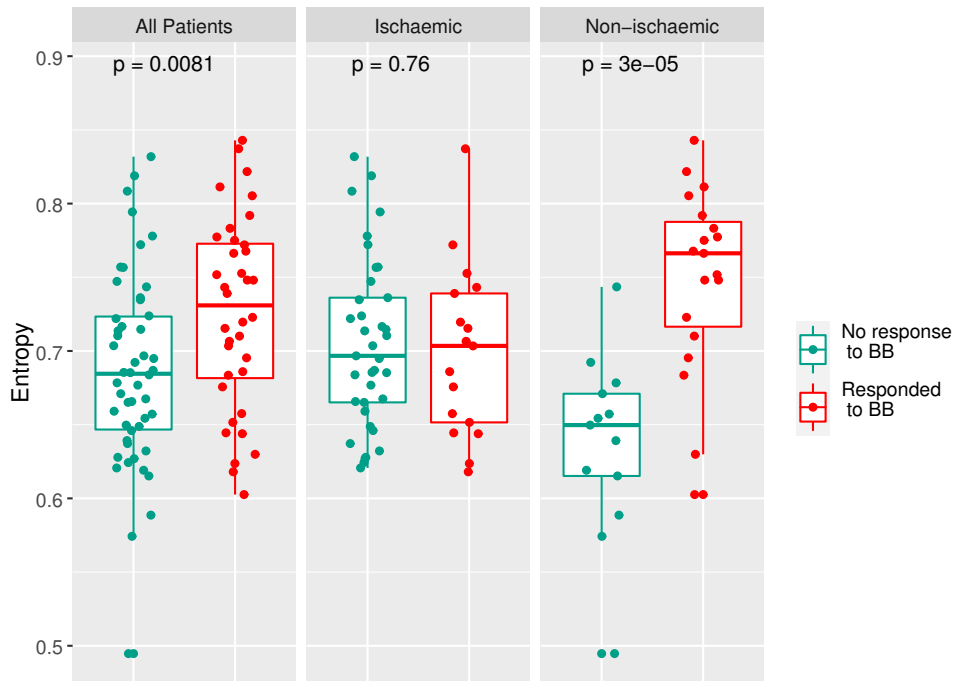


Figure 8.3: Entropy for heart failure patients, calculated from the baseline RNVG phase image and split into two groups based on response to beta-blocker therapy. Higher entropy corresponds to worse dyssynchrony. Significance was tested using a two-sample t-test.

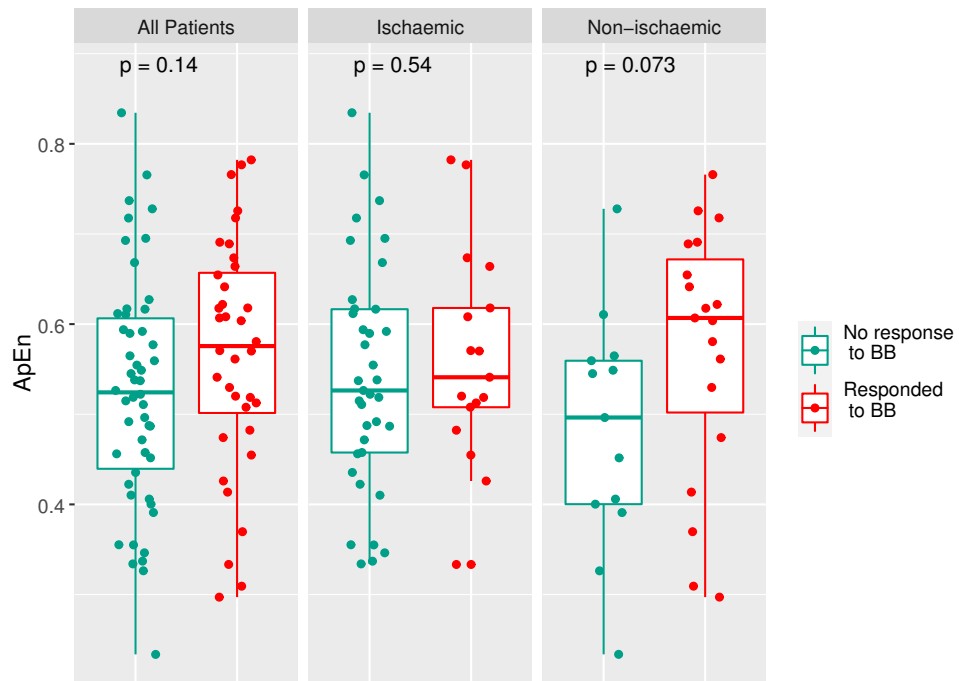


Figure 8.4: $ApEn$ for heart failure patients, calculated from the baseline RNVG phase image and split into two groups based on response to beta-blocker therapy. A higher value of $ApEn$ corresponds to worse dyssynchrony. Significance was tested using a two-sample t-test.

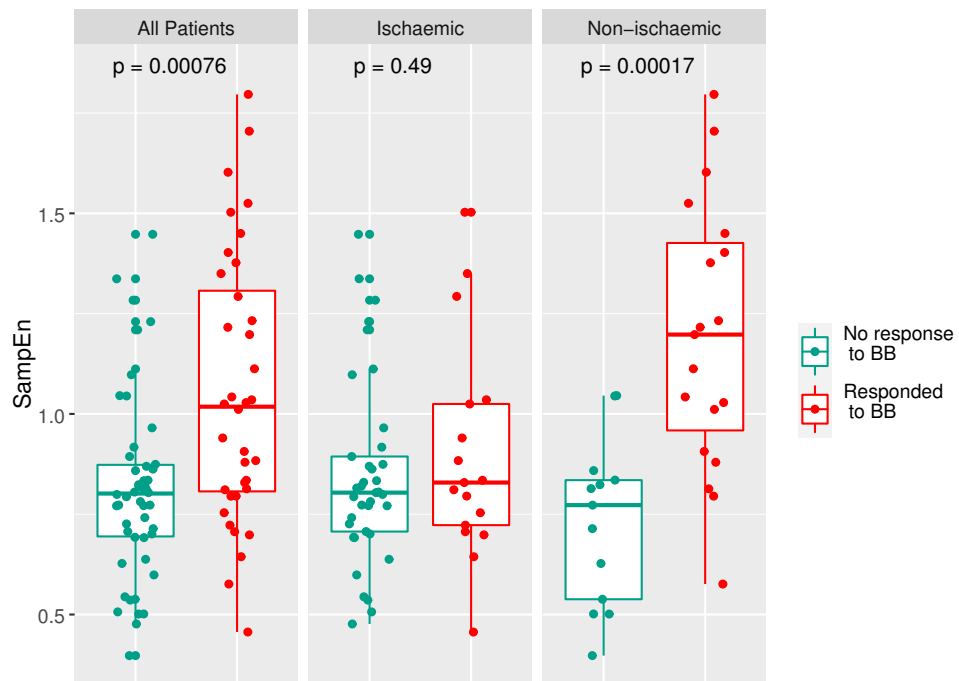


Figure 8.5: $SampEn$ for heart failure patients, calculated from the baseline RNVG phase image and split into two groups based on response to beta-blocker therapy. A higher value of $SampEn$ corresponds to worse dyssynchrony. Significance was tested using a Wilcoxon rank-sum test.

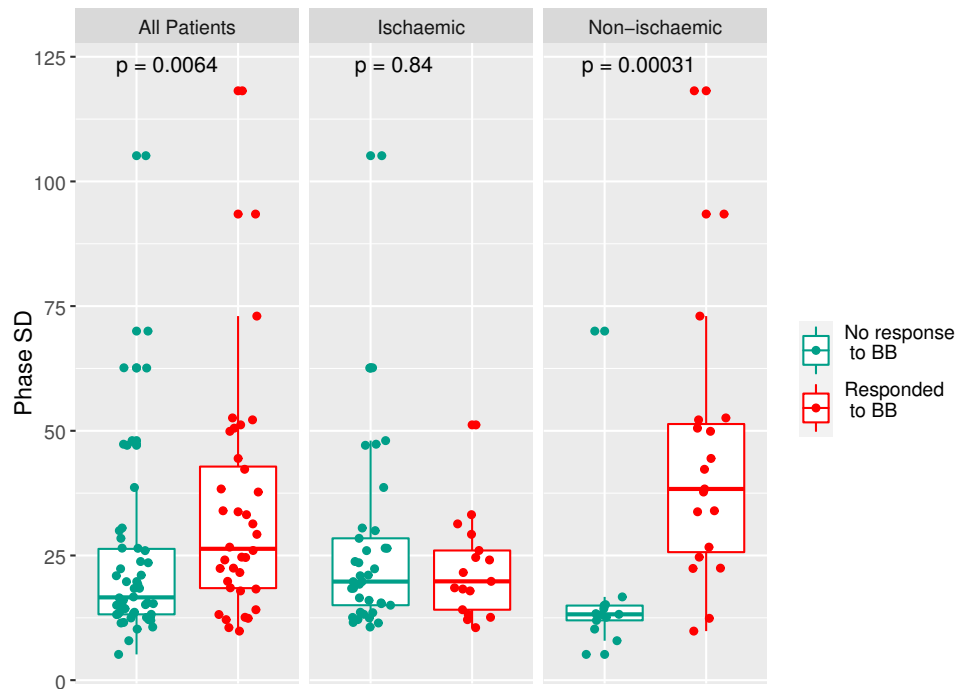


Figure 8.6: Phase standard deviation for heart failure patients, calculated from the baseline RNVG phase image and split into two groups based on response to beta-blocker therapy. Significance was tested using a Wilcoxon rank-sum test.

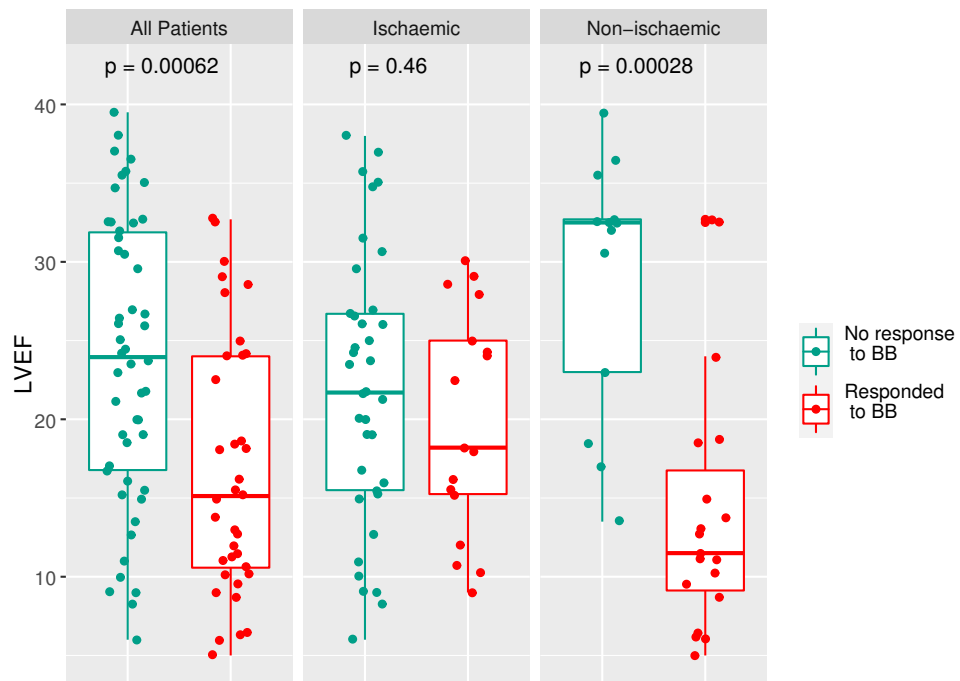


Figure 8.7: Baseline LVEF for heart failure patients, calculated from the baseline RNVG phase image and split into two groups based on response to beta-blocker therapy. Significance was tested using a Wilcoxon rank-sum test.

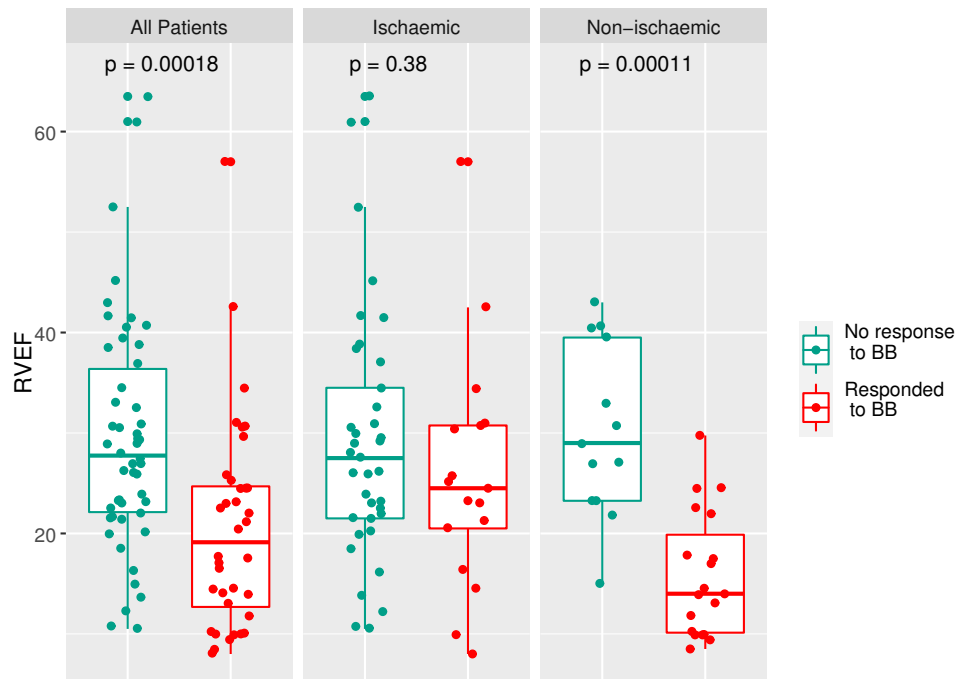


Figure 8.8: RVEF for heart failure patients, calculated from the baseline RNVG phase image and split into two groups based on response to beta-blocker therapy. Significance was tested using a Wilcoxon rank-sum test.

8.3.3 Predictive Models

Logistic regression models were used to try to predict which patients would respond to beta-blockade. The first logistic regression model was created using 6 predictors selected by Lasso regression based variable selection; *SampEn*, ischaemic aetiology, presence of diabetes, LVEF, RVEF and age. There were no significant individual predictors within this model. The accuracy for this model was 71% and the AUC was 0.73.

The non-ischaemic group had a larger proportion of responders and number of individually significant predictors. Therefore, a second model was proposed for the non-ischaemic subgroup, using the same predictors with the exception of ischaemic aetiology. Improved accuracy of 80% and AUC of 0.87 was achieved when considering only the non-ischaemic subgroup. For a simpler interpretation, a third model was fitted for the non-ischaemic subgroup using only *SampEn* and LVEF, achieving an accuracy of 84% and AUC of 0.90. The accuracy and AUC values for each model are summarised in Table 8.8. The three logistic regression models proposed are shown in Table 8.9. The coefficient and corresponding p-value for each predictor within the model are shown.

Table 8.8: Summary of Logistic Regression Models

Model	AUC	Accuracy (%)
1 - All HF (<i>SampEn</i> , ischaemic aetiology, diabetic, LVEF, RVEF, Age)	0.73	71%
2 - Non-ischaemic (<i>SampEn</i> , diabetic, LVEF, RVEF, Age)	0.87	80%
3 - Non-ischaemic (<i>SampEn</i> , LVEF)	0.90	84%

Table 8.9: Logistic Regression Models for predicting response to beta-blockade

Predictor	Model 1		Model 2		Model 3	
	Coefficient	P-value	Coefficient	P-value	Coefficient	P-value
(Intercept)	2.3771	0.3233	17.2665	0.1905	-0.9410	0.7968
SampEn	1.3457	0.2733	5.4841	0.1559	3.6943	0.1799
LVEF	-0.0554	0.1699	-0.2980	0.2065	-0.1017	0.1462
RVEF	-0.0280	0.3256	-0.0622	0.5776	-	-
Diabetic	-0.5273	0.4245	-2.1039	0.7037	-	-
Age	-0.0335	0.1700	-0.2369	0.1744	-	-
Ischaemic	0.4520	0.4585	-	-	-	-

8.4 Discussion

The results suggest that beta-blockers improve dyssynchrony for HFrEF of both ischaemic and non-ischaemic aetiology. As expected LVEF and RVEF also improve post beta-blockade. The results compare well with the studies by Kaya *et al.* and Takemoto *et al.* [98, 101]. Both studies used septal to lateral delay as measured by echo to assess dyssynchrony and did not include any patients with ischaemic heart failure. Kaya *et al.* found that beta-blockade improved left ventricular dyssynchrony and LVEF for heart failure patients with idiopathic dilated cardiomyopathy and left ventricular dyssynchrony. Takemoto *et al.* also found that patients experienced an improvement in both LVEF and dyssynchrony after beta-blocker therapy for patients with a QRS <120ms and sinus rhythm. The mechanism for this improvement is not fully understood.

A second finding of this study is that patients with HFrEF with non-ischaemic aetiology with more severe dyssynchrony were more likely to respond to beta-blocker therapy (defined as an improvement in LVEF of 10% or more). In contrast, dyssynchrony was not predictive of beta-blocker response in the ischaemic subgroup. The difference in response between ischaemic and non-ischaemic aetiology is an interesting finding.

The improvement in left ventricular dyssynchrony may in part be due to the reduced heart rate caused by beta-blockade. There are a number of studies investigating this relationship with varying results. A study using SPECT MPI dyssynchrony by Al-Jaroudi *et al.* found no correlation between heart rate and dyssynchrony for patients with end-stage renal failure [102]. However, this study investigated correlations rather than heart rate changes for individual patients. Another SPECT MPI dyssynchrony study by Barron *et al.* demonstrated that there was a strong correlation between heart rate and dyssynchrony measured by bandwidth and standard deviation when the phase was measured in time but found that bandwidth and standard deviation were unrelated to heart rate when measured in degrees [103].

Several echocardiography studies have also investigated the correlation between heart rate and dyssynchrony. Lafitte *et al.* found that exercise did not have an effect on dyssynchrony for patients with normal left ventricular function, but for patients with heart failure, 37% had no significant change in dyssynchrony, 34% had worsened dyssynchrony, and 29% improved [104]. They also found a significant association between the presence of ischaemic cardiomyopathy and exercise-induced changes in dyssynchrony. Research carried out by Valzania *et al.* found no increase in dyssynchrony for heart failure patients undergoing Dobutamine stress echocardiography [105]. Conversely, Chattopadhyay *et al.* carried out Dobutamine stress echocardiography for heart failure patients and demonstrated a significant increase in dyssynchrony [106]. The studies referred to here were all relatively small studies with varying inclusion criteria for patient selection. The relationship between heart rate and dyssynchrony is not yet fully understood, and further work is needed to answer this question.

Previous research has suggested that response to therapy may differ for ischaemic and non-ischaemic aetiologies. The CIBIS-I trial [97] suggested a difference in ischaemic and non-

ischaemic survival post beta-blocker. However, the trial had lower than expected deaths. No difference in survival between ischaemic and non-ischaemic aetiologies was found in the CIBIS-II trial [107]. The investigators assessed the patients enrolled in CIBIS II and classed them as NYHA class III to IV. However, the mortality rate observed in the trial's placebo arm suggests most patients in the study were likely to be compatible with NYHA class II rather than classes III to IV [108]. This is an example of the limitations and subjective nature of the NYHA class system. The CIBIS trials did not measure dyssynchrony. Possible reasons for the difference could be differing levels of dyssynchrony within the cohorts or different levels of disease.

Improved dyssynchrony has been linked with improved survival, as shown in CRT studies. For example, a sub-study of the EchoCRT trial found that persistent or worsening dyssynchrony six months post CRT was associated with worse clinical outcomes, in particular, heart failure hospitalisations [14]. Bader *et al.* [12] used tissue doppler imaging to measure the maximum delay between septal, lateral, anterior and inferior walls as a measure of dyssynchrony and reported that mechanical dyssynchrony is predictive of heart failure worsening. A study by Cho *et al.* used the maximum delay in an eight segment model to assess dyssynchrony, and they reported that dyssynchrony is a predictor of clinical events for patients with heart failure [15]. Another study by Askari *et al.* suggested that for patients with ischaemic heart failure, the presence of dyssynchrony could be a predictor of heart failure progression [109]. The study assessed dyssynchrony by calculating the standard deviation of time to peak systolic myocardial velocity and the maximum segment delay using a six basal and mid-segment model. There are several methods for assessing dyssynchrony within each imaging modality, and they are not necessarily equivalent. More research is required to establish standardised methods and compare the different techniques.

There are a limited number of studies investigating the effects of the right ventricle in heart failure. This work has suggested that beta-blocker improves RVEF as well as LVEF. There are some small studies published which support this result, including a study by Tatli *et al.* [110] which found that right ventricular systolic performance improved for heart failure patients post beta-blocker, with an associated improvement in left ventricular systolic function. Another study by Giardini *et al.* [111] found that beta-blocker therapy improved RVEF and reduced right ventricular volumes in patients with a systemic right ventricle. Future work investigating dyssynchrony of the right ventricle would be of interest in this cohort.

Knowing which patients will respond to the currently available therapies may be crucial to ensure each patient receives the most appropriate treatment. For this reason, logistic regression models were created to predict beta-blocker response. Limited accuracy (71%) was achieved with Model 1, which was based on all HFrEF patients. Greater success was achieved by considering only HFrEF of non-ischaemic aetiology. The accuracy achieved with Model 2 was 84%. Of the models created, Model 3 (*SampEn* and LVEF) is preferred due to achieving high accuracy with only two predictors for non-ischaemic heart failure patients.

While the effect of dyssynchrony and beta-blockers on survival would be of clinical interest, this cohort is too small to provide any meaningful results. Treatment for these patients would have varied, and some went on to have percutaneous coronary intervention (stent), coronary artery bypass graft, or heart transplant after the study. Previous attempts to create models to predict mortality for heart failure patients have had only moderate accuracy, and those trying to predict a combined endpoint of hospitalisation or death had even poorer results [112, 113].

There are currently no studies using newer echo dyssynchrony parameters, such as global longitudinal strain, to investigate the effect of beta-blockers on cardiac dyssynchrony. This study is the only work to date assessing dyssynchrony for heart failure patients using RNVG phase parameters. Heart failure treatment would benefit from further investigation of mechanical dyssynchrony in larger trials.

8.4.1 Limitations

The results are from a single centre study, limited by a small patient sample with no control group. The model for predicting beta-blocker response had high accuracy but would require further testing with an unseen data set. This study also assumes patient compliance with taking prescribed drugs. Assessment of the right ventricular ejection fraction by planar RNVG is less accurate than other techniques due to the right ventricle overlapping with the right atrium in the best septal view.

8.5 Conclusions

An improvement in dyssynchrony, LVEF, and RVEF, was measured six months post beta-blockade for both ischaemic and non-ischaemic groups. This research also suggests that patients with non-ischaemic heart failure and dyssynchronous left ventricular contraction are more likely to respond to beta-blocker therapy. A larger study with data from multiple centres would be desirable to confirm the interesting results of this study.

Chapter 9

Summary and Conclusions

This research has successfully demonstrated the value of novel dyssynchrony parameters calculated from radionuclide ventriculography (RNVG) phase images, including synchrony, entropy, phase standard deviation, approximate entropy (*ApEn*), and sample entropy (*SampEn*). A methodology to optimise *ApEn* and *SampEn* for this application has been developed, demonstrated using simulated data, then validated with clinical results. The results of this work highlight the importance of optimising input parameters when using novel indices, such as *ApEn* and *SampEn*, to characterise clinical images. The dyssynchrony parameters demonstrated high intra-operator reproducibility, in agreement with the results of other published work that investigated RNVG phase. Further investigation would be required to confirm the reproducibility and normal range for clinical use at other sites. All of the dyssynchrony parameters that were assessed demonstrated a significant difference between myocardial infarction, left bundle branch block, and normal patients. A normal range has been suggested for each parameter based on the analysis carried out with the normal patient group using the optimised sequence length m , and tolerance value r for *ApEn* and *SampEn*.

The optimised parameters were applied in the assessment of various clinical patient groups. This is the first time *ApEn* and *SampEn* have been used to measure cardiac dyssynchrony to predict patient outcomes. The dyssynchrony parameters were used to assess breast cancer patients who received cardiotoxic cancer therapy and patients with heart failure (with reduced ejection fraction) pre and post beta-blockade therapy. Predictive models using logistic regression were successfully established for both of these patient cohorts. The predictive models achieved a high accuracy using 10-fold cross-validation. However, further testing with unseen data would be necessary to validate the models fully. In both the breast cancer and heart failure clinical studies, *SampEn* performed better than synchrony, entropy and phase standard deviation. *ApEn* and *SampEn* both performed well for the group of breast cancer patients, suggesting that *ApEn* may be useful for detecting mild dyssynchrony. However, *SampEn* was superior to *ApEn* when applied to the heart failure patients with more severe dyssynchrony.

The results from the study investigating patients who received cardiotoxic therapy suggest

that dyssynchrony parameters applied to the baseline RNVG can detect subtle phase abnormalities. The data from this study indicates that *ApEn* combined with the baseline LVEF could potentially predict which patients are at a higher risk of developing left ventricular dysfunction following cardiotoxic chemotherapy, as measured by LVEF decline before treatment commences. This is a novel result that has not previously been demonstrated with RNVG. Patient treatment and monitoring could become more personalised if patients at a higher risk of cardiac dysfunction could be identified earlier, helping to achieve the optimal outcome for each patient.

The beta-blocker study for patients with heart failure demonstrated that dyssynchrony, and left and right ventricular ejection fraction improve after beta-blocker for both ischaemic and non-ischaemic groups. This result compares well with several small published echo dyssynchrony studies. It is already established that beta-blockade therapy significantly improves LVEF, but its effect on cardiac dyssynchrony has not previously been widely investigated. A second finding from this study is that patients with non-ischaemic heart failure and dyssynchronous left ventricular contraction are more likely to respond to beta-blocker therapy. Identifying non-responders to current guideline-advised medical therapy is essential to ensure each patient receives the most appropriate treatment. The difference in response between ischaemic and non-ischaemic aetiology is an interesting finding which is discussed in the literature, but there is currently no consensus in this area. This study is the only work to date assessing dyssynchrony for heart failure patients using RNVG phase analysis. A larger study with data from multiple centres would be desirable to confirm the interesting results of this study.

The results have demonstrated that dyssynchrony can be measured by RNVG phase analysis and has been shown to be useful in predicting patient outcomes for several different patient groups. This research suggests that assessing and quantifying mechanical dyssynchrony could be of clinical benefit. Combining *ApEn* or *SampEn* with LVEF provided additional information in both studies. Predictive models that combine dyssynchrony with other known predictors may improve clinical decision making. This research was carried out using dyssynchrony measures from RNVG phase; however, the clinical results may apply to other imaging modalities. Comparisons between dyssynchrony measured from different imaging modalities will be important as dyssynchrony starts to play a more significant role in cardiac guidelines and decision making. Currently, there is no gold standard for evaluating mechanical dyssynchrony, but standardisation and normal ranges will be essential to provide meaningful results and allow comparison between different sites, techniques, and software.

Future work investigating the potential of dyssynchrony calculated from RNVG phase images to predict cardiac resynchronisation therapy (CRT) response would be an interesting application for this research. The ability to predict response in this patient cohort would have substantial clinical benefits. Approximately 30% of patients who currently undergo CRT therapy are classified as non-responders. However, some echocardiography studies have suggested a significant difference in dyssynchrony between responders and non-responders before CRT

implantation. At present, there is not enough evidence to suggest that the selection criteria for cardiac resynchronisation should include mechanical dyssynchrony, but there has been a significant amount of interest in using dyssynchrony for this application. To date, the research is primarily using echo derived dyssynchrony parameters rather than RNVG phase. This is an area where further research is necessary.

Overall, this research strengthens the idea that dyssynchrony can predict patient outcomes and improve clinical decision making. This proof of concept work was carried out as a single centre, retrospective study with a single processing system and fixed imaging parameters. A larger prospective multi-centre trial would be required to confirm and expand on the results within this thesis before being implemented clinically. In addition, full testing of the prediction models would require further work with new unseen data. There would also be a clinical benefit in comparing dyssynchrony measured from RNVG against dyssynchrony from other modalities, such as echocardiography and MRI. In particular, the comparison of RNVG phase parameters to more established echocardiography dyssynchrony measures such as global longitudinal strain. Where possible, the results of this research have been compared to dyssynchrony studies using echocardiography, but a further study with direct comparison would be necessary before clinical implementation. Nevertheless, it is becoming clear that dyssynchrony plays an important role in assessing cardiac function and will continue to play an increasing role in the constantly evolving field of cardiac imaging. Combining dyssynchrony with other novel approaches, such as contraction patterns, image texture and more advanced dyssynchrony measurements, with known clinical predictors, may potentially improve the results.

Bibliography

- [1] OpenStax College, "A labelled diagram of the anatomy of the heart",
https://commons.wikimedia.org/wiki/File:2008_Internal_Anatomy_of_the_HeartN.jpg,
<https://creativecommons.org/licenses/by/3.0/legalcode> 2008.
- [2] OpenStax College, "Conduction System of Heart",
https://commons.wikimedia.org/wiki/File:2018_Conduction_System_of_Heart.jpg,
<https://creativecommons.org/licenses/by/3.0/legalcode> 2018.
- [3] R. Abou, P. van der Bijl, J. J. Bax, and V. Delgado, "Global longitudinal strain: clinical use and prognostic implications in contemporary practice," *Heart*, vol. 106, no. 18, pp. 1438–1444, 2020.
- [4] British Heart Foundation, "Scotland factsheet,"
<https://www.bhf.org.uk/what-we-do/our-research/heart-statistics>, July 2021.
- [5] H. Dai, A. A. Much, E. Maor, E. Asher, A. Younis, Y. Xu, Y. Lu, X. Liu, J. Shu, and N. L. Bragazzi, "Global, regional, and national burden of ischaemic heart disease and its attributable risk factors, 1990–2017: results from the global burden of disease study 2017," *European Heart Journal-Quality of Care and Clinical Outcomes*, 2020.
- [6] M. W. Groch, E. G. DePuey, A. C. Belzberg, W. D. Erwin, M. Kamran, C. A. Barnett, R. C. Hendel, S. M. Spies, A. Ali, and R. C. Marshall, "Planar imaging versus gated blood-pool spect for the assessment of ventricular performance: a multicenter study," *Journal of Nuclear Medicine*, vol. 42, no. 12, pp. 1773–1779, 2001.
- [7] G. A. Wright, S. Thackray, S. Howey, and J. G. Cleland, "Left ventricular ejection fraction and volumes from gated blood-pool spect: comparison with planar gated blood-pool imaging and assessment of repeatability in patients with heart failure," *Journal of Nuclear Medicine*, vol. 44, no. 4, pp. 494–498, 2003.
- [8] M. S. J. Sutton, M. A. Pfeffer, L. Moye, T. Plappert, J. L. Rouleau, G. Lamas, J. Rouleau, J. O. Parker, M. O. Arnold, B. Sussex, *et al.*, "Cardiovascular death and left ventricular remodeling two years after myocardial infarction: baseline predictors and

- impact of long-term use of captopril: information from the survival and ventricular enlargement (SAVE) trial,” *Circulation*, vol. 96, no. 10, pp. 3294–3299, 1997.
- [9] M. M. McDermott, J. Feinglass, P. I. Lee, S. Mehta, B. Schmitt, F. Lefevre, and M. Gheorghiade, “Systolic function, readmission rates, and survival among consecutively hospitalized patients with congestive heart failure,” *American Heart Journal*, vol. 134, no. 4, pp. 728–736, 1997.
- [10] S. D. Solomon, N. Anavekar, H. Skali, J. J. McMurray, K. Swedberg, S. Yusuf, C. B. Granger, E. L. Michelson, D. Wang, S. Pocock, *et al.*, “Influence of ejection fraction on cardiovascular outcomes in a broad spectrum of heart failure patients,” *Circulation*, vol. 112, no. 24, pp. 3738–3744, 2005.
- [11] K. Jones and N. Goodfield, “Mechanical dyssynchrony and super-response to CRT,” *Journal of Nuclear Cardiology*, <https://doi.org/10.1007/s12350-020-02453-1>, 2021.
- [12] H. Bader, S. Garrigue, S. Lafitte, S. Reuter, P. Jais, M. Haïssaguerre, J. Bonnet, J. Clementy, and R. Roudaut, “Intra-left ventricular electromechanical asynchrony: a new independent predictor of severe cardiac events in heart failure patients,” *Journal of the American College of Cardiology*, vol. 43, no. 2, pp. 248–256, 2004.
- [13] M. Fudim, F. Dalgaard, M. Fathallah, A. E. Iskandrian, and S. Borges-Neto, “Mechanical dyssynchrony: How do we measure it, what it means, and what we can do about it,” *Journal of Nuclear Cardiology*, pp. 1–11, 2019.
- [14] J. Gorcsan III, P. Sogaard, J. J. Bax, J. P. Singh, W. T. Abraham, J. S. Borer, K. Dickstein, D. Gras, H. Krum, J. Brugada, *et al.*, “Association of persistent or worsened echocardiographic dyssynchrony with unfavourable clinical outcomes in heart failure patients with narrow QRS width: a subgroup analysis of the EchoCRT trial,” *European heart journal*, vol. 37, no. 1, pp. 49–59, 2016.
- [15] G. Cho, J. Song, W. Park, S. Han, S. Choi, Y. Doo, D. Oh, and Y. Lee, “Mechanical dyssynchrony assessed by tissue doppler imaging is a powerful predictor of mortality in congestive heart failure with normal QRS duration,” *Journal of the American College of Cardiology*, vol. 46, no. 12, pp. 2237–2243, 2005.
- [16] P. Ponikowski, A. A. Voors, S. D. Anker, H. Bueno, J. G. Cleland, A. J. Coats, V. Falk, J. R. González-Juanatey, V. Harjola, E. A. Jankowska, *et al.*, “2016 esc guidelines for the diagnosis and treatment of acute and chronic heart failure: The task force for the diagnosis and treatment of acute and chronic heart failure of the european society of cardiology (ESC) developed with the special contribution of the heart failure association (HFA) of the ESC,” *European Heart Journal*, vol. 37, no. 27, pp. 2129–2200, 2016.

- [17] C. Yu, H. Lin, Q. Zhang, and J. Sanderson, "High prevalence of left ventricular systolic and diastolic asynchrony in patients with congestive heart failure and normal QRS duration," *Heart*, vol. 89, no. 1, pp. 54–60, 2003.
- [18] E. S. Chung, A. R. Leon, L. Tavazzi, J. Sun, P. Nihoyannopoulos, J. Merlino, W. T. Abraham, S. Ghio, C. Leclercq, J. J. Bax, *et al.*, "Results of the predictors of response to crt (PROSPECT) trial," *Echocardiography*, vol. 2608, p. 2616, 2008.
- [19] N. M. Hawkins, M. C. Petrie, M. R. MacDonald, K. J. Hogg, and J. J. McMurray, "Selecting patients for cardiac resynchronization therapy: electrical or mechanical dyssynchrony?," *European Heart Journal*, vol. 27, no. 11, pp. 1270–1281, 2006.
- [20] I. Stankovic, C. Prinz, A. Ciarka, A. M. Daraban, M. Kotrc, M. Aarones, M. Szulik, S. Winter, A. Belmans, A. N. Neskovic, *et al.*, "Relationship of visually assessed apical rocking and septal flash to response and long-term survival following cardiac resynchronization therapy (PREDICT-CRT)," *European Heart Journal-Cardiovascular Imaging*, vol. 17, no. 3, pp. 262–269, 2016.
- [21] J. Gorcsan, C. P. Anderson, B. Tayal, M. Sugahara, J. Walmsley, R. C. Starling, and J. Lumens, "Systolic stretch characterizes the electromechanical substrate responsive to cardiac resynchronization therapy," *JACC: Cardiovascular Imaging*, vol. 12, no. 9, pp. 1741–1752, 2019.
- [22] J. M. Aalen, E. Donal, C. K. Larsen, J. Duchenne, M. Lederlin, M. Cvijic, A. Hubert, G. Voros, C. Leclercq, J. Bogaert, *et al.*, "Imaging predictors of response to cardiac resynchronization therapy: left ventricular work asymmetry by echocardiography and septal viability by cardiac magnetic resonance," *European Heart Journal*, vol. 41, no. 39, pp. 3813–3823, 2020.
- [23] P. Thavendiranathan, A. D. Grant, T. Negishi, J. C. Plana, Z. B. Popović, and T. H. Marwick, "Reproducibility of echocardiographic techniques for sequential assessment of left ventricular ejection fraction and volumes: application to patients undergoing cancer chemotherapy," *Journal of the American College of Cardiology*, vol. 61, no. 1, pp. 77–84, 2013.
- [24] K. Negishi, T. Negishi, J. Hare, B. Haluska, J. Plana, and T. Marwick, "Independent and incremental value of deformation indices for prediction of trastuzumab-induced cardiotoxicity," *Journal of the American Society of Echocardiography*, vol. 26 (5), pp. 493–498, 2013.
- [25] H. Sawaya, I. Sebag, J. Plana, J. Januzzi, B. Ky, V. Cohen, J. W. S. Gosavi, S. Carver, R. Martin, M. Picard, R. Gerszten, E. Halpern, I. Passeri, J. Kuter, and

- M. Scherrer-Crosbie, "Early detection and prediction of cardiotoxicity in chemotherapy-treated patients," *American Journal of Cardiology*, vol. 107, pp. 1375–1380, 2011.
- [26] E. A. Gripp, G. E. Oliveira, L. A. Feijó, M. I. Garcia, S. S. Xavier, and A. S. Sousa, "Global longitudinal strain accuracy for cardiotoxicity prediction in a cohort of breast cancer patients during anthracycline and/or trastuzumab treatment," *Arquivos Brasileiros de Cardiologia*, vol. 110(2), pp. 140–150, 2017.
- [27] H. Sawaya, I. Sebag, J. Plana, J. Januzzi, B. Ky, T. Tan, V. Cohen, J. Banchs, J. Carver, S. Wieggers, R. Martin, M. Picard, R. Gerszten, E. Halpern, J. Passeri, I. Kuter, and M. Scherrer-Crosbie, "Assessment of echocardiography and biomarkers for the extended prediction of cardiotoxicity in patients treated with anthracyclines, taxanes, and trastuzumab," *Circulation: Cardiovascular Imaging*, vol. 5, pp. 596–603, 2012.
- [28] M. T. Ali, E. Yucel, S. Bouras, L. Wang, H. W. Fei, E. F. Halpern, and M. Scherrer-Crosbie, "Myocardial strain is associated with adverse clinical cardiac events in patients treated with anthracyclines," *The American Society of Echocardiography*, vol. 29(6), pp. 522–527, 2016.
- [29] L. Jose, P. Lancellotti, D. MunEIJoz, V. Aboyans, R. Asteggiano, M. Galderisi, G. Habib, D. Lenihan, G. Lip, A. Lyon, T. Fernandez, D. Mohty, M. Piepoli, J. Tamargo, A. Torbicki, and T. Suter, "ESC position paper on cancer treatments and cardiovascular toxicity developed under the auspices of the esc committee for practice guidelines," *European Heart Journal*, vol. 37, pp. 2768–2801, 2016.
- [30] J. Chen, E. V. Garcia, R. D. Folks, C. D. Cooke, T. L. Faber, E. L. Tauxe, and A. E. Iskandrian, "Onset of left ventricular mechanical contraction as determined by phase analysis of ecg-gated myocardial perfusion spect imaging: development of a diagnostic tool for assessment of cardiac mechanical dyssynchrony," *Journal of nuclear cardiology*, vol. 12, no. 6, pp. 687–695, 2005.
- [31] K. Nakajima, N. Matsumoto, T. Kasai, S. Matsuo, K. Kiso, and K. Okuda, "Normal values and standardization of parameters in nuclear cardiology: Japanese society of nuclear medicine working group database," *Annals of Nuclear Medicine*, vol. 30, no. 3, pp. 188–199, 2016.
- [32] A. Peix, G. Karthikeyan, T. Massardo, M. Kalaivani, C. Patel, L. M. Pabon, A. Jiménez-Heffernan, E. Alexanderson, S. Butt, A. Kumar, *et al.*, "Value of intraventricular dyssynchrony assessment by gated-spect myocardial perfusion imaging in the management of heart failure patients undergoing cardiac resynchronization therapy (VISION-CRT)," *Journal of Nuclear Cardiology*, pp. 1–10, 2019.

- [33] A. Mukherjee, C. D. Patel, N. Naik, G. Sharma, and A. Roy, “Quantitative assessment of cardiac mechanical dyssynchrony and prediction of response to cardiac resynchronization therapy in patients with non-ischaemic dilated cardiomyopathy using equilibrium radionuclide angiography,” *Europace*, vol. 18, no. 6, pp. 851–857, 2016.
- [34] N. Badhwar, J. James, K. Hoffmayer, J. O’Connell, D. Green, T. De Marco, and E. Botvinick, “Utility of equilibrium radionuclide angiogram-derived measures of dyssynchrony to predict outcomes in heart failure patients undergoing cardiac resynchronization therapy,” *Journal of Nuclear Medicine*, vol. 57, pp. 1880–1886, 2016.
- [35] N. Kano, T. Okumura, S. Isobe, A. Sawamura, N. Watanabe, K. Fukaya, H. Mori, R. Morimoto, K. Kato, Y. K. Bando, *et al.*, “Left ventricular phase entropy: Novel prognostic predictor in patients with dilated cardiomyopathy and narrow QRS,” *Journal of Nuclear Cardiology*, vol. 25, no. 5, pp. 1677–1687, 2018.
- [36] J. Cullen, A. Saleem, R. Swindell, P. Burt, and C. Moore, “Measurement of cardiac synchrony using approximate entropy applied to nuclear medicine scans,” *Biomedical Signal Processing and Control*, vol. 5, pp. 32–36, 1 2010.
- [37] E. H. Botvinick, M. B. Fraiss, D. W. Shosa, M. A. O’Connell, J. A. Pacheco-Alvarez, M. Scheinman, R. S. Hattner, F. Morady, and D. B. Faulkner, “An accurate means of detecting and characterizing abnormal patterns of ventricular activation by phase image analysis,” *The American Journal of Cardiology*, vol. 50, pp. 289–298, 1982.
- [38] M. Fraiss, E. H. Botvinick, D. W. Shosa, W. J. O’Connell, M. M. Scheinman, R. S. Hattner, and F. Morady, “Phase image characterization of ventricular contraction in left and right bundle branch block,” *The American Journal of Cardiology*, vol. 50, pp. 95–105, 1982.
- [39] M. Fraiss, E. Botvinick, D. Shosa, W. O’Connell, J. P. Alvarez, M. Dae, R. Hattner, and D. Faulkner, “Phase image characterization of localized and generalized left ventricular contraction abnormalities,” *Journal of the American College of Cardiology*, vol. 4, no. 5, pp. 987–998, 1984.
- [40] L. Brateman, K. Buckley, S. G. Keim, T. J. Wargovich, and C. M. Williams, “Left ventricular regional wall motion assessment by radionuclide ventriculography: a comparison of cine display with fourier imaging,” *Journal of Nuclear Medicine: official publication, Society of Nuclear Medicine*, vol. 32, no. 5, pp. 777–782, 1991.
- [41] E. Vallejo, L. Jiménez, G. Rodríguez, F. Roffe, and D. Bialostozky, “Evaluation of ventricular synchrony with equilibrium radionuclide angiography: assessment of variability and accuracy,” *Archives of Medical Research*, vol. 41, no. 2, pp. 83–91, 2010.

- [42] H. Singh, A. Singhal, P. Sharma, C. D. Patel, S. Seth, and A. Malhotra, "Quantitative assessment of cardiac mechanical synchrony using equilibrium radionuclide angiography," *Journal of Nuclear Cardiology*, vol. 20, no. 3, pp. 415–425, 2013.
- [43] L. Fauchier, O. Marie, D. Casset-Senon, D. Babuty, P. Cosnay, and J. P. Fauchier, "Interventricular and intraventricular dyssynchrony in idiopathic dilated cardiomyopathy: a prognostic study with fourier phase analysis of radionuclide angioscintigraphy," *Journal of the American College of Cardiology*, vol. 40, no. 11, pp. 2022–2030, 2002.
- [44] W. F. Kerwin, E. H. Botvinick, J. W. O'Connell, S. H. Merrick, T. DeMarco, K. Chatterjee, K. Scheibly, and L. A. Saxon, "Ventricular contraction abnormalities in dilated cardiomyopathy: effect of biventricular pacing to correct interventricular dyssynchrony," *Journal of the American College of Cardiology*, vol. 35, no. 5, pp. 1221–1227, 2000.
- [45] J. W. O'Connell, C. Schreck, M. Moles, N. Badwar, T. DeMarco, J. Olgin, B. Lee, Z. Tseng, U. Kumar, and E. H. Botvinick, "A unique method by which to quantitate synchrony with equilibrium radionuclide angiography," *Journal of Nuclear Cardiology*, vol. 12, no. 4, pp. 441–450, 2005.
- [46] C. E. Shannon, "A mathematical theory of communication," *The Bell System Technical Journal*, vol. 27, pp. 379–423, 1948.
- [47] C. J. Johnson, J. D. Roberts, J. H. James, K. S. Hoffmayer, N. Badhwar, I. A. Ku, S. Zhao, D. M. Naeger, R. K. Rao, J. W. O'Connell, *et al.*, "Comparison of radionuclide angiographic synchrony analysis to echocardiography and magnetic resonance imaging for the diagnosis of arrhythmogenic right ventricular cardiomyopathy," *Heart Rhythm*, vol. 12, no. 6, pp. 1268–1275, 2015.
- [48] S. M. Pincus, I. M. Gladstone, and R. A. Ehrenkranz, "A regularity statistic for medical data analysis Steven M. Pincus, and Richard A. Ehrenkranz, MD," *Journal of Clinical Monitoring*, vol. 7, no. 4, pp. 335–345, 1991.
- [49] G. S. Dawes, M. Moulden, O. Sheil, and C. W. Redman, "Approximate entropy, a statistic of regularity, applied to fetal heart rate data before and during labor," *Obstetrics and Gynecology*, vol. 80, pp. 763–768, November 1992.
- [50] M. P. Tulppo, T. H. Makikallio, T. E. Takala, T. Seppanen, and H. V. Huikuri, "Quantitative beat-to-beat analysis of heart rate dynamics during exercise," *American Journal of Physiology-Heart and Circulatory Physiology*, vol. 271, no. 1, pp. H244–H252, 1996.

- [51] A. D. Georgoulis, C. Moraiti, S. Ristanis, and N. Stergiou, "A novel approach to measure variability in the anterior cruciate ligament deficient knee during walking: The use of the approximate entropy in orthopaedics," *Journal of Clinical Monitoring and Computing*, vol. 20, no. 1, pp. 11–18, 2006.
- [52] A. H. Khandoker, M. Palaniswami, and R. K. Begg, "A comparative study on approximate entropy measure and poincaré plot indexes of minimum foot clearance variability in the elderly during walking," *Journal of NeuroEngineering and Rehabilitation*, vol. 5, p. 4, 2008.
- [53] S. M. Pincus and E. K. Kalman, "Irregularity, volatility, risk, and financial market time series," *Proceedings of the National Academy of Sciences*, vol. 101(38), pp. 13709–13714, 2004.
- [54] S. M. Pincus and A. L. Goldberger, "Physiological time-series analysis: what does regularity quantify?," *The American Journal of Physiology*, vol. 266 (4), pp. 1643–1656, 1994.
- [55] R. A. McKinley, L. K. McIntire, R. Schmidt, D. W. Repperger, and J. A. Caldwell, "Evaluation of eye metrics as a detector of fatigue," *Human Factors*, vol. 53 (4), pp. 403–414, 2011.
- [56] K. Yun, "Decreased cortical complexity in methamphetamine abusers," *Psychiatry Research: Neuroimaging*, vol. 201(3), pp. 226–32, 2012.
- [57] J. M. Yentes, N. Hunt, K. K. Schmid, J. P. Kaipust, D. McGrath, and N. Stergiou, "The appropriate use of approximate entropy and sample entropy with short data sets," *Annals of Biomedical Engineering*, vol. 42, pp. 349–65, 2012.
- [58] A. Delgado-Bonal and A. Marshak, "Approximate entropy and sample entropy: A comprehensive tutorial," *Entropy*, vol. 21 6, p. 541, 2019.
- [59] J. S. Richman and J. R. Moorman, "Physiological time-series analysis using approximate entropy and sample entropy," *American Journal of Physiology-Heart and Circulatory Physiology*, vol. 278, no. 6, pp. H2039–H2049, 2000.
- [60] J. M. Yentes, W. Denton, J. McCamley, P. Raffalt, and K. K. Schmid, "Effect of parameter selection on entropy calculation for long walking trials," *Gait Posture*, vol. 60, pp. 128–134, 2018.
- [61] L. Montesinos, R. Castaldo, and L. Pecchia, "On the use of approximate entropy and sample entropy with centre of pressure time-series," *Journal of NeuroEngineering and Rehabilitation*, vol. 15, 2018.

- [62] R Core Team, *R: A Language and Environment for Statistical Computing*. R Foundation for Statistical Computing, Vienna, Austria, 2018.
- [63] H. Wickham, *ggplot2: Elegant Graphics for Data Analysis*. Springer-Verlag New York, 2016.
- [64] J. Cheng, *ggpval: Annotate Statistical Tests for 'ggplot2'*, 2019. R package version 0.2.3.
- [65] M. Kuhn, *caret: Classification and Regression Training*, 2020. R package version 6.0-86.
- [66] C. J, “Hotelling: Hotelling’s t^2 test and variants. R package version 1.0-5,” 2018.
- [67] H. Greenspan, B. Van Ginneken, and R. M. Summers, “Guest editorial deep learning in medical imaging: Overview and future promise of an exciting new technique,” *IEEE Transactions on Medical Imaging*, vol. 35, no. 5, pp. 1153–1159, 2016.
- [68] B. J. Erickson, P. Korfiatis, Z. Akkus, and T. L. Kline, “Machine learning for medical imaging,” *Radiographics*, vol. 37, no. 2, pp. 505–515, 2017.
- [69] K. Suzuki, “Overview of deep learning in medical imaging,” *Radiological Physics and Technology*, vol. 10, no. 3, pp. 257–273, 2017.
- [70] B. Sahiner, A. Pezeshk, L. M. Hadjiiski, X. Wang, K. Drukker, K. H. Cha, R. M. Summers, and M. L. Giger, “Deep learning in medical imaging and radiation therapy,” *Medical physics*, vol. 46, no. 1, pp. e1–e36, 2019.
- [71] R. P. Anderson, R. Jin, and G. L. Grunkemeier, “Understanding logistic regression analysis in clinical reports: an introduction,” *The Annals of Thoracic Surgery*, vol. 75, no. 3, pp. 753–757, 2003.
- [72] D. H. Alonso, M. N. Wernick, Y. Yang, G. Germano, D. S. Berman, and P. Slomka, “Prediction of cardiac death after adenosine myocardial perfusion SPECT based on machine learning,” *Journal of Nuclear Cardiology*, vol. 26, no. 5, pp. 1746–1754, 2019.
- [73] E. Carluccio, P. Biagioli, G. Alunni, A. Murrone, C. Zuchi, S. Coiro, C. Riccini, A. Mengoni, A. D’Antonio, and G. Ambrosio, “Prognostic value of right ventricular dysfunction in heart failure with reduced ejection fraction: superiority of longitudinal strain over tricuspid annular plane systolic excursion,” *Circulation: Cardiovascular Imaging*, vol. 11, no. 1, p. e006894, 2018.
- [74] E. C. Sammut, A. D. Villa, G. Di Giovine, L. Dancy, F. Bosio, T. Gibbs, S. Jeyabraba, S. Schwenke, S. E. Williams, M. Marber, *et al.*, “Prognostic value of quantitative stress

- perfusion cardiac magnetic resonance,” *JACC: Cardiovascular Imaging*, vol. 11, no. 5, pp. 686–694, 2018.
- [75] B. Whitcher, V. J. Schmid, and A. Thornton, “Working with the DICOM and NIfTI data standards in R,” *Journal of Statistical Software*, vol. 44, no. 6, pp. 1–28, 2011.
- [76] K. A. Jones, C. A. Paterson, D. J. Hamilton, A. D. Small, W. Martin, J. Robinson, and N. Goodfield, “Optimising approximate entropy for assessing cardiac dyssynchrony with radionuclide ventriculography,” *Biomedical Signal Processing and Control*, vol. 68, p. 102703, 2021.
- [77] S. M. Pincus, “Approximate entropy as a measure of system complexity,” *Mathematics*, vol. 88, pp. 2297–2301, 1991.
- [78] C. Marcassa, R. Campini, E. Verna, L. Ceriani, and P. Giannuzzi, “Assessment of cardiac asynchrony by radionuclide phase analysis: correlation with ventricular function in patients with narrow or prolonged QRS interval,” *European Journal of Heart Failure*, vol. 9, no. 5, pp. 484–490, 2007.
- [79] R. Wassenaar, D. O’Connor, B. Dij, R. Ruddy, and D. Birnie, “Optimisation and validation of radionuclide angiography phase analysis parameters for quantification of mechanical dyssynchrony,” *Journal of Nuclear Cardiology*, vol. 16, pp. 895–903, 2009.
- [80] S. Anwar, K. Negishi, A. Borowszki, P. Gladding, Z. B. Popović, F. Erenberg, and J. D. Thomas, “Comparison of two-dimensional strain analysis using vendor-independent and vendor-specific software in adult and pediatric patients,” *JRSM Cardiovascular Disease*, vol. 6, p. 2048004017712862, 2017.
- [81] K. A. Jones, A. D. Small, S. Ray, D. J. Hamilton, J. Robinson, N. E. R. Goodfield, and C. A. Paterson, “Radionuclide ventriculography phase analysis for risk stratification of patients undergoing cardiotoxic cancer therapy,” *Journal of Nuclear Cardiology*, <https://doi.org/10.1007/s12350-020-02277-z>, 2020.
- [82] M. Hooning, A. Botma, B. Aleman, M. Baaijens, H. Bartelink, J. G. M. Klijn, T. C, and V. L. F, “Long-term risk of cardiovascular disease in 10-year survivors of breast cancer,” *Journal of the National Cancer Institute*, vol. 99 (5), pp. 365–375, 2007.
- [83] J. Doyle, A. Neugut, J. Jacobson, V. Grann, and D. Hershman, “Chemotherapy and cardiotoxicity in older breast cancer patients: A population-based study,” *Journal of Clinical Oncology*, vol. 23 (34), pp. 8597–8605, 2005.
- [84] N. B. Boekel, J. N. Jacobse, M. Schaapveld, M. J. Hooning, J. A. Gietema, F. K. Duane, C. W. Taylor, S. C. Darby, M. Hauptmann, C. M. Seynaeve, M. H. A. Baaijens, G. S.

- Sonke, E. J. T. Rutgers, N. S. Russell, B. M. P. Aleman, and F. E. van Leeuwen, “cardiovascular disease incidence after internal mammary chain irradiation and anthracycline based chemotherapy for breast cancer,” *British Journal of Cancer*, vol. 119, pp. 408–418, 2018.
- [85] I. Perez, S. Alam, G. Hernandez, and R. Sancassani, “Cancer therapy-related cardiac dysfunction: An overview for the clinician,” *Clinical Medicine Insights: Cardiology*, vol. 13, pp. 1–11, 2019.
- [86] A. Seidman, C. Hudis, M. Pierri, S. Shak, V. Paton, M. Ashby, M. Murphy, S. Stewart, and D. Keefe, “Cardiac dysfunction in the trastuzumab clinical trials experience,” *Journal of Clinical Oncology*, vol. 20, pp. 1215–1221, 2002.
- [87] A. Mosterd and A. W. Hoes, “Clinical epidemiology of heart failure,” *Heart*, vol. 93, no. 9, pp. 1137–1146, 2007.
- [88] M. M. Redfield, S. J. Jacobsen, J. C. Burnett Jr, D. W. Mahoney, K. R. Bailey, and R. J. Rodeheffer, “Burden of systolic and diastolic ventricular dysfunction in the community: appreciating the scope of the heart failure epidemic,” *Jama*, vol. 289, no. 2, pp. 194–202, 2003.
- [89] G. S. Bleumink, A. M. Knetsch, M. C. Sturkenboom, S. M. Straus, A. Hofman, J. W. Deckers, J. C. Witteman, and B. H. C. Stricker, “Quantifying the heart failure epidemic: prevalence, incidence rate, lifetime risk and prognosis of heart failure: The rotterdam study,” *European Heart Journal*, vol. 25, no. 18, pp. 1614–1619, 2004.
- [90] F. Ceia, C. Fonseca, T. Mota, H. Morais, F. Matias, A. de Sousa, and A. G. Oliveira, “Prevalence of chronic heart failure in southwestern europe: the EPICA study,” *European journal of Heart Failure*, vol. 4, no. 4, pp. 531–539, 2002.
- [91] R. Levin, M. Dolgin, C. Fox, and R. Gorli, “The criteria committee of the new york heart association: Nomenclature and criteria for diagnosis of diseases of the heart and great vessels,” *LWW Handbooks*, pp. 140–150, 1994.
- [92] J. J. Bax, T. H. Marwick, S. G. Molhoek, G. B. Bleeker, L. Van Erven, E. Boersma, P. Steendijk, E. E. van der Wall, and M. J. Schalij, “Left ventricular dyssynchrony predicts benefit of cardiac resynchronization therapy in patients with end-stage heart failure before pacemaker implantation,” *The American Journal of Cardiology*, vol. 92, no. 10, pp. 1238–1240, 2003.
- [93] C. Yu, W. Fung, H. Lin, Q. Zhang, J. E. Sanderson, and C. Lau, “Predictors of left ventricular reverse remodeling after cardiac resynchronization therapy for heart failure

- secondary to idiopathic dilated or ischemic cardiomyopathy,” *The American Journal of Cardiology*, vol. 91, no. 6, pp. 684–688, 2003.
- [94] L. H. Opie and B. J. Gersh, *Drugs for the Heart*. London: Elsevier Saunders, 2005.
- [95] P. Lechat, M. Packer, S. Chalon, M. Cucherat, T. Arab, and J. Boissel, “Clinical effects of β -adrenergic blockade in chronic heart failure: a meta-analysis of double-blind, placebo-controlled, randomized trials,” *Circulation*, vol. 98, no. 12, pp. 1184–1191, 1998.
- [96] J. M. Brophy, L. Joseph, and J. L. Rouleau, “ β -blockers in congestive heart failure: a bayesian meta-analysis,” *Annals of internal medicine*, vol. 134, no. 7, pp. 550–560, 2001.
- [97] CIBIS Investigators and Committees, “A randomized trial of beta-blockade in heart failure the cardiac insufficiency bisoprolol study (CIBIS),” *Circulation*, vol. 90, pp. 1765–73, 1994.
- [98] Y. Takemoto, T. Hozumi, K. Sugioka, Y. Takagi, Y. Matsumura, M. Yoshiyama, T. P. Abraham, and J. Yoshikawa, “Beta-blocker therapy induces ventricular resynchronization in dilated cardiomyopathy with narrow QRS complex,” *Journal of the American College of Cardiology*, vol. 49, no. 7, pp. 778–783, 2007.
- [99] F. Monitillo, V. Di Terlizzi, M. I. Gioia, R. Barone, D. Grande, G. Parisi, N. D. Brunetti, and M. Iacoviello, “Right ventricular function in chronic heart failure: From the diagnosis to the therapeutic approach,” *Journal of cardiovascular development and disease*, vol. 7, no. 2, p. 12, 2020.
- [100] J. McGowan, W. Martin, M. Burgess, G. McCurrach, S. Ray, T. McDonagh, and J. Cleland, “Validation of an echocardiographic wall motion index in heart failure due to ischaemic heart disease,” *European journal of heart failure*, vol. 3, no. 6, pp. 731–737, 2001.
- [101] M. G. Kaya, B. Sarli, M. Akpek, E. G. Kaya, M. Yarlioglues, R. Topsakal, and Y.-Y. Lam, “Evaluation of beta-blockers on left ventricular dyssynchrony and reverse remodeling in idiopathic dilated cardiomyopathy: A randomized trial of carvedilol and metoprolol,” *Cardiology Journal*, vol. 21, no. 4, pp. 434–441, 2014.
- [102] W. Al-Jaroudi, F. Iqbal, J. Heo, and A. E. Iskandrian, “Relation between heart rate and left ventricular mechanical dyssynchrony in patients with end-stage renal disease,” *The American Journal of Cardiology*, vol. 107, no. 8, pp. 1235–1240, 2011.
- [103] A. J. Barron, R. Xavier, M. Al-Housni, E. Reyes, and R. Underwood, “Phase analysis, a novel SPECT technique for left ventricular dyssynchrony: Are degrees and milliseconds interchangeable?,” *Journal of Nuclear Cardiology*, vol. 27, no. 6, pp. 2273–2279, 2020.

- [104] S. Lafitte, P. Bordachar, M. Lafitte, S. Garrigue, S. Reuter, P. Reant, K. Serri, V. Lebouffos, M. Berrhouet, P. Jais, *et al.*, “Dynamic ventricular dyssynchrony: an exercise-echocardiography study,” *Journal of the American College of Cardiology*, vol. 47, no. 11, pp. 2253–2259, 2006.
- [105] C. Valzania, F. Gadler, M. J. Eriksson, A. Olsson, G. Boriani, and F. Braunschweig, “Electromechanical effects of cardiac resynchronization therapy during rest and stress in patients with heart failure,” *European Journal of Heart Failure*, vol. 9, no. 6-7, pp. 644–650, 2007.
- [106] S. Chattopadhyay, M. F. Alamgir, N. P. Nikitin, A. G. Fraser, A. L. Clark, and J. G. Cleland, “The effect of pharmacological stress on intraventricular dyssynchrony in left ventricular systolic dysfunction,” *European Journal of Heart Failure*, vol. 10, no. 4, pp. 412–420, 2008.
- [107] CIBIS-II Investigators, “The cardiac insufficiency bisoprolol study II (CIBIS-II): a randomised trial,” *The Lancet*, vol. 353, no. 9146, pp. 9–13, 1999.
- [108] T. H. LeJemtel, “Review of the cardiac insufficiency bisoprolol study II (CIBIS-II).,” *Current Cardiology Reports*, vol. 1, no. 1, pp. 29–30, 1999.
- [109] I. V. Askari and O. A. Osipova, “Influence of beta-blockers on mechanical dyssynchrony and cardiac remodeling in patients with ischemic chronic heart failure in the setting of revascularization,” *Research Results in Pharmacology*, vol. 5, no. 1, pp. 1–13, 2019.
- [110] E. Tatli, T. Kurum, M. Aktoz, and M. Buyuklu, “Effects of carvedilol on right ventricular ejection fraction and cytokines levels in patients with systolic heart failure,” *International Journal of Cardiology*, vol. 125, no. 2, pp. 273–276, 2008.
- [111] A. Giardini, L. Lovato, A. Donti, R. Formigari, G. Gargiulo, F. M. Picchio, and R. Fattori, “A pilot study on the effects of carvedilol on right ventricular remodelling and exercise tolerance in patients with systemic right ventricle,” *International Journal of Cardiology*, vol. 114, no. 2, pp. 241–246, 2007.
- [112] W. Ouwerkerk, A. A. Voors, and A. H. Zwinderman, “Factors influencing the predictive power of models for predicting mortality and/or heart failure hospitalization in patients with heart failure,” *JACC: Heart Failure*, vol. 2, no. 5, pp. 429–436, 2014.
- [113] K. Rahimi, D. Bennett, N. Conrad, T. M. Williams, J. Basu, J. Dwight, M. Woodward, A. Patel, J. McMurray, and S. MacMahon, “Risk prediction in patients with heart failure: a systematic review and analysis,” *JACC: Heart Failure*, vol. 2, no. 5, pp. 440–446, 2014.